1977

Thermal response of a composite bridge structure

David John Wisch

Department:

THERMAL RESPONSE OF A COMPOSITE BRIDGE STRUCTURE

BY

DAVID JOHN WISCH, 1953-

A THESIS

Presented to the Faculty of the Graduate School of the

UNIVERSITY OF MISSOURI-ROLLA

In Partial Fulfillment of the Requirements for the Degree

MASTER OF SCIENCE IN CIVIL ENGINEERING

1977

Approved by

J. W. Emsoner (Advisor) W. A. Andrews

M. G. Lay

ABSTRACT

This experimental investigation was conducted as an intermediate study to verify and substantiate a prior theoretical study for possible utilization toward development of rational bridge design criteria. The objectives of the study were to construct and instrument a 15 ft - 15 ft (4.6 m - 4.6 m) two-span, composite design, laboratory structure, to subject the structure to thermal loading, and to correlate the experimental temperature distributions, strain distributions, and deflections with those obtained from the theoretical study. Infrared heat lamps were used to obtain steady-state thermal loading.

Three theoretical cases were considered for strain calculations: a) both the slab and the beam in plane stress, b) the slab in plane strain and the beam in plane stress, and c) the slab in some state between plane stress and plane strain (partially restrained) and the beam in plane stress. The experimental and theoretical temperature distributions, strains, and deflections were in reasonable agreement.

It was concluded that the theoretical procedure provides a rational method for predicting the thermal behavior of composite-girder bridge structures and can be applied with reasonable confidence when used with realistic temperature profiles, material properties, and substructure stiffness characteristics.

ACKNOWLEDGEMENTS

The author wishes to thank Dr. Jack H. Emanuel for his advice and patient editing of this manuscript. Thanks are also due to Drs. W. A. Andrews and M. G. Parry for serving on the graduate committee.

Special notes of gratitude are due to Dr. J. Leroy Hulsey without whose help and encouragement this study could never have materialized and to Mr. Ken Haas for his many hours of work and the design and fabriaction of data recording equipment.

Among the many other people who helped and appreciation goes include DeLong's Inc. for suggestions and steel fabrication, fellow graduate students for aid in construction and valuable friendship, Mrs. Margot Lewis for her patient typing of the drafts and the final copy of this manuscript, and the author's parents for their continual support and encouragement.

Support for this investigation was provided by the Missouri Highway Cooperative Research Program.

TABLE OF CONTENTS

LIST OF ILLUSTRATIONS

Page

LIST OF TABLES

NOTATION[a]

A_b, A_f, A_s, A_{sL} = cross-sectional area of beam, top flange, slab, and slab section between flanges, respectively;

A_c = composite cross-sectional area of each element;

$\tilde{A}$, $\tilde{\tilde{A}}$ = elements of A matrix;

b_{ef} = effective width of slab;

b_f = width of top flange of beam;

c = half of depth of slab (always positive);

c_b, c_f, c_t = centroidal distances;

e = element;

E_b, E_f, E_s = modulus of elasticity of beam, top flange, and slab, respectively;

E_m = modulus of elasticity of the appropriate material;

F'_1, F'_2 = element interface forces, shear, and moment, respectively, for plane strain;

F_1,...F_8 = element interface forces for compatibility;

F_o = fixed end forces;

g = beam spacing;

g_s = slab width between beam flanges;

h_c = convection heat transfer coefficient;

I_b, I_f, I_s, I_{sL} = moment of inertia of separated element components;

I_c = composite moment of inertia of each element;

I_n = total value of radiation incident on bridge deck;

---

[a]Symbols such as ε and σ, which are common except for coordinate designation, have been listed for the x or longitudinal axis only.

k_i, k_x, k_y = anisotropic thermal conductivities;

ℓ = element length;

ℓ_x, ℓ_y = direction cosines of the outward normal of the deck;

M'_{tb}, M'_{tf}, M'_{ts}, M'_{tsL} = moment superimposed upon restrained separated element components to achieve free movement and to satisfy equilibrium;

n = modular ratio = E_b/E_s;

P = thrust of element e;

P'_{tb}, P'_{tf}, P'_{ts}, P'_{tsL} = force superimposed upon restrained separated element components to achieve free movement and to satisfy equilibrium;

q_{as} = heat flux resulting from long wave radiation;

q_c = heat flux resulting from convection;

q_r = heat flux resulting from long wave radiation from a structure;

q_s = heat flux resulting from solar radiation;

T = change in temperature;

t = temperature at any point;

$T(y)$ = change in temperature as a function of vertical distance;

T_a, T_c, T_∞ = ambient air temperature around bridge, F, C, K, respectively;

$T_b(y)$, $T_f(y)$, $T_s(y)$, $T_{sL}(y)$ = change in temperature in element components as a function of vertical distance;

T_α = temperature at any point of deck, k;

v = air velocity;

w = width of separated element component;

$w(y)$ = width of beam as a function of y;

y = distance in vertical direction (+ down);

y_b, y_f, y_s, y_{sL} = distance measured from centroidal axis of element component (+ down);

α = coefficient of thermal expansion;

α_b, α_f, α_s = coefficient of thermal expansion of beam and slab, respectively;

α_r = radiation absorbtivity factor;

β, β_f, β_y, $\bar{\beta}$, $\tilde{\beta}$ = elements of A matrix;

ε_{as} = atmospheric emittance;

ε_b, ε_o, ε_t, ε_x = unit strain;

ε_r = radiation emissivity coefficient;

$^c\varepsilon_{xs}$ = beam and slab compatibility strains, respectively, in the longitudinal direction;

ε'_{xb}, ε'_{xs} = longitudinal unit strain in restrained beam and slab, respectively;

$\overset{*}{\varepsilon}'_{xb}$, $\overset{*}{\varepsilon}'_{xf}$, $\overset{*}{\varepsilon}'_{xs}$, $\overset{*}{\varepsilon}'_{xsL}$ = unit strain in longitudinally restrained element components;

ε''_{xs} = longitudinal unit strain in beam and slab, respectively, resulting from interface loading;

θ = curvature;

θ_b, θ_s = beam and slab curvature, respectively;

λ, λ_f, $\bar{\lambda}$, $\tilde{\lambda}$ = elements of A matrix;

μ, μ_f, μ_s = Poisson's ratio;

ξ, ξ_b, ξ_o, ξ_t = x, y, or z distance;

ρ = radius of curvature;

ρ_b, ρ_s = radius of curvature of the beam and slab, respectively;

ρ_{IF} = radius of curvature at the slab and beam interface;

σ_{sb} = Stephan-Boltzman constant,

σ_x, σ_{xb}, σ_{xf}, σ_{xs}, σ_{xsL} = unit thermal stress;

$^{c}\sigma_{xb}$, $^{c}\sigma_{xs}$ = element component compatibility beam and slab stress, respectively;

σ'_{xb}, σ'_{xf}, σ'_{xs}, σ'_{xsL} = unit thermal stress in longitudinally unrestrained separated element components;

σ'_{xb_M}, σ'_{xs_M} = longitudinal unit stress induced by M'_{tb}, and M'_{ts}, respectively;

σ'_{xb_p}, σ'_{xs_p} = longitudinal unit stress induced by P'_{tb}, and P'_{ts}, respectively;

σ''_{xb}, σ''_{xf}, σ''_{xs} = longitudinal unit stress resulting from interface compatibility forces;

$\overset{*}{\sigma}'_{xb}$, $\overset{*}{\sigma}'_{xf}$, $\overset{*}{\sigma}'_{xs}$, $\overset{*}{\sigma}'_{xsL}$ = longitudinal unit stress in restrained separated element components;

τ = unit horizontal shear stress; and

ψ, ψ_f, ψ_s, $\bar{\psi}$, $\tilde{\psi}$, $\tilde{\bar{\psi}}$ = elements of A matrix.

I. INTRODUCTION

The primary cause of movement after the subsidence of initial shrinkage and creep deformations in a composite design bridge is temperature change. This temperature change induces thermal stresses unless the structure is homogeneous, free of restraints, and of constant temperature. Composite design structures do not fit this stress free category, because dissimilar materials are present and some type of restraint is normally applied at the supports of the deck. In normal design practice an attempt is made to provide for thermal movement by using expansion devices ranging from simple plates or pads to elaborate roller and rocker bearings.

In an effort to hold down the rapidly increasing maintenance costs of expansion devices and to develop more efficient designs through a better understanding of structural behavior, the thermal response of bridges has been the subject of much interest in the past few years[5, 6, 17, 19, 22, 24, 26, 33, 39, 40]. Some investigators have reported that thermally induced stresses in a composite design structure can reach 30 to 40 percent of the design strength of the component materials[6, 17, 22]. The major portion of these stresses is caused by the difference in the coefficients of thermal expansion of the concrete and the steel and the types and magnitude of restraints imposed on the deforming structure.

Thermally related problems have been the subject of rather extensive studies in Australia, Europe, and Canada; however, these studies have been concerned with concrete box-girder structures rather than with concrete-steel bridges of composite design. The heat

transfer analysis involved in the two types of construction differs very little, but the determination of strains and stresses is another matter. A one material structure has deformations and stresses resulting from thermal gradients that are nonlinear and from restraints acting on the abutments. On the other hand, construction using two dissimilar materials introduces another cause of stress that requires a complex solution, that being the interaction of the two materials against each other when temperatures change in any fashion, linear or nonlinear. This action is caused by the differing coefficients of thermal expansion and results when the materials are rigidly connected and forced to act as a single unit as is the case in a composite design.

Many studies have been undertaken to determine the coefficient of thermal expansion for concrete[4, 8, 9, 11, 12, 14, 18, 26, 29, 30, 34]. The results of these studies have then been applied with either assumed or theoretical temperature profiles to simple span structures in order to determine the magnitude of stresses involved.

Few bridges today are single span, and little work has been directed toward the indeterminate structures coupled with dissimilar materials. Previous studies[15, 16] have shown that the supporting and expansion devices commonly designed to eliminate the restraints of supports very often do not function properly. Thus, a popular design in recent years eliminates expansion devices by connecting the superstructure to a flexible substructure with either a pinned or integral (rigid) connection at the abutments. This procedure forces the superstructure and substructure to move as a single unit and somewhat restrains the superstructure's movement. Approach slabs leading to the abutments can cause a very large external force to be applied to the

bridge structure when both the slab and structure expand as a result of increasing temperatures.

A recently completed rigorous study at the University of Missouri-Rolla by Emanuel and Hulsey[17] and Hulsey[22] attacked thermally induced stresses from a theoretical standpoint. Acceptance of the theoretical results and their utilization toward rational design criteria is subject to substantiation by experimental results obtained from model and prototype structures. However, experimental results for correlation of the theoretical procedures have not been previously available.

The objectives of the study reported upon here were to construct and instrument a small, composite design, laboratory structure in the Structural Laboratory of the Engineering Research Laboratory at the University of Missouri-Rolla, to subject the structure to thermal loading, and to correlate the experimental results with calculated values obtained from the theoretical study[17, 22]. In addition, the heat transfer phenomenon was investigated, and the experimental results were correlated with values obtained from a theoretical numerical approach[22, 23]. Steady-state thermal loading was used, because it more accurately predicts field structure response. Recording units capable of recording the amount of data required within very small time increments were not economically feasible.

II. LABORATORY TEST STRUCTURE

The primary objective of the investigation was to correlate observed experimental values with calculated values obtained by utilizing theoretical procedures developed in previous studies by Emanuel et al.[16], Emanuel and Hulsey[17], and Hulsey[22]. The test structure utilized was a (15 ft - 15 ft) [4.6 m - 4.6 m] continuous composite design with a curved steel plate and pintle bearing at the center pier and integral abutments. An adequate rather than a true model was designed and subsequently constructed in the structural laboratory of the Engineering Research Laboratory, University of Missouri-Rolla.

A. SUBSTRUCTURE

1. Abutments. Integral stub abutments with flexible piling were modeled by the test structure. Modeling considerations included a desire for a constant soil modulus, noninterference of the container on the soil medium and pile interaction, and a reasonable piling-superstructure stiffness ratio.

The major soil modulus parameters in the test structure included the moisture content of the soil and the ability of the soil to retain a constant modulus under repeated loading and changes in atmospheric moisture content. Hence, sand was chosen rather than clay or silt, because the modulus of a granular soil is easier to control. A very dense, uniformly placed medium was also needed to prevent areas of local stress concentration. If the sand had been placed moist, it would have taken months for it to reduce to a dry condition at the lower levels of the abutments. This would have constantly changed the

modulus values and also would have tended to cement the sand grains together because of the presence of a small amount of clay particles. Subsequent crumbling under pile movement would have produced a non-uniform densification. Therefore, all the sand was dried before it was placed. The sand used for initial placement was heated and dried in an asphalt pugmill, and the small amount needed for final topping was dried with forced air in thin layers. These two methods reduced the moisture content to less than 2 percent. This percentage was low enough to insure no change in induced differential moisture at any level of the abutment.

Problems usually associated with densification were avoided by using the "rain" method of sand placement. Used first by Vesic[35] and recently by Hillhouse[20], the method provides a relatively high density which is very uniform across an area and through the depth of placement. In this method, a sand filled barrel is raised to a given height above the area to be filled, a trap door is released and the sand falls through a matrix of small holes in the bottom of the barrel. In essence, it "rains" sand. An average density of 104.5 pcf (16.4 kN/m^3) was attained.

To obtain good interaction between the piling and the sand, and to avoid stress concentrations on the piling due to the surrounding medium, a sand was sought with a small particle size and a uniform grain size. Masonry sand from the Meramac River fitted the criteria and was economically feasible. As can be seen from the grain-size distribution in Fig. 1, this sand is relatively uniform with very little minus 200 material, consequently the possibility of moisture gain through capillary action from the atmosphere could be neglected.

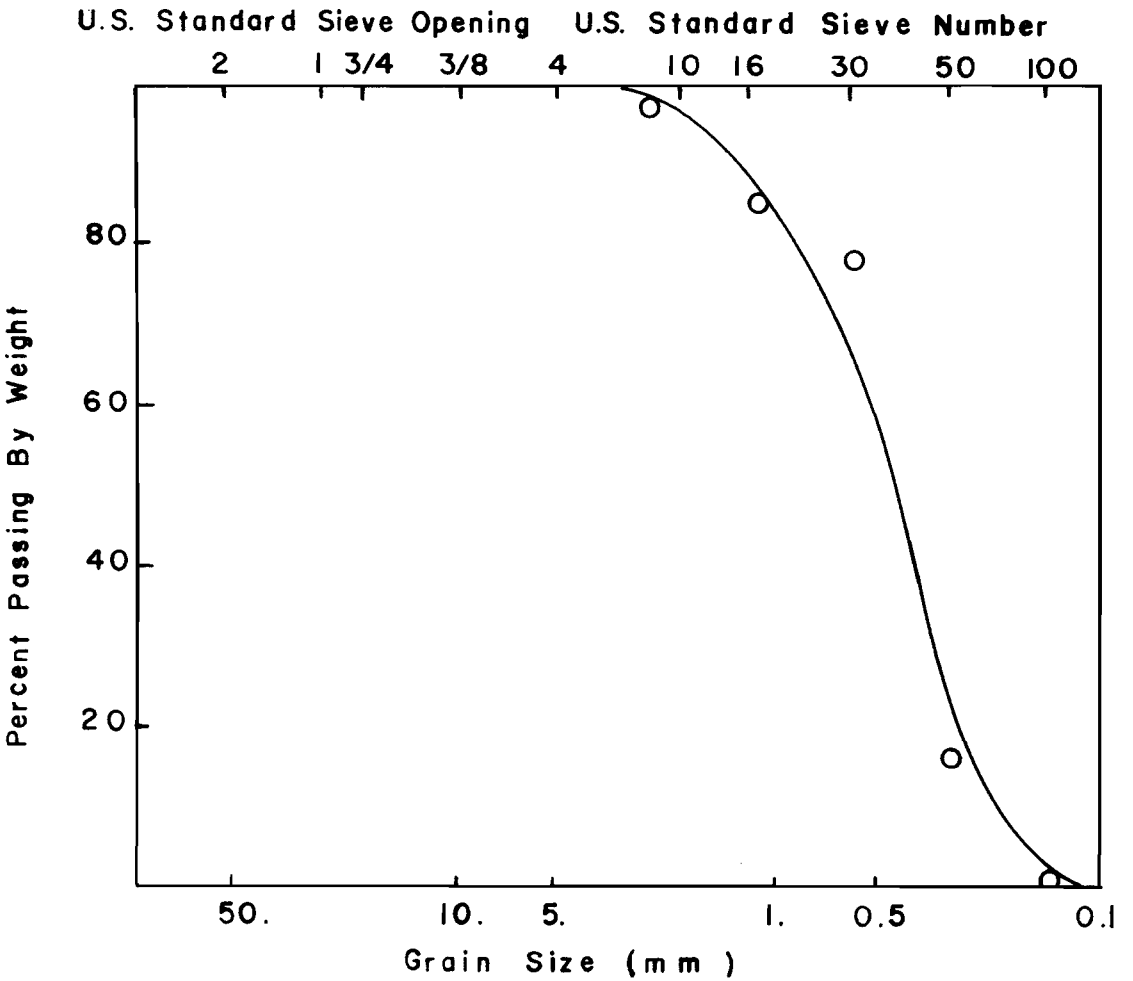

Fig. 1. Grain-Size Distribution of Abutment Sand

The ratios of distances from piling to container that were suggested by Davisson and Salley[13] in their discussion of model pile tests were used in the design of the sand boxes. These ratios were used to calculate minimum dimensions, and the adjusted final dimensions were: transverse to stringers, 7 ft (2.1 m); longitudinal (width/height = 0.4 to 0.5), 3 ft (0.9 m); and depth, 6 ft (1.8 m).

A computer program for analysis of beams on elastic foundations was used to model potential pile sizes. A soil pressure of 110 psf (5269 N/m^2) giving a triangular pressure distribution along the depth of the pile was input as a series of discrete elastic springs at small intervals. Numerous lengths and sizes of pipe and bar shapes were reviewed, and their resulting deflection patterns produced by a unit lateral load applied to the top of the pile were compared to classic pile deformation plots. A 72-in. (183-cm) long steel bar with a 5 x 1/2-in. (127 x 13-mm) cross section matched the classic curves quite well. Three piles, one under each stringer, were used at each abutment. For ease in placement, bearing attachment, and uniformity of rotations and displacements, a 6 x 1/2-in. (152 x 13-mm) plate pile cap was welded to the tops of the three piles. Before emplacing the sand, the piling assemblies were hung in the sand boxes so that the pile bottoms were 6 in. (15 cm) above floors of the boxes. The rain procedure previously described was then used to emplace the sand. No measureable deflection occurred when the pile bracing supports were removed.

2. Center Pier. Three 2-in. (5-cm) diameter by 76-1/2-in. (194-cm) long standard pipe sections spaced 20-in. (51-cm) on center and welded to a 12 x 1/2-in. (305 x 13-mm) base plate were used for the

center pier. A 6 x 1/2-in. (152 x 13-mm) plate was used as a pier cap for possible future placement of different types of support bearings. The pier assemblage is shown in Fig. 2.

The pier simulates a cantilever beam. Six 3-in. (7.6-cm) diameter holes were cored 4 in. (10 cm) into the existing floor. A hydrostone mixture was used to grout 3/4-in. (19-mm) diameter by 5-in. (127-mm) long anchor bolts into these holes. Later, the pier assemblage was bedded in hydrostone, the anchor bolts tightened, and the hydrostone allowed to expand between the floor and base plate to form a rigid connection.

The selection of the cantilever simulation for the pier agrees with the fact that in the field most piers have a relative point of fixity and the portion above this point acts as a cantilever. The selection also provided an easy reference for the determination of nonsymmetrical expansion of the spans and any force induced in the pier by such movement.

3. Bearings. An integral connection at the abutment was achieved by welding a stringer plate to the bottom flange of the stringer and bolting the plate to the abutment cap plate as shown in Fig. 3. The connection transferred rotation and moment from the stringer to the abutment piling.

The bearing at the pier simulates a type C bearing of the Missouri State Highway Department Standard Details. The fixed curved steel rocker plates, consisting of 6 x 1-1/2 x 6-in. (152 x 38 x 152-mm) plates machined to a 6-in. (152-mm) radius, were bolted to connection plates welded to the stringer flange and rested on 6 x 1/2 x 9-in. (152 x 13 x 229-mm) bearing plates having a machined top surface. Two

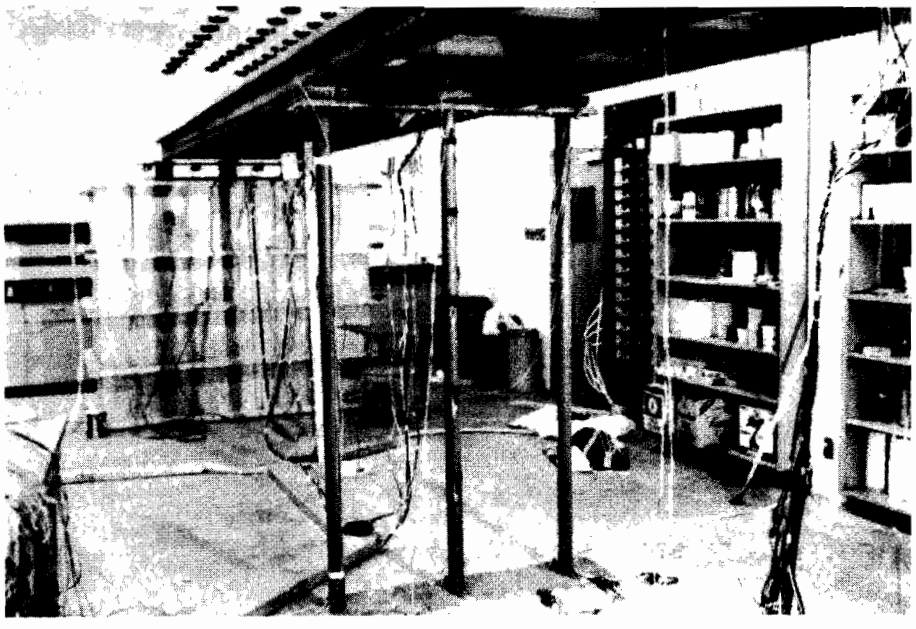

Fig. 2. Pier Assemblage

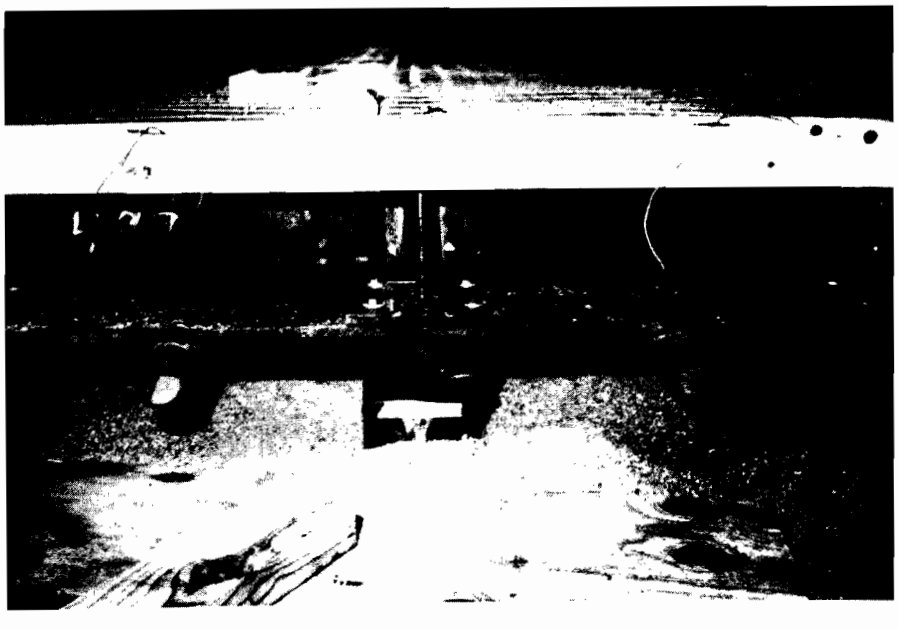

Fig. 3. Stringer Piling Connection

3/8-in. (10-mm) diameter chamfered pintles that protruded 7/8-in. (22-mm) above the bearing plate were used to prevent lateral displacement. Provision for rotation was provided by tapered holes in the curved steel rocker plates. The bearing details are shown in Figs. 4 and 5.

B. SUPERSTRUCTURE

1. Stringers. The stringer design loading consisted of the dead weight of the beam and slab, and assumed live load of 30 psf (1437 N/m^2), and an impact factor of 1.3 as calculated from the AASHTO specifications. The calculated stresses were multiplied by an amplification factor of 1.3 and checked against the maximum AASHTO allowable stresses for composite design. In accordance with reported theoretical values[6, 17, 22], the 1.3 amplification factor provided for a 30 percent increase caused by thermal stresses. Limited laboratory space restricted the total superstructure length to 30 ft (9 m).

Stress distributions for various sections and span lengths were reviewed and the M6 x 4.4 (15 cm x 64 N/m) section spaced 20 in. (51 cm) on center was selected. Only wide-flange shapes were considered, and fabrication and construction difficulties excluded cold-formed sections. The section was adequate for placement of the concrete deck without shoring. Because a lighter rolled section was not available, the M6 x 4.4 (15 cm x 64 N/m) section was also used for the outside stringers.

Four-inch (10-cm) channels were desired for lateral bracing and the C4 x 5.4 (10 cm x 79 N/m) section was selected for this purpose. Bearing connection plates, 6 x 1/2 x 6-in. (152 x 13 x 152-mm) with slotted holes were welded to the bottom flange of the stringers at the pier and at the abutments.

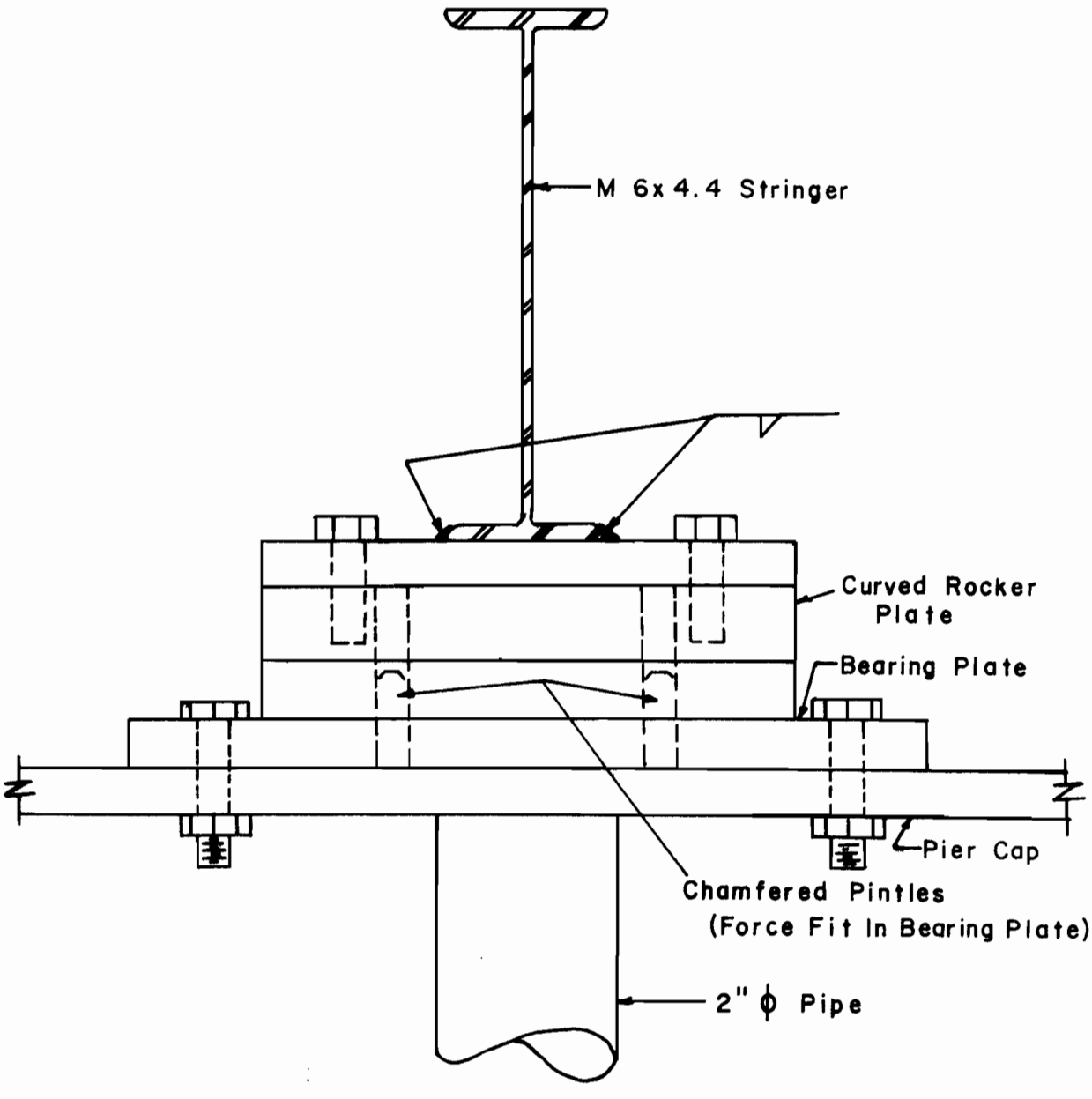

Fig. 4. Pier Bearing and Cross Section of Stringer

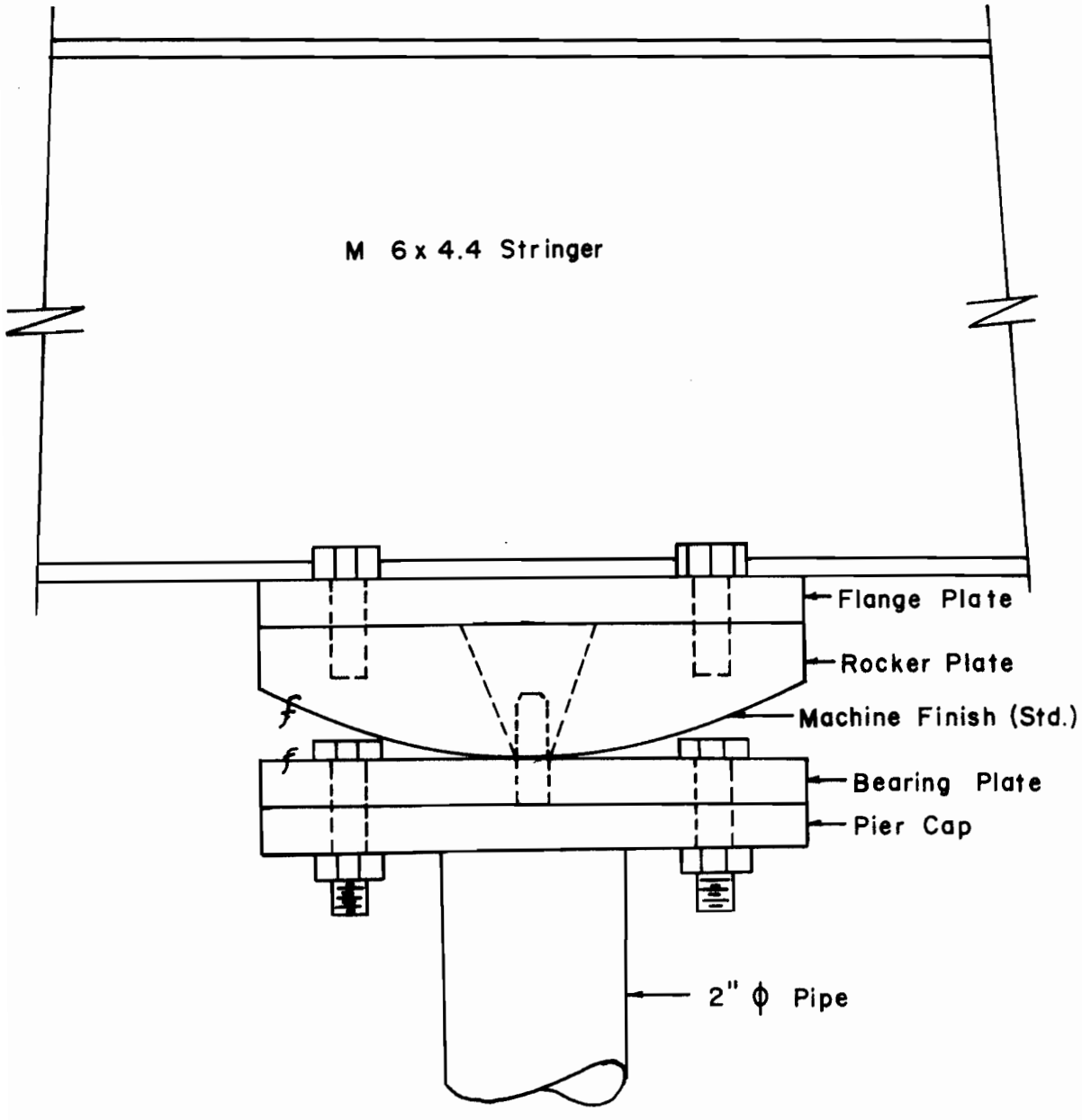

Fig. 5. Pier Bearing -- Side View

After consultation with the steel fabricator, 3/8-in. (10-mm) diameter by 7/8-in. (22-mm) stud shear connectors were selected. Larger diameters were not used because there was a possibility the stringer would warp from the heat during welding of the connectors to the stringer flange. A constant 4-in. (10-cm) spacing met the requirements of the stud design criteria and also simplified fabrication. In accordance with standard AASHTO procedures, shear connectors were not placed in high (negative moment) tensile zones, i.e., over the bearing at the pier. The steel layout is shown in Fig. 6.

2. Slab Design. Preliminary design calculations limited the slab depth to 1-1/2 in. (38-mm) to prevent the slab from becoming too stiff in relation to the stringers. As previously noted, loading consisted of dead load, a live load of 30 psf (1437 N/m^2) and an impact factor of 1.3. Slab design was based on one-way action with a span length of 20 in. (51 cm), which was the center to center spacing of the stringers. The overall width of the slab was 45. in. (114 cm). After calculating the required tension and shrinkage steel areas, a 16 gage 2-5/8-in. (68-mm) longitudinal (30-ft [9-m] stringer direction) by 2-in (51-mm) transverse galvanized welded wire mesh was selected, because it made it relatively easy to place the two layers of steel in the slab, and it provided steel in both the longitudinal and transverse directions. The top layer of mesh was positioned 1/4 in. (6 mm) from the top of the finished slab, and the lower layer was set 1-1/4 in. (32 mm) from the top of the slab. The lower mesh layer was supported by 1/4-in. (6-mm) square glass plates placed between it and the forms. The top mesh was supported by 16 gage bracket-shaped ([) wire chairs which rested on the forms.

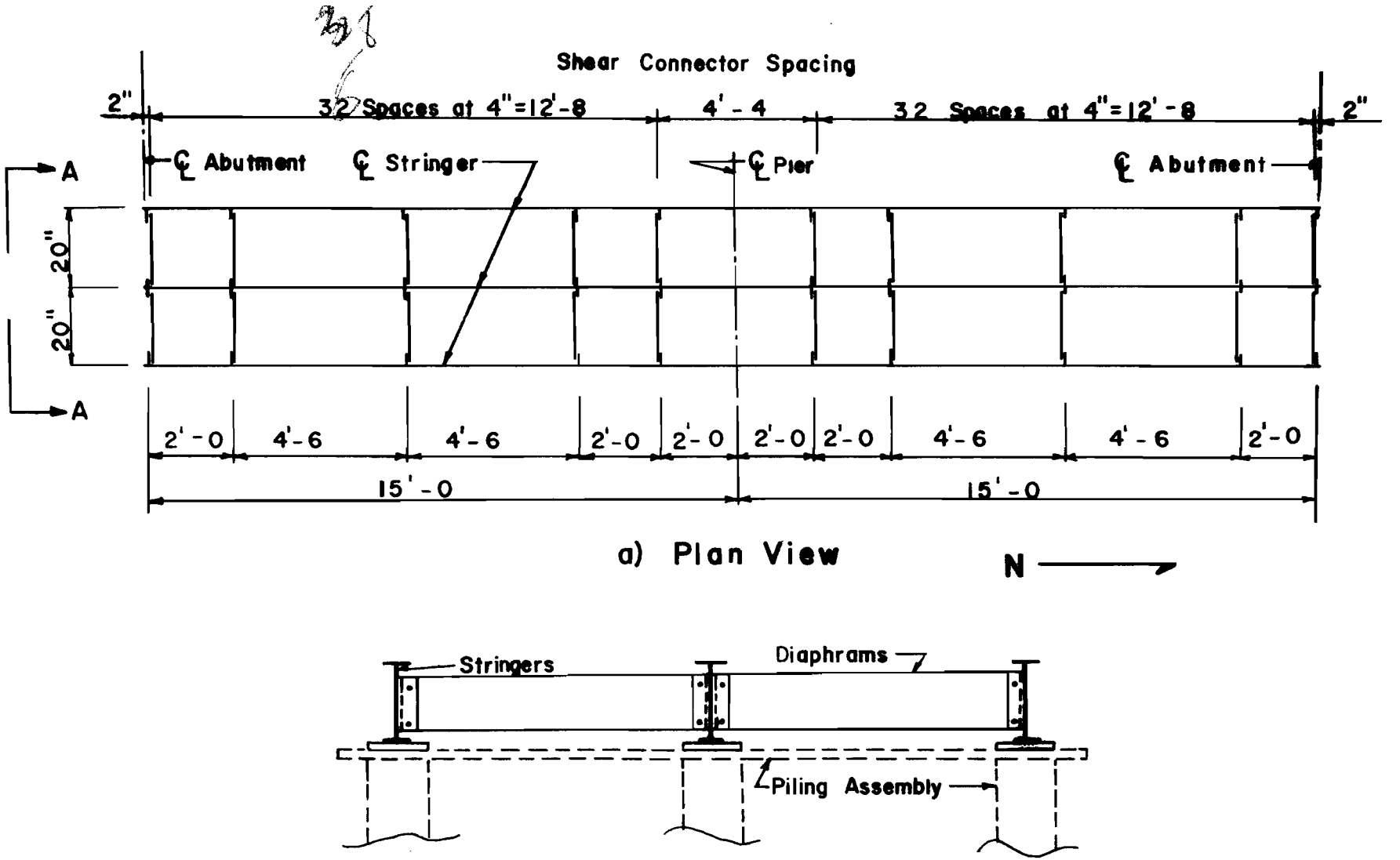

a) Plan View

b) Section A-A

Fig. 6. Steel Layout

3. Concrete Mix. The number and variety of constraints necessitated a special mix design for the slab. These constraints included a slab thickness of 1-1/2 in. (38 mm), placement of steel near the top and the bottom of the slab, a 28-day compressive strength of approximately 4000 psi (27,600 kN/m^2), an air content of 5-1/2 $\pm$ 1-1/2 percent (in accordance with the MSHD-1973 specification), a maximum limestone aggregate size of 3/8 in. (10 mm), uniformity after placement, and proper workability and finishing qualities. The mix design was selected on the basis of laboratory trial batches. Trial batches were mixed with different parameters of cement content, w/c ratio, and aggregate size and proportions. The slump, workability, and seven-day strength, which is about two-thirds of the 28-day strength, were observed for each batch. The final mix design was then based on a trial mix that met all constraints.

Crushed limestone with a maximum particle size of 3/8 in. (10 mm) was selected as the coarse aggregate. Limestone was selected because it is the coarse aggregate most commonly used in Missouri, and thus the thermal properties of the test mix would approximate a typical prototype mix. The fine aggregate as indicated previously came from the Meramac River and is a masonry blend sand. The sieve analysis for the coarse and fine aggregates is shown in Fig. 7.

Because a portion of the crushed limestone passed the No. 4 sieve thereby being considered as fine aggregate, a blend of aggregates was sought that would fit ASTM Standard C 33-74a recommended for concrete aggregates. A mixture of equal weights (0.98:1.00 rodded volume ratios) of stone and sand most closely met the standard. The mixed fine aggregate particle-size distribution and the ASTM recommended limits

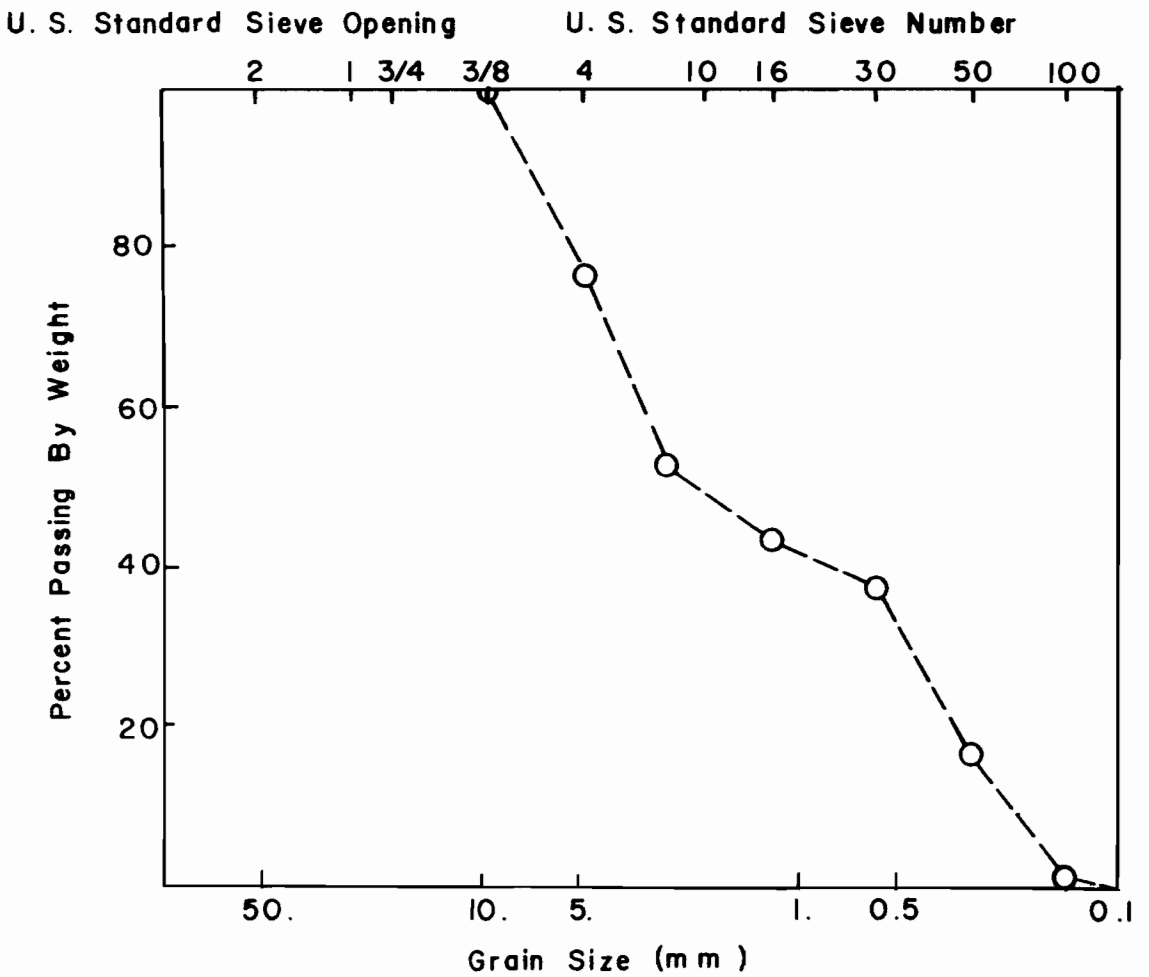

Fig. 7. Grain-Size Distribution of Concrete Aggregate

are shown in Fig. 8. Of the mixture, the 23 percent that was retained by the No. 4 sieve became coarse aggregate. Thirty-six percent of the fine aggregate was crushed limestone, and the remaining 64 percent consisted of river sand.

The final mix selected for the deck consisted of:

20.6 lb (91.7 N)	water
34.6 lb (154 N)	cement
68.0 lb (303 N)	sand (dry)
68.0 lb (303 N)	crushed limestone (dry)
4 cc	air entraining agent

These quantities yielded 1.4 cu ft (0.04 m^3) and were mixed in a 2 cu ft (0.06 m^3) capacity rotary type mixer. The cement was Red Ring brand and the air entraining agent was Darex. The air content, tested with a pressure indicator (bowl type), was 6.3 percent, and the 28-day strength averaged 4400 psi (30,360 N/m^2) for the cylinders tested. Placing of the slab began at the north end and was continuous towards the south. Sixteen batches were required and test cylinders were cast from every other batch. To aid in placement, the forms were vibrated with hand held rubber mallets.

After its surface had been hand finished, the deck was covered with wet blankets. These blankets were moistened daily for eight days. Both the blankets and the forms were removed on the ninth day following placement.

4. Formwork. Slab forms between stringers consisted of 1/2-in. (13-mm) plywood cut to provide for fast erection and easy removal when used with 2 x 4-in. (51 x 102-mm) wood spacers placed between stringer flanges as shown in Fig. 9. The edges were formed with 1 x 3-in.

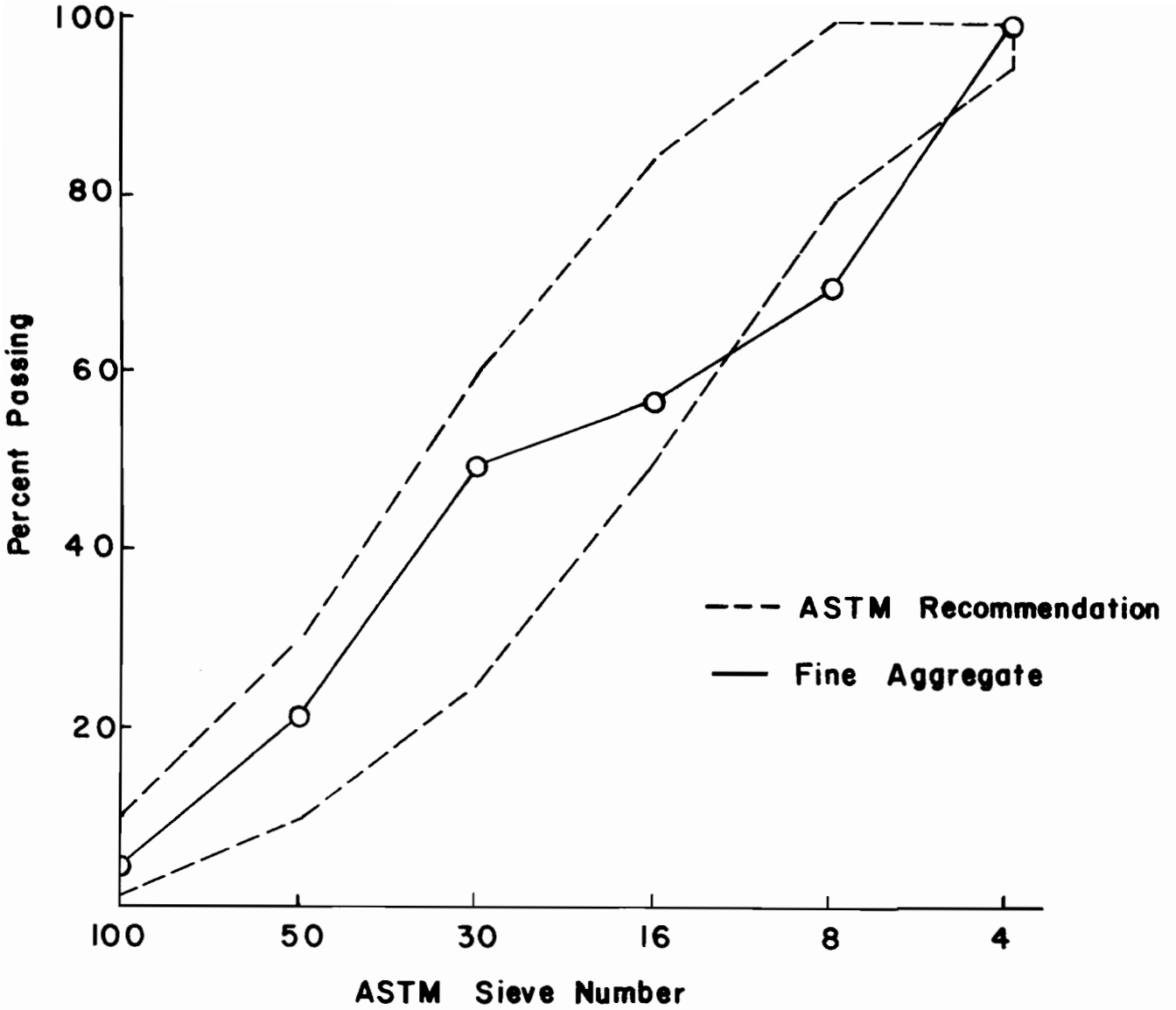

Fig. 8. Fine Aggregate Distribution and ASTM Recommendation

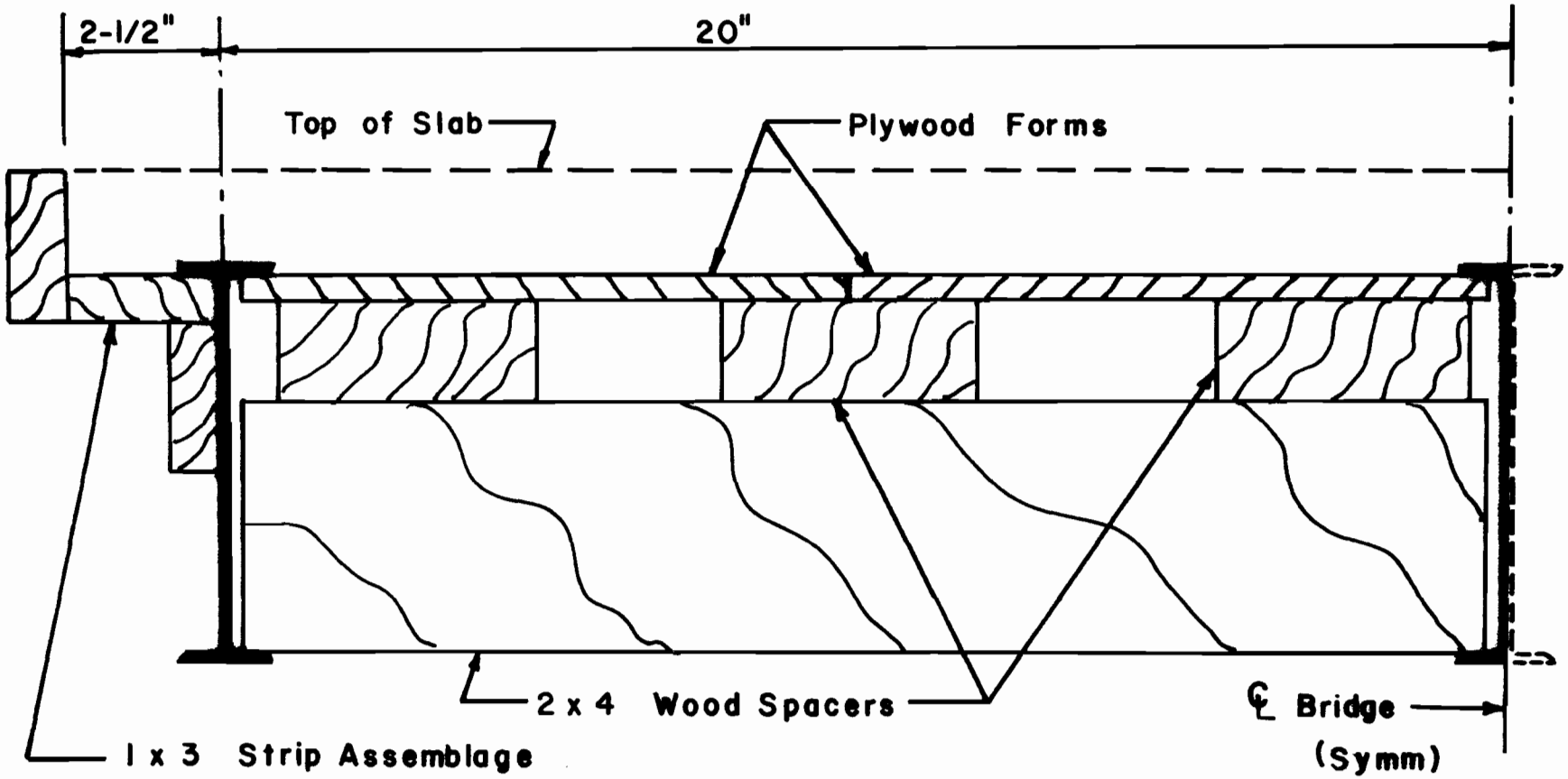

Fig. 9. Deck Formwork

(25 x 76-mm) fir strip assemblages clamped to the outer stringers. All wood form members were given two coats of commercial grade form oil. It was not necessary to shore the formwork. As shown in Fig. 9, the forms were placed beneath the top flange. The design depth of the slab was 1.5 in. (38 mm) above the stringers. Thus, the slab depth between stringers was about 1.65 in. (42 mm) (slab depth plus flange thickness).

III. INSTRUMENTATION

Instrumentation was installed to record temperatures, strains, and displacements at selected points on the structure. To achieve this, thermistors, electric resistance strain gauges, and dial indicators were used. The application and method of attachment varied for different usage and locations on the structure. An automatic data recorder was used to record all the readings except for the dial indicators. The data recording system included two switch and balance units, a 100 channel thermistor stepping unit, an automatic scanner, and a paper tape perforator (Fig. 10).

The strain gauges were Micro-Strain, model 6C-2x2-120 w/L. These gauges had a gauge factor of 2.05, resistance of 120 ohms, grid size of 1/4 x 1/4 in., (6.4 x 6.4 mm) and an overall size of 3/8 in. by 5/16 in. (9.5 x 7.9 mm). The gauges were carbon steel temperature compensated with a factor of 6.0×10^{-6}/F (10.8×10^{-6}/C).

Gauges on the abutment piling and the center pier were mounted with BLH EPY-150 two-part epoxy. This epoxy cures at room temperature and withstands usage up to 150 F (66 C). Surface preparation of the steel consisted of removing scale, degreasing, sanding and conditioning. A uniform mounting pressure of 10 psi (69 kN/m^2) was applied to each gauge during the epoxy curing period.

The adhesive used for the gauges mounted on the stringers was Micro-Measurements M-Brand AE-15 two-part epoxy. This epoxy exhibits essentially creep-free performance up to 200 F (93 C) when cured at temperatures 25 F (14 C) greater than maximum operating temperatures. Surface preparation and mounting followed the procedures described above. Heat lamps focused on the stringers produced a cure temperature

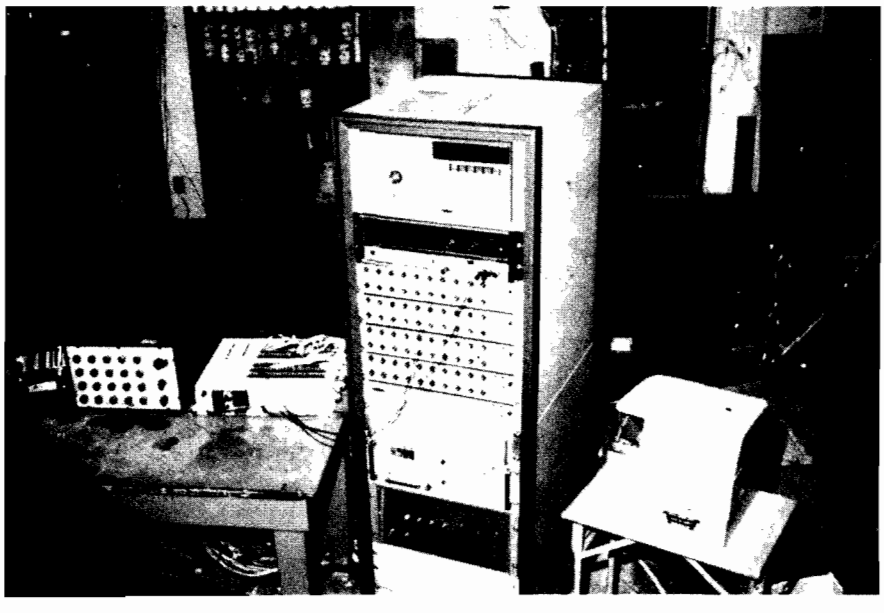

Fig. 10. Data Recording System

of 190 F (88 C).

Special consideration was required for the preparation of the strain and temperature transducers to be placed in the slab. A material approximating the thermal and mechanical properties of concrete was sought for mounting the strain gauges and thermistors. After a lengthy search and review, glass microscope slides were chosen. Neat cement paste cubes were not considered because of their lack of tensile strength, which could lead to loss of the gauges if tension occurred in the section. The thermal values of conductivity and coefficient of expansion of the slides and concrete are quite similar. The mechanical properties of the glass and the concrete matched very well except for Young's modulus which has a ratio of 3:1, the glass being the stiffer material. If steel had been used, a ratio of 10:1 would have been obtained with steel being the stiffer material.

The glass used for microscope slides is a high grade soda-lime glass, which has a low alkali content. Thus, any possible alkali reaction with the concrete mixture had minimal, if any, adverse effect on the slides. The slides were 1 x 3 x 1/10 in. (25 x 76 x 2.5 mm) and had a coefficient of linear thermal expansion of 5.0×10^{-6}/F (9×10^{-6}/C), a thermal conductivity of 0.53 Btu/hr-ft-F (.92 W/m-C) and a Young's modulus of 10.3×10^{6} psi (71×10^{6} kN/m^2).

Potential problems that might arise from a heat sink were avoided by using a material with a thermal conductivity similar to that of the concrete. A material having a higher conductivity would have caused a more rapid heat flow through the deck and would have reduced the temperature gradient between the surfaces. The glass slides also had a thermal coefficient of expansion almost that of concrete. This

reduced the local stress concentrations induced by materials acting against each other. In essence, the closer the properties are matched, the more closely the true strain state in the slab can be measured.

The mounting surfaces of the slides were scored with abrasive paper to improve the adhesion of the gauges. After the slides were degreased the gauges were mounted with the same epoxy that was used for the stringers. Here also, a heat cure temperature of 190 F (88 C) was obtained by placing heat lamps below the metal channel that was used to hold the slides and the weights required to provide a 10 psi (69 kN/m^2) uniform pressure on the gauges. To provide a better mechanical bond to the deck concrete, several 1/4 x 1/8-in. (6.4 x 3.2-mm) slots were cut in the sides of the slides.

The piling and pier gauges were moisture proofed with BLH Barrier E Neoprene. The piling gauges were also covered with small aluminum channels to prevent the sand from abrading them. Several light layers of beeswax were used to moisture proof the stringer and slide gauges. Twenty-two gage Belden wire leads connected the gauges to junction blocks placed about 3 ft (0.9 m) from the gauge locations. Belden 8723 four-strand shielded wire leads averaging 20 ft (6 m) in length were then used to connect the junction blocks and the recording unit. Similar lead arrangements were used for the piling and pier gauges except that they were connected to manual switch and balance units and then to the recording unit. These manual units consisted of one 10 channel Strain-Sert unit and one 20 channel BLH unit.

Fenwal Uni-Curve No. UUA 33J1 thermistors were selected for the temperature sensors. These thermistors are epoxy encapsulated temperature sensitive resistors with a maximum spherical diameter of

0.095 in. (2.4 mm), resistance tolerance of ± 1 percent and temperature tolerance of ± 0.4 F (0.22 C) over a range of 30 - 175 F (-1.1 - 79 C). Actual temperature values were obtained by comparing resistance values to temperatures from a calibration chart. The temperature resistance relationship was programmed for computational ease by using logarithmic equations that gave values within ± 0.2 percent of the chart values.

A two-part metal filled epoxy was used to attach all the thermistors to their base locations. Metal filled epoxy was used to provide better heat conduction from the base material to the thermistor mounted flush on the base. Leads from the thermistors consisted of coaxial cable (similar to Belden 8216) leading to a stepping unit. Thermistor-cable connections were enclosed in heat-shrinkage tubing to prevent the invasion of moisture.

The total longitudinal deck deflection and vertical deflection at midspan was recorded by using dial indicators with a least count of 0.001 in. (0.025 mm). The indicators for vertical deflections were mounted on wooden standards, whereas the indicators at the abutments were attached to metal channels that were rigidly attached to the sandbox frame. The dial indicator assemblies are shown in Figs. 11 and 12.

All the thermistor leads entered a 100 channel stepping unit which interfaced with the automatic recorder. This unit, which allowed for automatic stepping, eliminated any hand switching. Resistance values entered directly into the recording unit, which employed a Wheatstone bridge balance scheme. The recorder output was a voltage reading, which was input into a digital computer and converted by simple circuit relationships directly back to resistance, which in turn was converted to a temperature.

Fig. 11. Midspan Dial Indicator

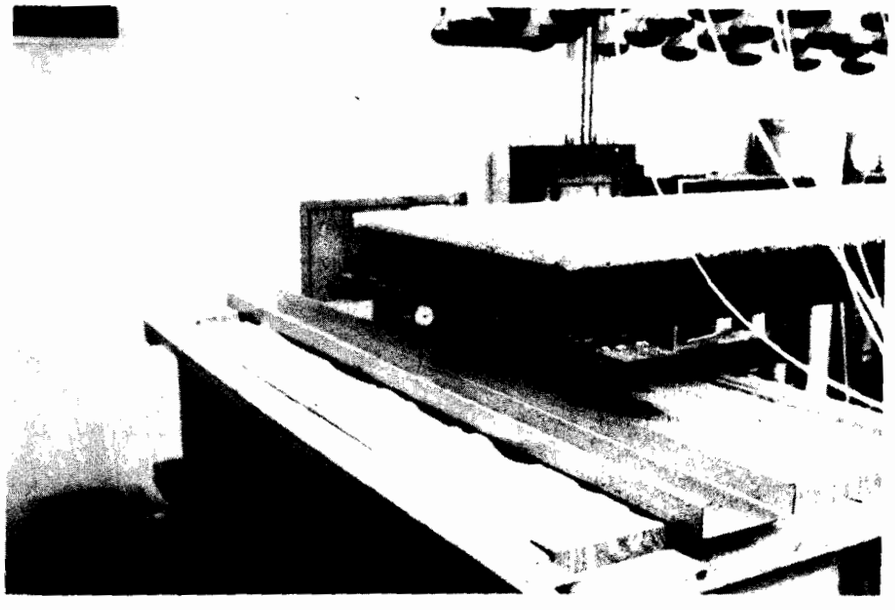

Fig. 12. Abutment Dial Indicator

The recording unit was a commercial automatic scanner with 40 channels available for strain gauges plus receptacles for the connection of the external stepping unit that was used for the thermistors. The thermistors could then be scanned immediately after the 40 recorder channels had been scanned. Thirty-six channels were connected directly to individual gauges from the bridge deck and the stringers and two channels were used to connect the two switch and balance units. Hand switching these two units through the recorder permitted a hard copy recording of values.

Coupled with the automatic recorder was a paper tape perforator, which gave a hard copy of all the readings. The tape was subsequently read into a minicomputer which formatted and sent the recorded values through a remote terminal directly into data files of an IBM 360-70 computer for data reduction.

A. INSTRUMENTATION ORIENTATION

To ascertain the piling strains resulting from thermal induced movement, gauges were mounted on the abutment piling and the center pier as previously described. Strain gauges were mounted on opposite faces of the piling at the same elevation as shown in Fig. 13.

Gauge placement on the center pier is shown in Fig. 14. Before placing the stringers, all the gauges were read in calibration tests to verify the cantilever action of the pier (linear variation in strain from top to base), but only the values from the two lower pairs were recorded during the thermal tests.

In addition to the piling and pier gauges, five locations were chosen for the placement of the transducer groups. Two groups were distributed through the deck midway between the stringers. The other

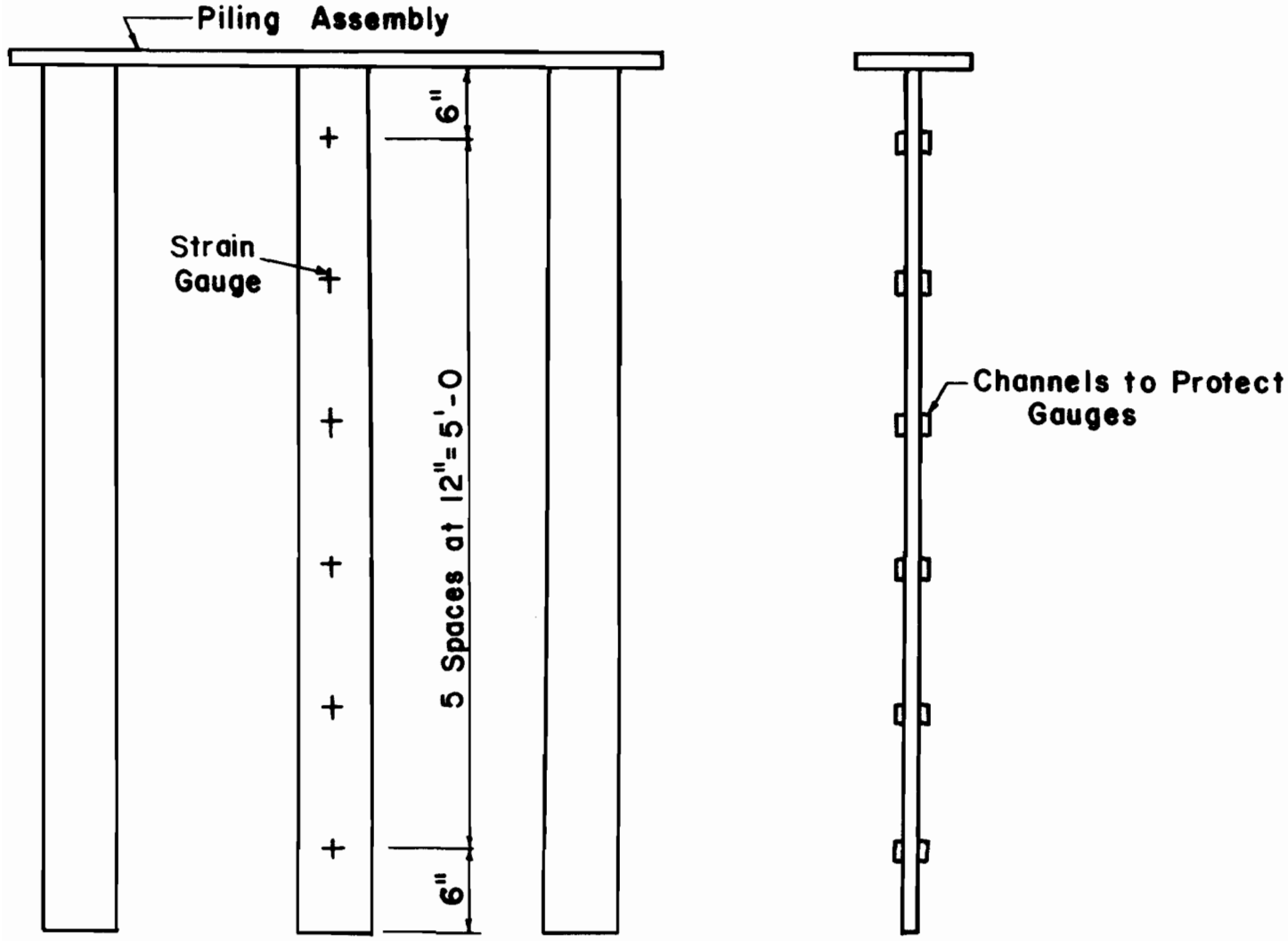

Fig. 13. Gauge Placement on Piling

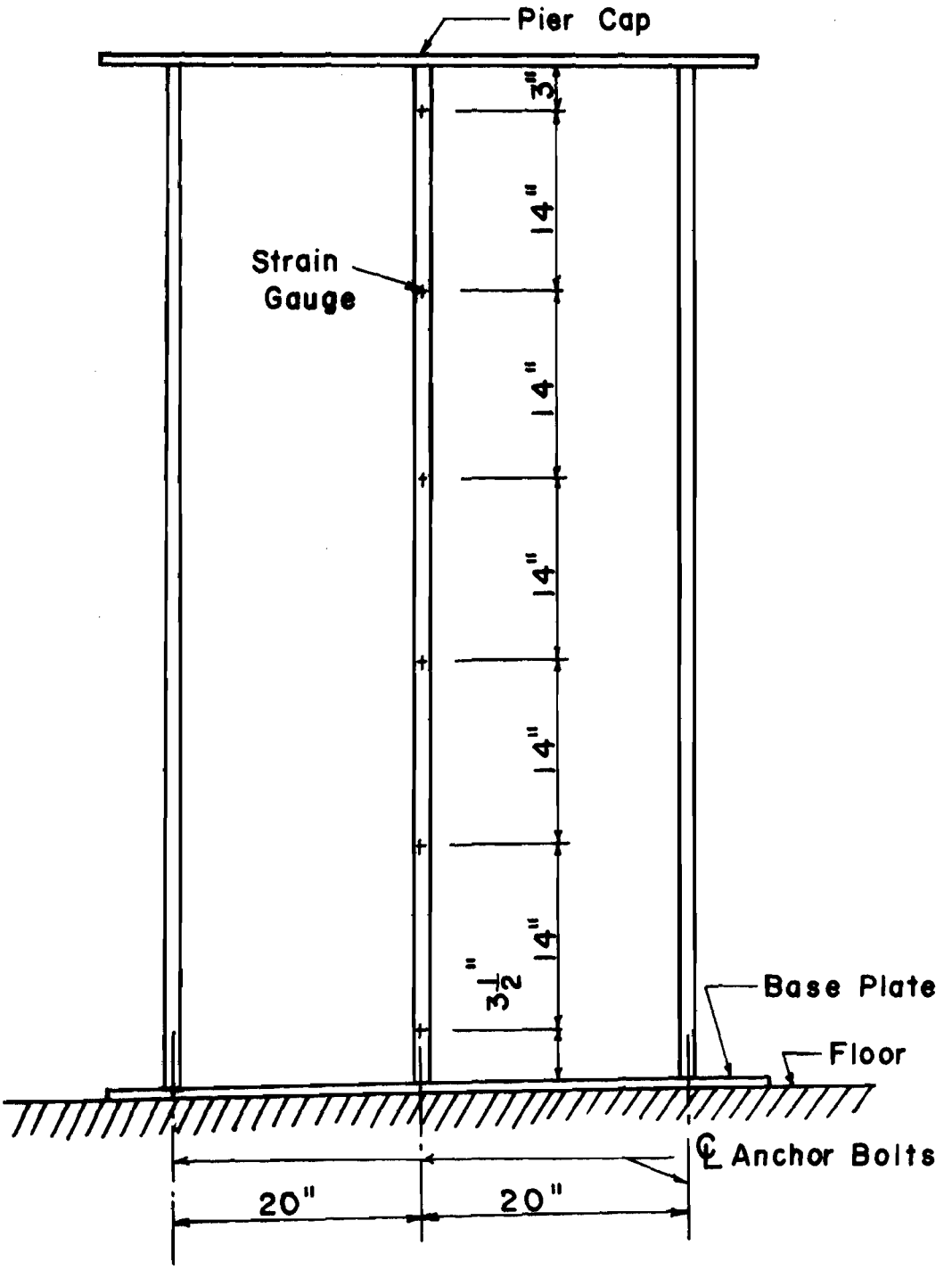

Fig. 14. Gauge Placement on Pier

three groups were placed on and immediately over the center stringer. Both thermistors and strain gauges were used in these groups. A plan view of the location of each group is shown in Fig. 15.

A slab transducer consisting of a glass microscope slide, strain gauge, and thermistor is shown in Fig. 16.

As shown, the gauge and thermistor leads were directed from opposite ends to help eliminate congestion and air voids in the deck when placing the concrete.

Thermal induced strains were read at the top, bottom, and four intermediate points of the slab at locations 2, 3, and 4. To achieve the proper vertical positioning of the slide transducers, small diameter plastic straws were glued to each corner of the bottom of the slides and to the top of the stringer or wooden forms, depending on location. Plastic straws were used because they would not act as heat sinks and were flexible enough to rebound to their proper position if displaced during slab placement.

Locations 1 and 5 in Fig. 15 had slab instrumentation only. These areas are midway between the center stringer and an outside stringer. Plan and elevation views of the small slab cantilever reference bar at location 1 are shown in Fig. 17, and plan and elevation views for the bars at location 5 are shown in Figs. 18 and 19, respectively. These reference bars were enclosed on three sides by 1/2-in. (13-mm) thick flexible styrofoam. Wire mesh was not used in these sections so that the concrete could expand freely as a result of thermal change and give an indication of unrestrained thermal expansion. The styrofoam produced essentially no resistance to small expansive movements and provided insulation between the boundaries. This kept the thermal

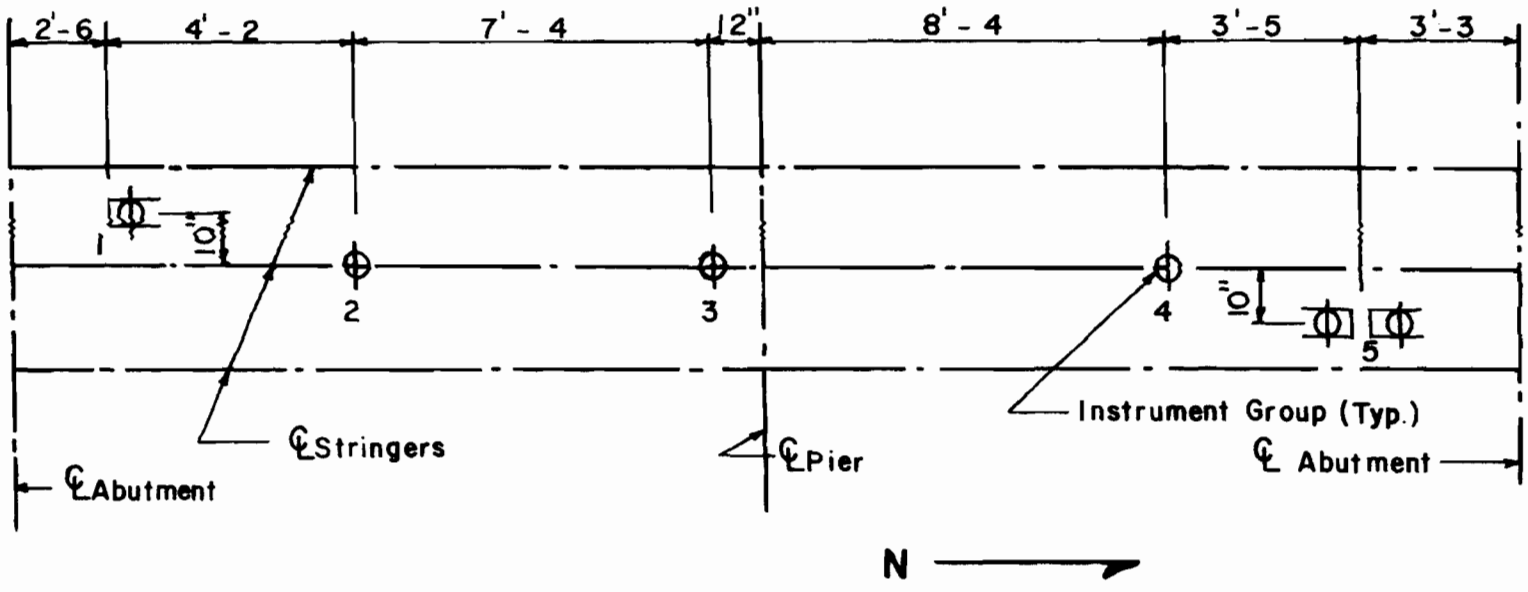

Fig. 15. Plan View of Deck Instrumentation Groups

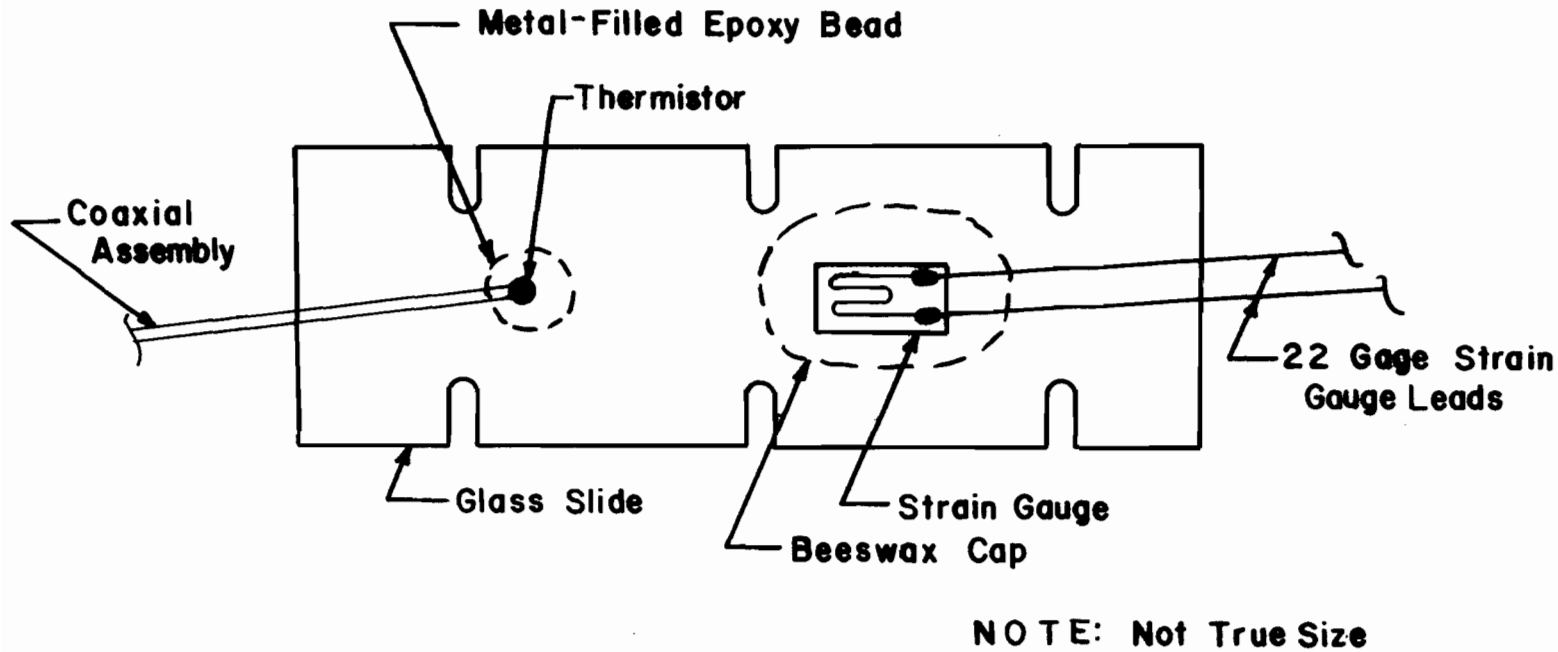

Fig. 16. Slab Transducer

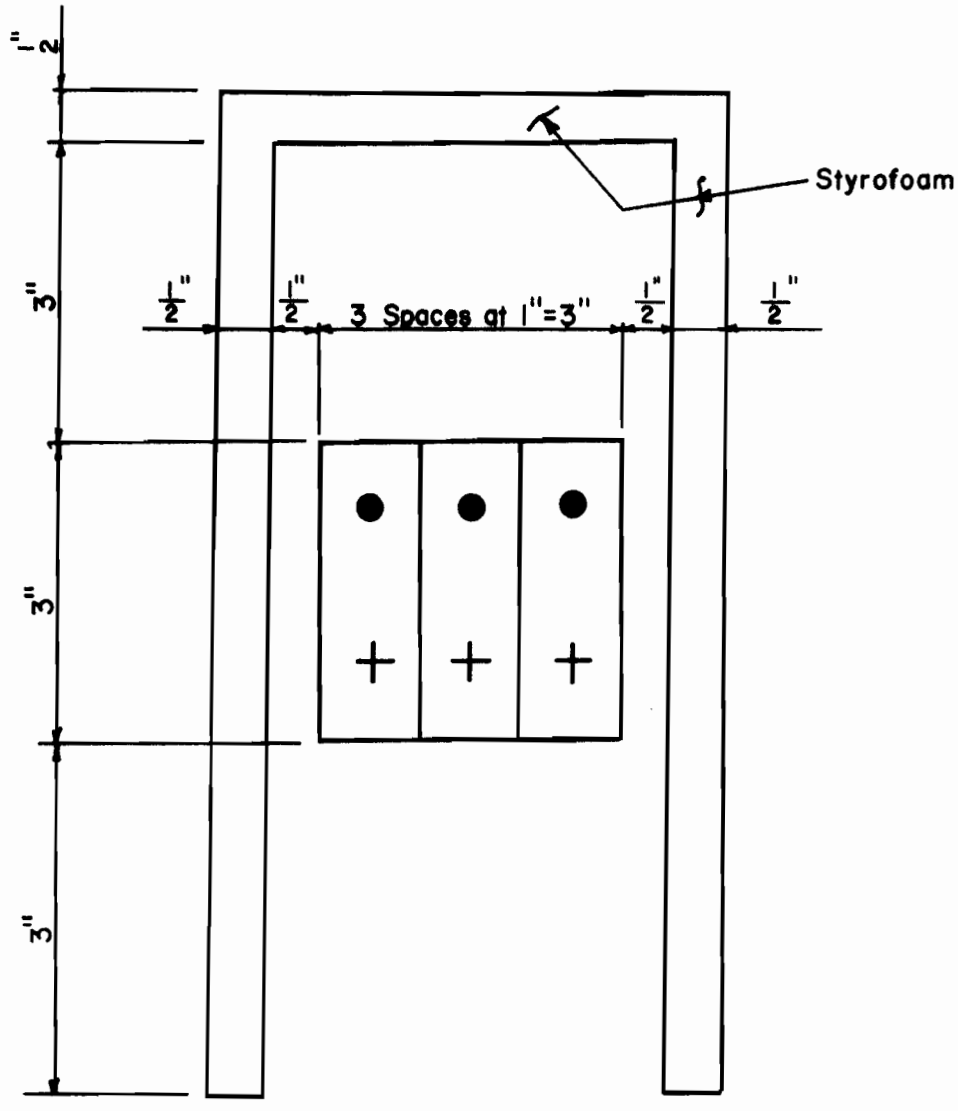

a) Plan View

● Thermistor

+ Strain Gauge

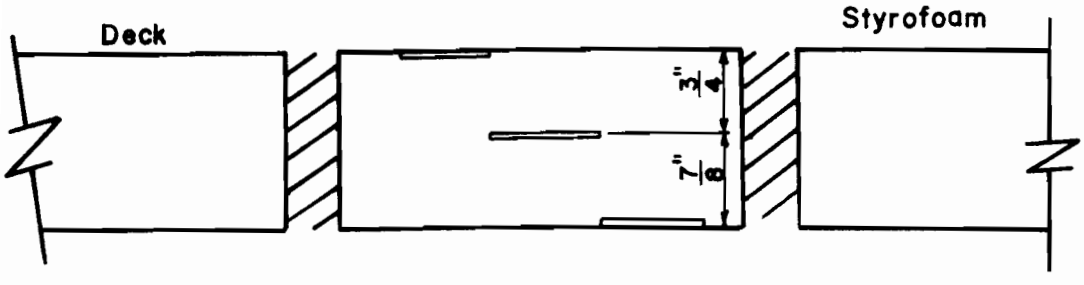

b) Elevation

Fig. 17. Reference Bar Instrumentation at Location 1

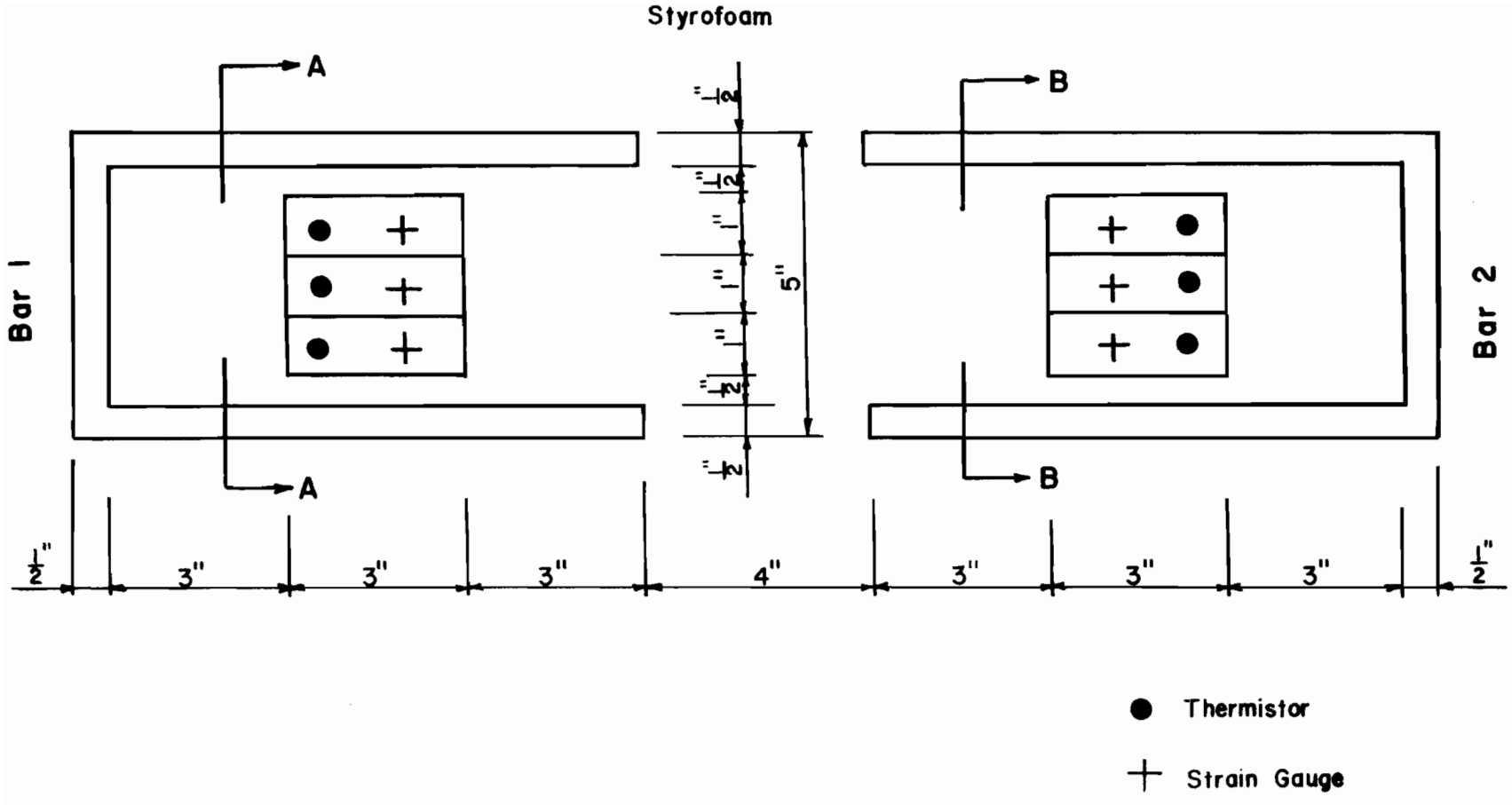

Fig. 18. Plan View of Reference Bar Instrumentation at Location 5

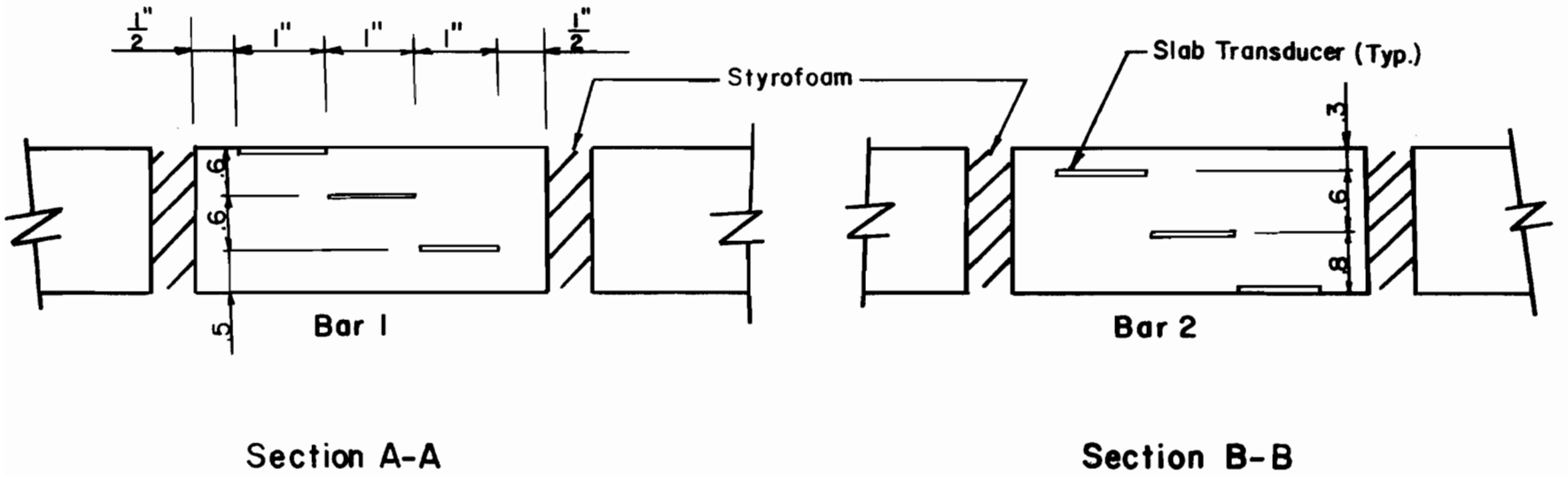

Fig. 19. Sections of Reference Bars at Location 5

gradients intact that would have otherwise been altered by an air space. The thermal gradients and temperatures obtained were then representative of any point through the deck between stringers.

At location 5 (Fig. 15), the transducers were distributed in two groups to avoid congestion in the slab and possible interference in the readings.

Instrument locations 2, 3, and 4 were at sections along the center stringer. As previously noted, strain gauges and thermistors were placed at six points vertically through the deck slab. The sixth or lowest point was the interface between the slab and stringer, and at this point the gauge and thermistor were attached to the top flange of the stringer. Seven thermistors were evenly spaced down the stringer web, and two were attached to the bottom flange, one at the outer edge of the flange and the other directly beneath the web. Strain gauges mounted on the top and bottom flanges were placed 1/4-in. (6.4-mm) on either side of the centerline of the flange. A typical plan view and an elevation of this instrumentation are shown in Fig. 20. The slab transducers were staggered to avoid excessive congestion and placement problems.

Dial indicators with a least count of 0.001 in. (0.025 mm) were used to obtain the vertical deflection of the center stringer at midspan (locations 2 and 4 of Fig. 15) and the longitudinal deck displacement at each abutment. The total deck movement at the bearing elevation was obtained by summing the abutment displacements.

In addition to structure instrumentation, thermistors were positioned 3, 6, and 12 in. (7.6, 15, and 30 cm) above and below the slab to give an indication of the still air temperature and thermal gradients around the bridge. Thermistors above the deck were shaded

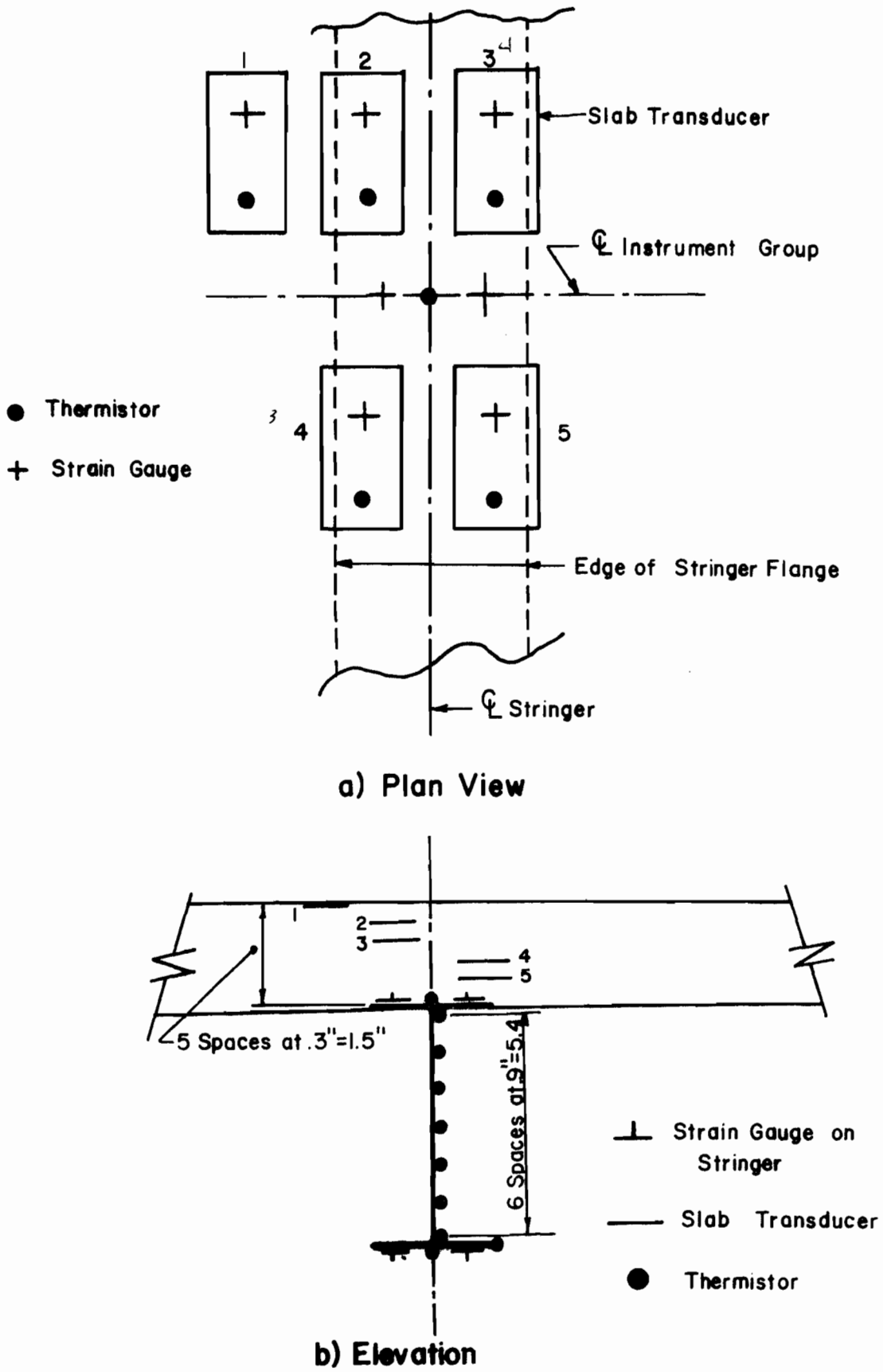

Fig. 20. Slab and Stringer Instrumentation

from the heat lamps in order to obtain readings unaffected by incident radiation.

IV. TESTING

A. PRELIMINARY TESTING AND CALIBRATION

Before the stringers were erected, an experimental determination of the stiffness characteristics of the abutments and the center pier was needed to provide data required for a theoretical computer analysis of the indeterminate structure (to be compared with experimental results) and for reducing the data to be obtained from thermal loading of the test structure.

Horizontal loading for both the pier and the abutments was applied by a cable and pulley system as shown in Fig. 21a. Moment or rotational loading on the abutments was provided by means of a rigid bar as shown in Fig. 21b. The magnitudes of the loading force were measured by load cells that were fabricated for the tests by mounting strain gauges on cold-rolled steel strips. Horizontal displacements were measured with dial indicators having a least count of 0.001 in. (0.025 mm). Abutment rotation was measured as shown in Fig. 22. The vertical bar, which was very stiff, was rigidly attached to the piling cap plate, and the dial indicators were mounted on a frame independent of the sand boxes. The piling cap rotation was calculated as the difference in dial indicator readings divided by the distance between the indicators.

Load-deflection and load-strain curves were drawn for the center pier. Load-deflection, load-strain, moment-rotation, and moment-strain curves were developed for the abutment piling. Typical curves are shown in Figs. 23 through 27. For calibration of the pier, all the strain gauges were used. During the thermal tests only the lower two pairs were used.

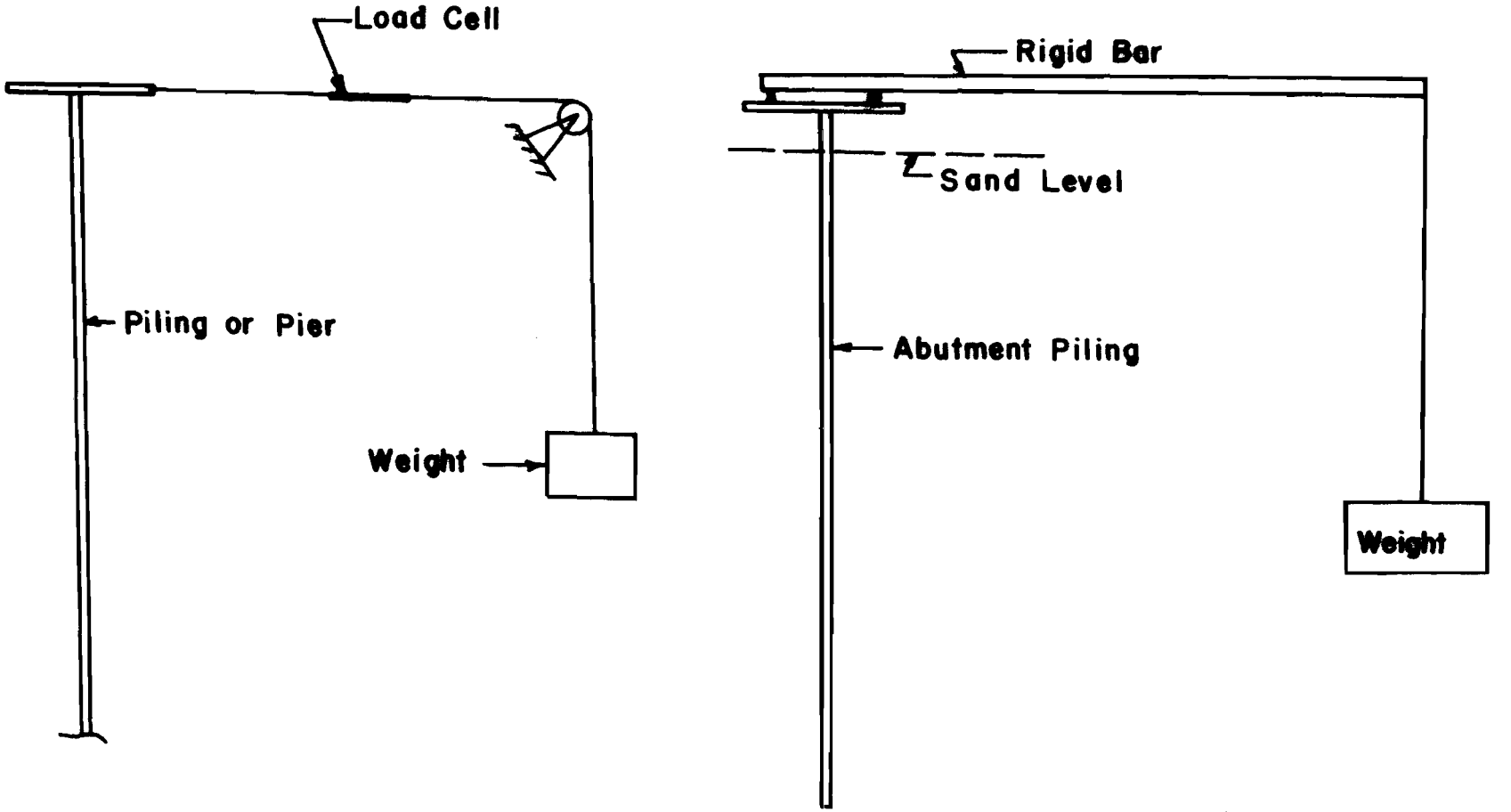

Fig. 21. Loading for Abutment and Pier Calibration

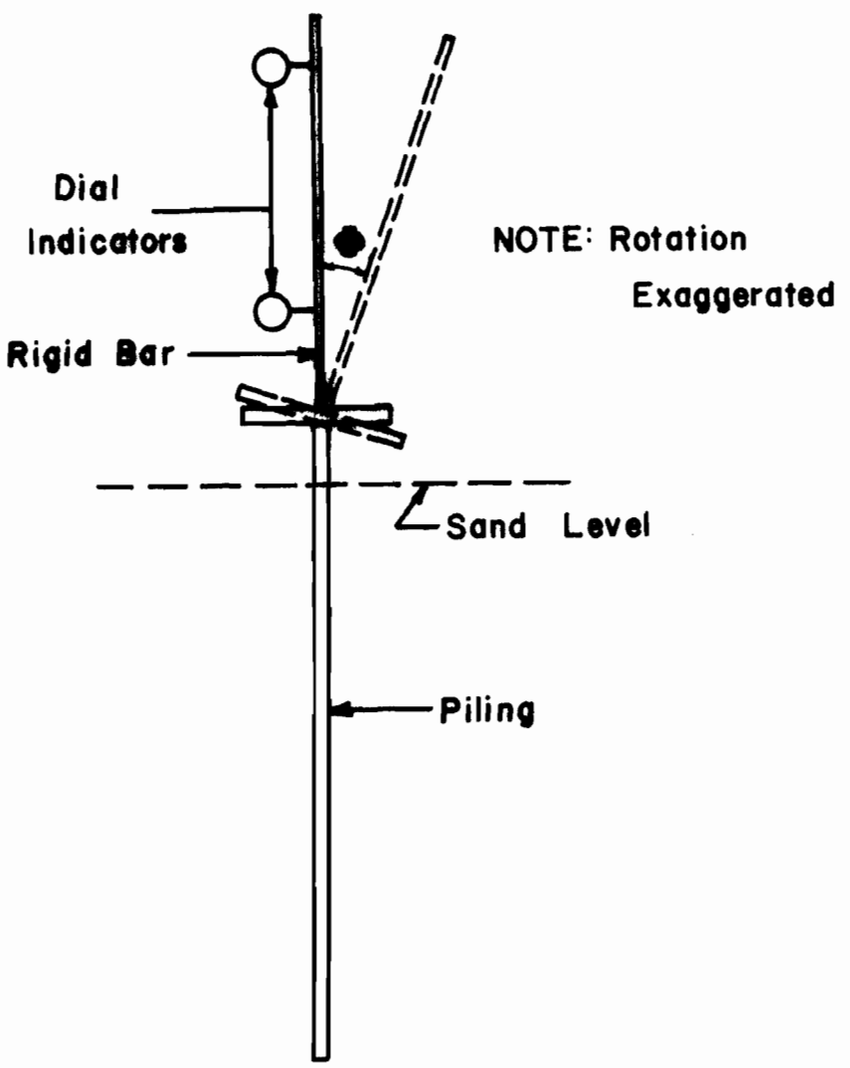

Fig. 22. Measurement of Abutment Pile Rotation

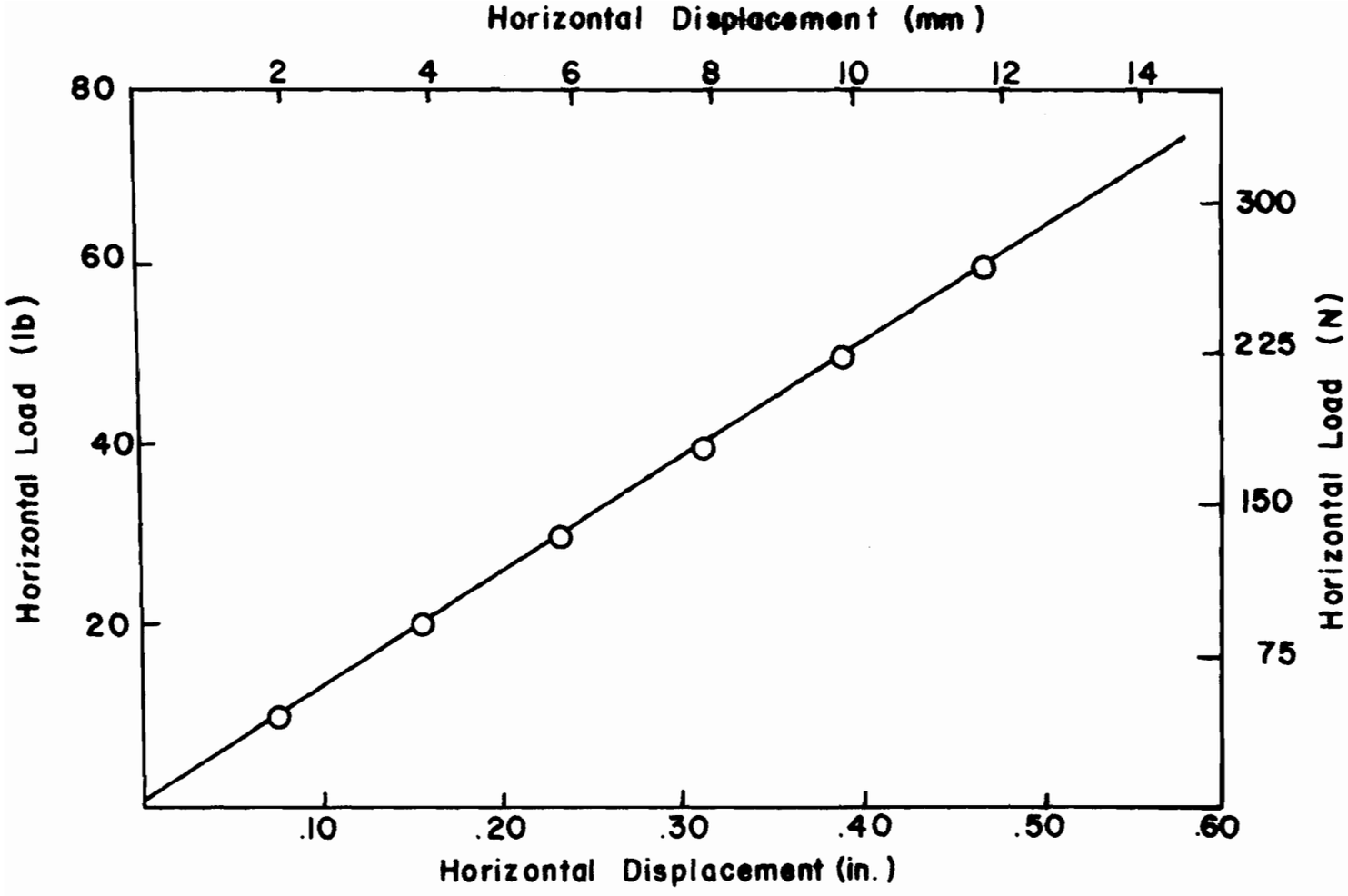

Fig. 23. Center Pier -- Load - Displacement Calibration

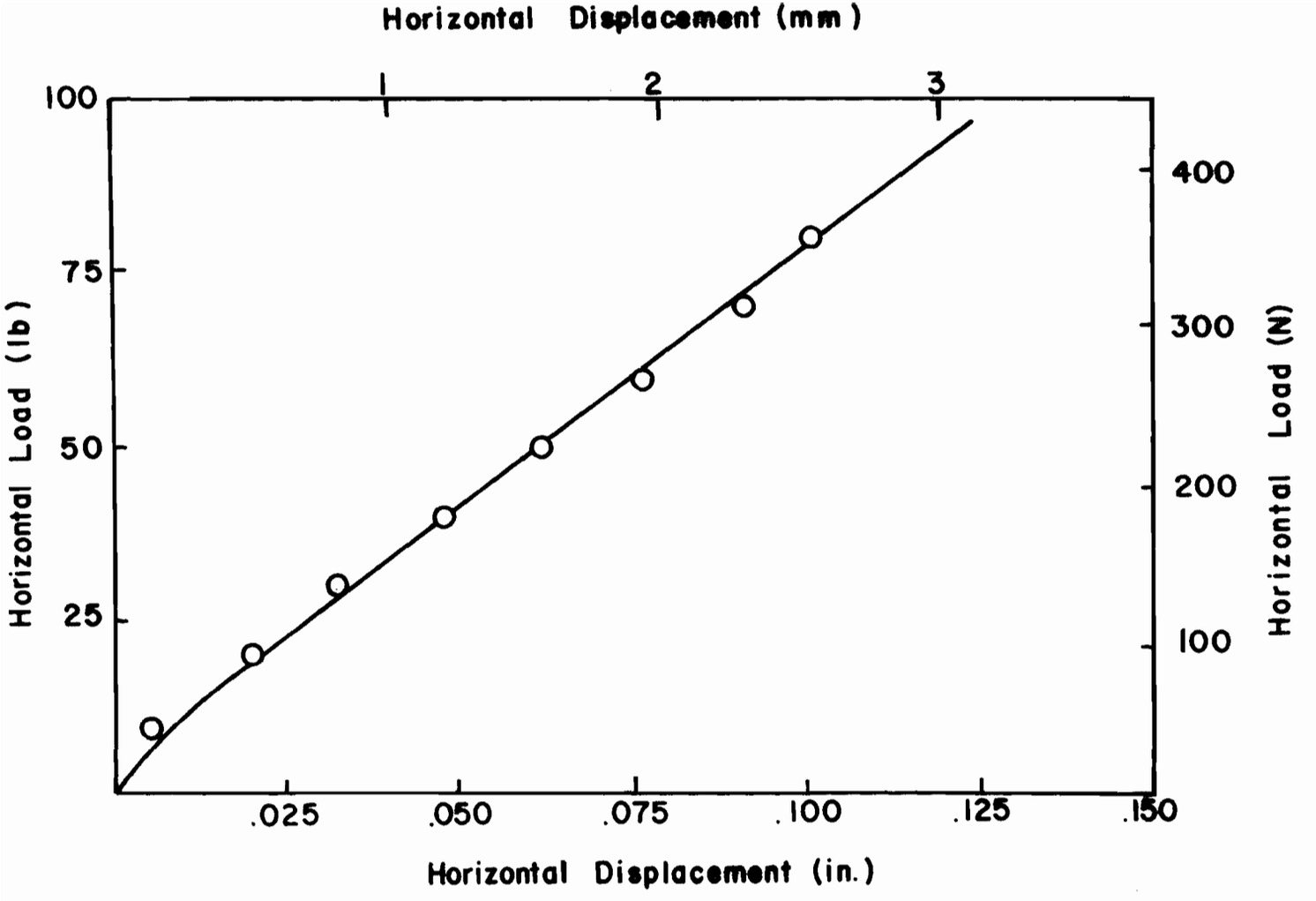

Fig. 24. Abutment -- Load - Displacement Calibration

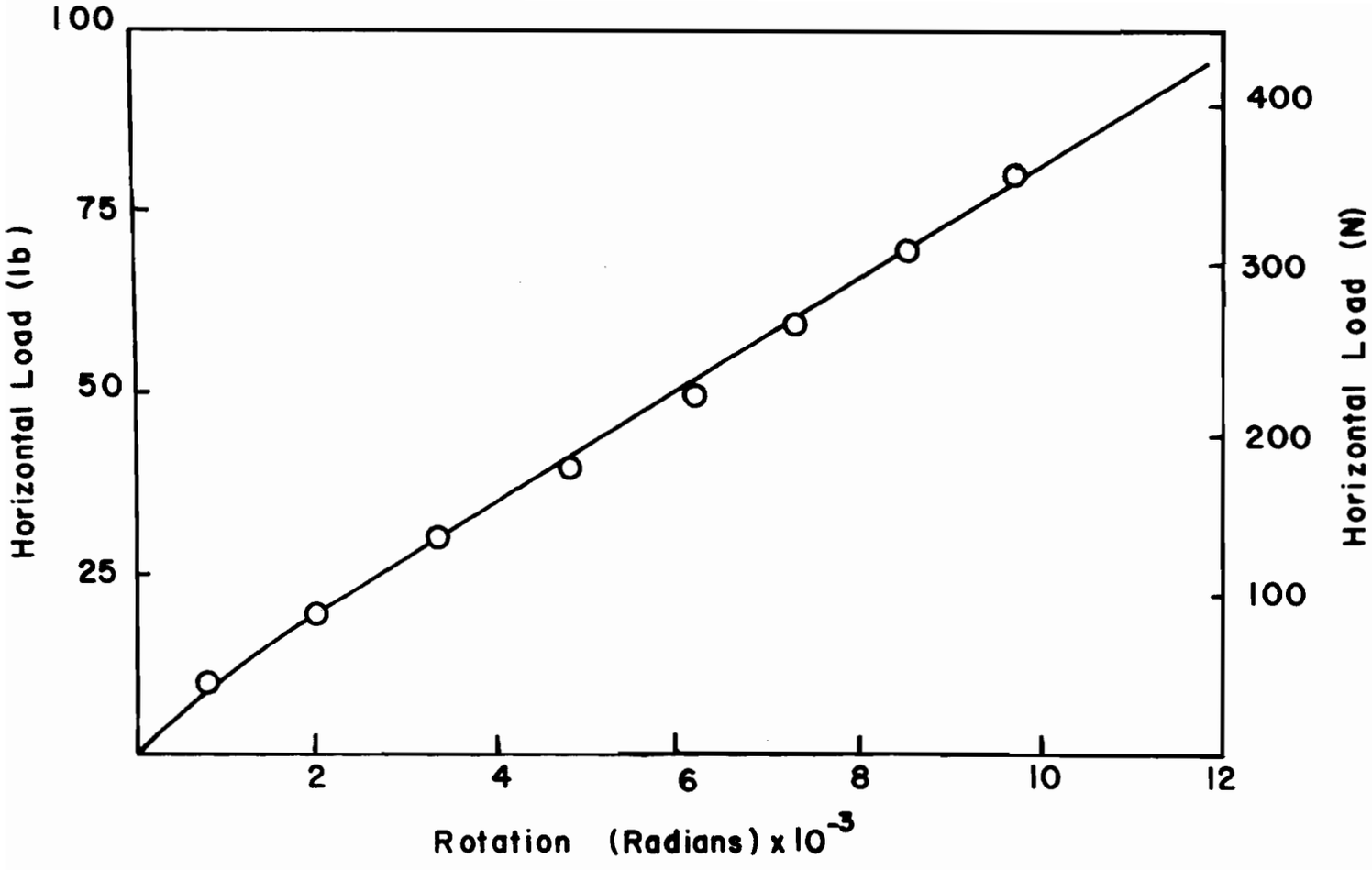

Fig. 25. Abutment -- Load - Rotation Calibration

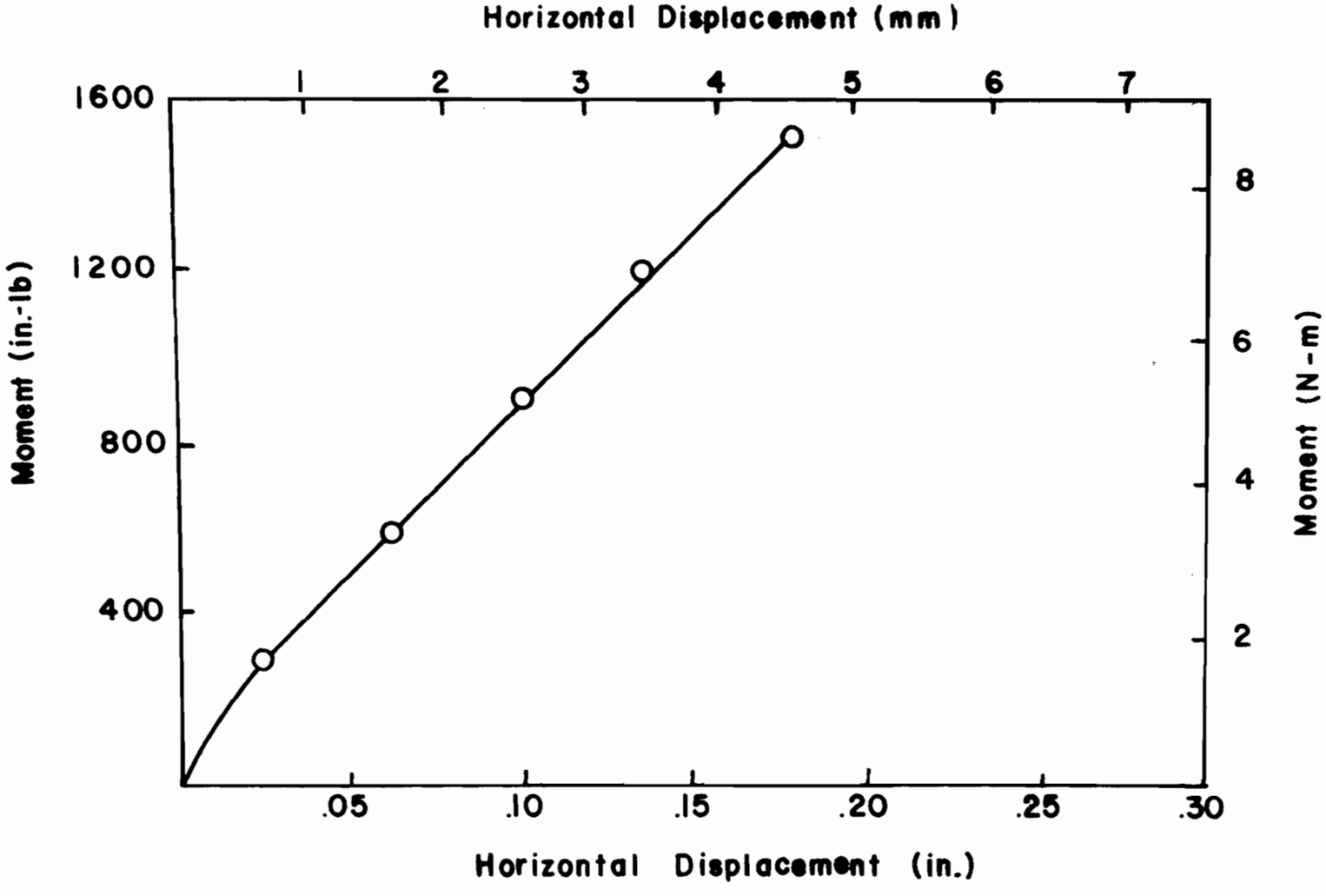

Fig. 26. Abutment -- Moment - Displacement Calibration

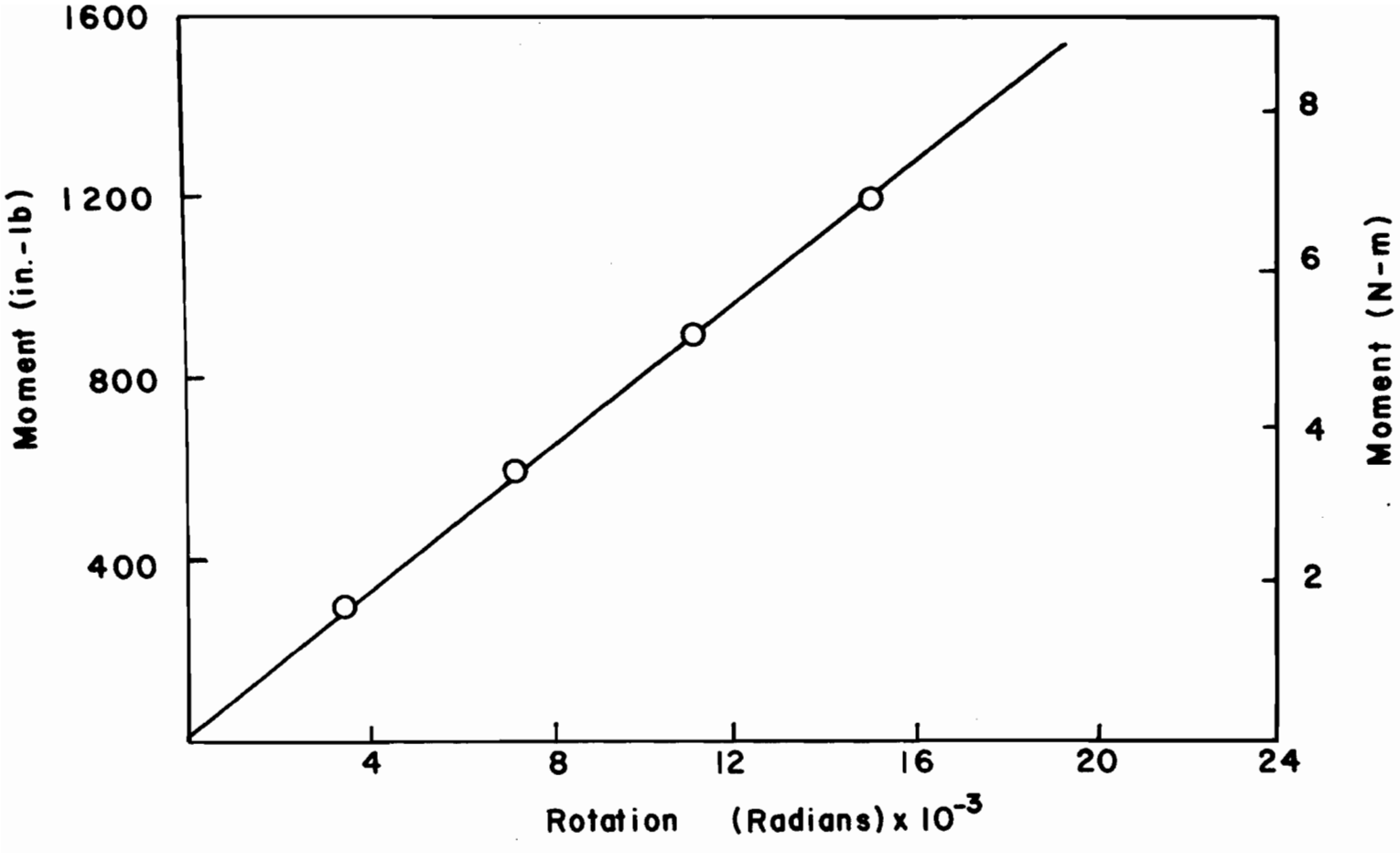

Fig. 27. Abutment -- Moment - Rotation Calibration

A stiffness matrix was formulated from the abutment calibration curves. The relationships in the matrix consisted of rotations and horizontal displacements produced by an applied horizontal force or moment. The matrix (symmetric and of the order of two by two) was used to obtain abutment rotations, which were induced by thermal loading of the test structure, from the observed piling strains and horizontal displacements.

The abutment piling calibration curves were found to be dependent upon the loading sequence. If either moment or horizontal loading induced deflection in the same direction as the previous loading, e.g., a horizontal deflection of north-north or south-south for two successive loadings, the soil stiffness was considerably greater than for a reversed loading sequence, e.g., a north-south or south-north deflection sequence. Consistent values were reproduced for repeated loadings in the same direction.

Final stiffness matrix values were chosen from the repeated sequence tests. The values, which indicated the stiffer of the two possible matrix relationships, were chosen because only a heating-cooling (e.g., room temperature to test temperature to room temperature) sequence was used in thermal loading of the test structure. This produced initial outward piling displacements. This is analogous to field conditions in the summer. Usually, hot days follow warm or hot days, and bridge abutments follow the same basic deflection path during a particular season. This effect is much more pronounced in sand model tests than in clay or actual field conditions.

The load-sequence stiffness variation can be explained by the soil particle dislocation and movement in the vicinity of the piling near the

sand surface during load reversals. This behavior is prevalent near the surface of a cohesionless soil, because particles near the back side of the piling will tend to slough when the pile is deflected. As a gap or void develops between the soil mass and the piling, the soil fails and fills the gap. The soil area affected by the movement then has a different density. Upon reversal of the pile loading, the soil is redensified. After this redensification, the soil will act to some extent as an elastic medium during repeated testing, if the displacements are not large enough to bulge the soil on either side of the piling in the direction of movement.

B. HEAT SOURCE

The test structure was thermally loaded by using General Electric model 250R40 250 watt infrared reflector heat lamps. These lamps emitted a radiation level that was partially absorbed by the deck and in turn heated the bridge structure. Radiation heating was chosen rather than a constant temperature heat source, because it was simpler and approximated actual field conditions imposed by the sun. The lamps were placed in four rows along the length of the bridge and were spaced 12 in. (30 cm) center-to-center both longitudinally and transversely. Alternate rows were staggered 6 in. (15 cm) as shown in Fig. 28a to provide a more uniform radiation level. The 12-in. (30 cm) spacing was selected for uniformity of heat distribution and also to provide a deck temperature of approximately 150 F (66 C). The bulb faces were placed 20 in. (51 cm) above the deck in accordance with the manufacturer's recommendation for the distance of the lamp from the heated subject being at least 1.6 times the lamp spacing (1.6 x 12 = 19.2 in. [49 cm]) for uniform radiation distribution. Ceramic lamp

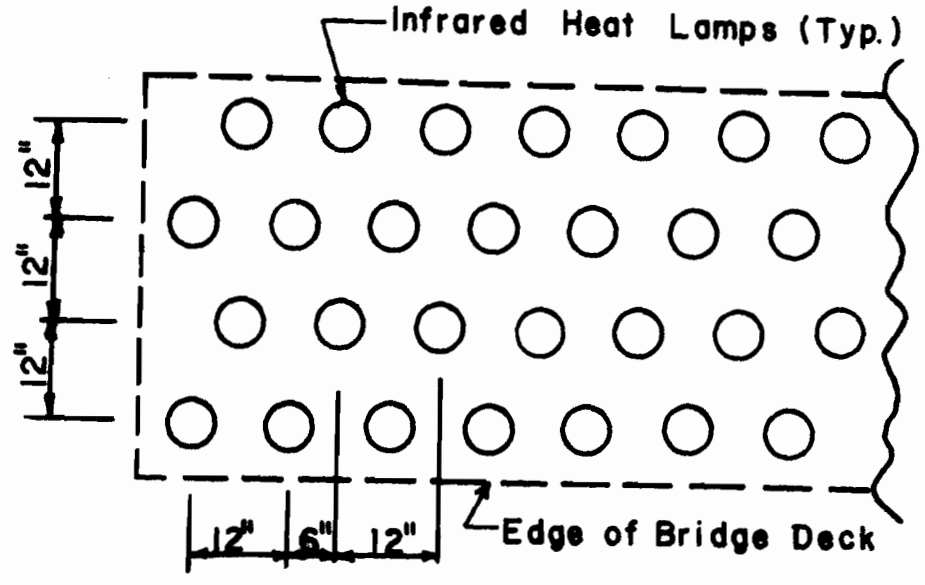

a) Heat Lamp Placement

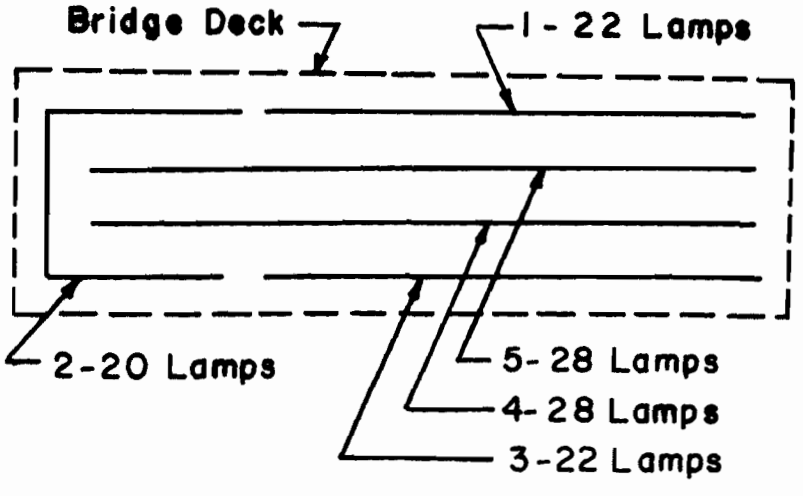

b) Variac Circuits

Fig. 28. Heat Lamp Details

sockets were mounted on a wooden frame and the lamp assembly was suspended from the ceiling as shown in Fig. 29.

Five 240-volt Variac transformers were used to vary the thermal loading. Each Variac controlled 20 to 28 heat lamps as shown in the circuits of Fig. 28b. The emitted radiation varied with the applied voltage. The design voltage for the lamps was 115 volts, and the output capacity of the transformers was 240 volts. Hence, the lamps were connected in series by pairs to split the voltage output. These pairs were then connected in parallel to complete a transformer string. Thus, the lamp input voltage could be varied up to 120 volts. The voltage drop through the wires was less than one percent, because the transformer leads were connected to the center of a bulb string. All leads and couplers consisted of 12 gage wire.

The maximum transformer voltage output was 240 volts with a rated amperage of 28 amps. Input to the transformers was 220 volts single phase. Only 190 volts could be input to the two center strings of lamps without exceeding an amperage of 28 amps. This voltage then became the critical level, and the temperature resulting from this loading became the maximum possible. The full voltage of 240 volts could be input to the outside strings, because there were a smaller number of lamps per string.

To obtain uniform heat flux, the outside circuits required a higher voltage input than the interior circuits because the overlap of radiant energy along the edges was not as pronounced as in the center. To check the uniformity of the heat flux, a heat receptor was fabricated. This consisted of a 5 x 3 x 1-in. (127 x 76 x 25-mm) carbon steel bar painted flat black on one of the 5 x 3-in. (127 x

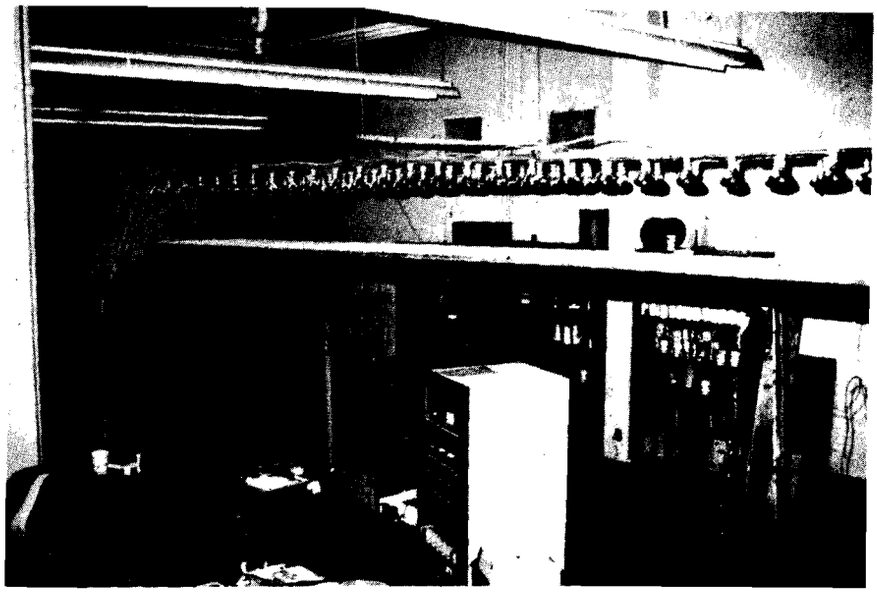

Fig. 29. Heat Lamp Assembly

76-mm) surfaces. Thermistors were placed on both surfaces and the bar was encased in styrofoam to prevent the loss of heat from the sides and to limit the convection to the top and bottom surfaces. The painted side was exposed to the radiation and the opposite face to ambient air as shown in Fig. 30. By moving the receptor to different points on the bridge deck and observing the steady state temperature of the receptor, the uniformity of radiant energy could be checked and the voltages adjusted to give the most uniform heat flux.

C. TESTING PROCEDURE

Thermal testing began when the test structure was completed and the initial instrumentation and heat source problems were resolved. Several transverse hairline shrinkage cracks across the deck occurred at random intervals along the length of the structure. These cracks resulted from shrinkage of the concrete during curing and subsequent moisture loss during testing. The cracks had no apparent effect on structural integrity; the shear connectors appeared adequate and both top and bottom reinforcement was used in the slab. No attempt was made to replace moisture lost from heating during testing, and the only source of moisture gain was the atmosphere of the laboratory.

Prior to any testing cycle, the laboratory was sealed to eliminate any outside drafts. Heating and air return ducts were sealed, door cracks taped, and outside openings covered with plastic. Thus, the only source of forced convection would be air currents caused either by heat gradients above and below the test structure developing into a cyclic draft as a result of the laboratory's high ceiling or by cross currents developing between the warm and cool ends of the large laboratory. During testing, these effects were found to be negligible;

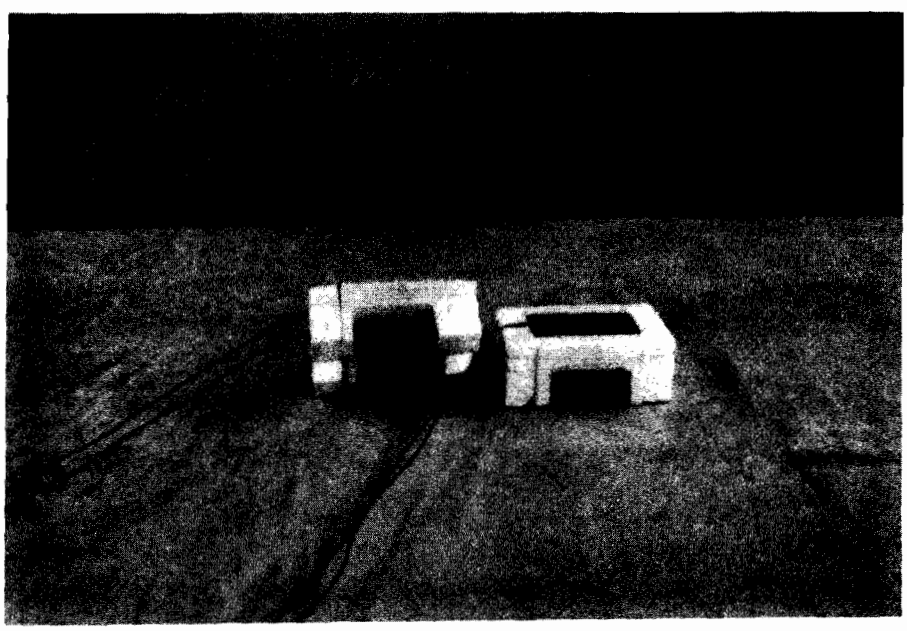

Fig. 30. Heat Receptors

consequently, a condition of free convection existed between the bridge and the surrounding atmosphere.

All strain gauges and dial indicators were zeroed prior to each test cycle. The bridge and ambient air temperatures were recorded and used as the reference temperatures at zero strain. The transformers were then turned on and adjusted for each circuit until an even incident heat flux on the deck was produced by the heat lamps. Uniformity was checked by observing the temperature of the heat sensor (previously described) when it was placed at different locations on the bridge deck. Subsequent adjustments were made as required.

Steady state temperatures through the cross section were achieved after seven hours of heating. Strain gauge and thermistor readings were recorded automatically by the data acquisition unit. Dial indicator readings were observed visually and hand recorded. Recorded values from the test structure included longitudinal strains and temperatures at previously described points on the stringer and in the slab. The lower two sets of strain gauges were located on the center pier and used to determine the lateral movement of the pier, and the upper two pairs of strain gauges were positioned on each abutment to determine the piling deformations. In addition, the ambient air temperatures above and below the slab were also recorded.

After all data were recorded, the heat lamps were turned off, the structure allowed to cool to room temperature, and strain and thermistor readings taken for comparison of cyclic action and instrumentation drift.

V. THERMAL STRESSES

Analysis of thermal strains and stresses in an indeterminate structure is achieved by a) removing redundants to obtain a determinate structure, b) dividing the simple determinate structure into a number of constant-section segments and determining the thermally induced segment strains and stresses, c) applying the redundants as loads and obtaining by conventional methods of analysis the resultant induced stresses and strains caused by the redundants, and d) superimposing the thermally induced and the redundantly induced strains and stresses.

A procedure for determining thermally induced strains and stresses was developed by Zuk[39, 40] and modified by Berwanger[5] and Berwanger and Symko[6]. Emanuel and Hulsey[17] and Hulsey[22] refined the work of Zuk and of Berwanger and developed a procedure to account for slab-beam interaction. The procedure used in this study follows that of Emanuel and Hulsey[17]. The geometric and material segment properties are assumed to be constant along the segment length; the temperature profile through the depth of the cross section is assumed to be constant along the segment length; and the slab and stringer are assumed to form a composite section. The slab may be assumed to be in a) plane stress ($\sigma_z = 0$), b) plane strain ($\varepsilon_z = 0$), or c) in some state between the two. The beam is assumed to be in a state of plane stress. Two types of analysis are presented, one for the slab acting in plane strain and the other for the slab acting in an elastic partially restrained state.

A. PLANE STRAIN

The slab and beam of the segment are assumed to be initially separated and free to deform individually, in response to the temperature distribution throughout the depth of the segment. Composite action

requires that the stringer and the slab have equal strains and curvature at the interface. To achieve this compatibility, a set of forces, i.e., shears and moments, as shown by Aleck[1], Zuk[39, 40], and Emanuel and Hulsey[17], is applied to the separated components. The resulting stresses, strains, curvature, and deflections for the composite segment can be ascertained once the interface forces required for compatibility have been determined.

In the derivation of the expressions for thermal stresses, the following have been assumed: 1) Hooke's law applies; 2) plane sections before bending remain plane after bending; 3) the temperature distribution through the slab and beam may be any continuous function through the depth; 4) the temperature distribution in the longitudinal and transverse directions is constant; 5) the slab and beam are isotropic, elastic, and homogeneous; 6) no stress or vertical force is applied in the y direction (through the depth); 7) fatigue stresses are negligible; 8) elements or segments are straight, prismatic and have a symmetrical cross section; 9) segment action is composite; and 10) an effective AASHTO slab width is used.

From classical elastic relationships, the expressions for strain in three dimensions are

$$\varepsilon_x = \frac{1}{E}[\sigma_x - \mu(\sigma_y + \sigma_z)] \tag{1a}$$

$$\varepsilon_y = \frac{1}{E}[\sigma_y - \mu(\sigma_x + \sigma_z)] \tag{1b}$$

$$\varepsilon_z = \frac{1}{E}[\sigma_z - \mu(\sigma_x + \sigma_y)] \tag{1c}$$

1. Slab Stresses. As previously noted, this analysis assumes that the slab acts in a state of plane strain. The plane stress analysis is identical except that Poisson's effect is neglected. The coordinate system used for either case is shown in Fig. 31.

First, separate the slab and the stringer and assume that the slab is simply supported at each end. Restrain all edges in both the longitudinal and transverse directions and introduce a temperature variation. As a result of the restraints $\overset{*}{\varepsilon}'_{xs} = \overset{*}{\varepsilon}'_{zs} = \overset{*}{\sigma}'_{ys} = 0$ and from Eqs. 1

$$\overset{*}{\sigma}'_{xs} = \overset{*}{\sigma}'_{zs} = - \frac{\alpha_s E_s T_s(y)}{1 - \mu_s} \tag{2}$$

However, the simply supported, separated slab strains freely in the longitudinaly direction. To achieve the effect of free movement and to satisfy force equilibrium, a longitudinal force, P'_{ts}, and a moment, M'_{ts}, are introduced and superimposed upon the thermally induced force and moment resulting from the initially restrained condition. The relationships among these forces and the separated components of the segment are shown in Fig. 32.

Summing forces in the x direction gives

$$P'_{ts} = \frac{\alpha_s E_s b_{ef}}{1 - \mu_s} \int_{-c}^{c} T_s(y)\, dy \tag{3}$$

and summing moments about the z axis yields

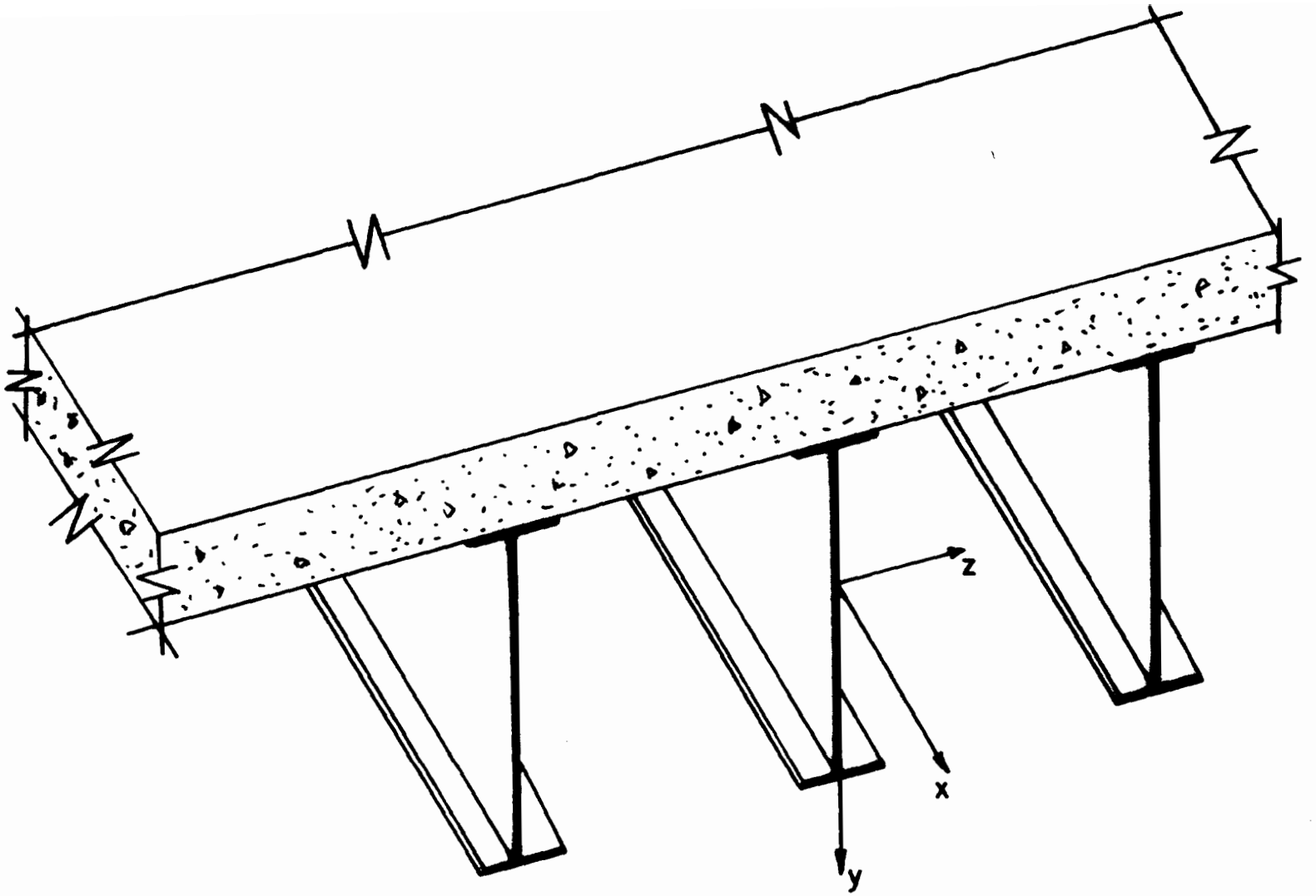

Fig. 31. Thermal Stress Coordinate System

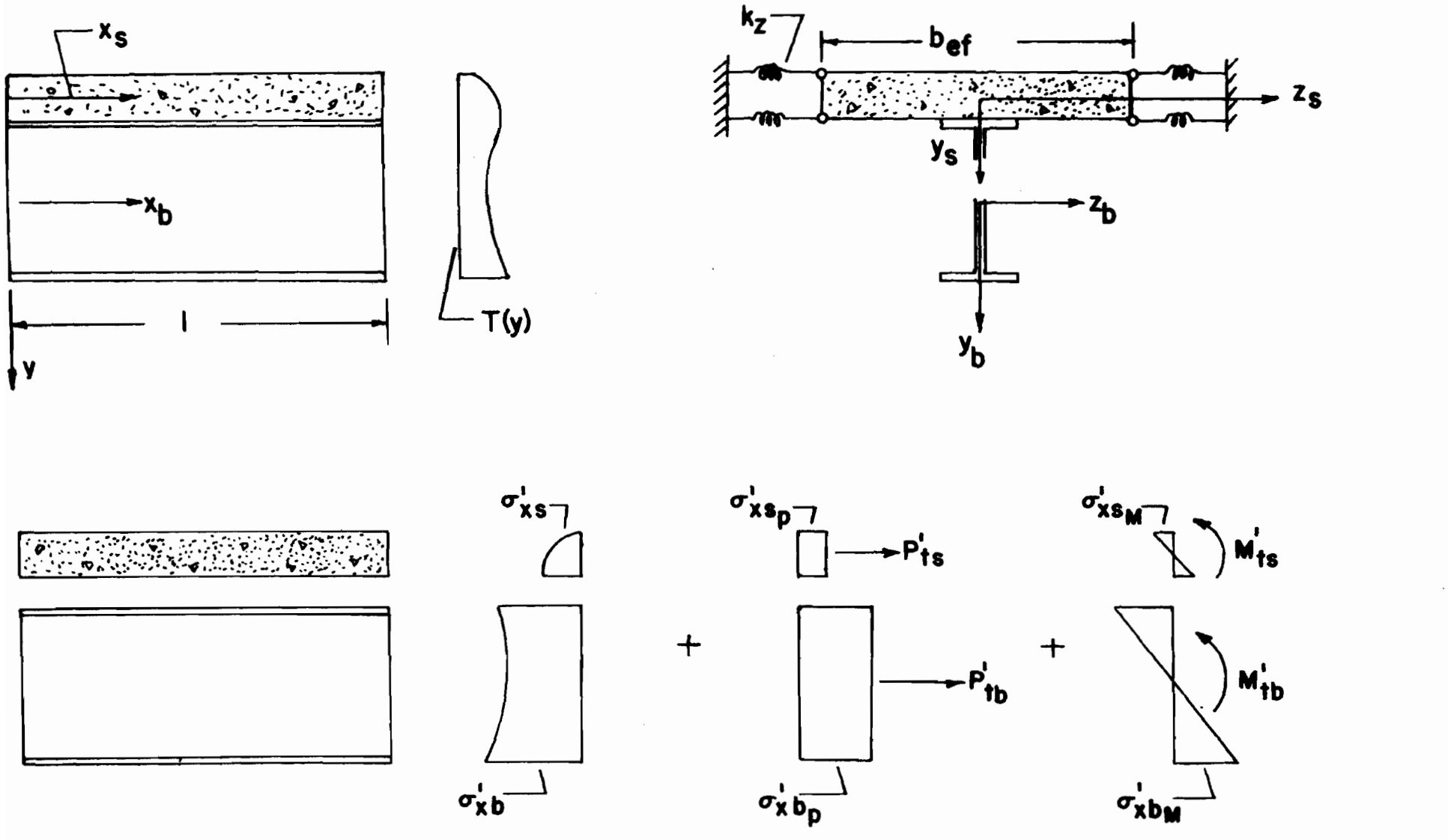

Fig. 32. Slab and Beam Element Forces and Stresses Before Compatibility

$$M'_{ts} = \frac{\alpha_s E_s b_{ef}}{1 - \mu_s} \int_{-c}^{c} T_s(y)\, y\, dy \qquad (4)$$

The resulting slab stresses for the longitudinal unrestrained case then become

$$\sigma'_{xs} = - \frac{\alpha_s E_s T_s(y)}{1 - \mu_s} + \frac{P'_{ts}}{A_s} + \frac{M'_{ts} y_s}{I_s} \qquad (5)$$

and

$$\sigma'_{zs} = - \frac{\alpha_s E_s T_s(y)}{1 - \mu_s} + \mu_s \left[\frac{P'_{ts}}{A_s} + \frac{M'_{ts} y_s}{I_s} \right] \qquad (6)$$

For the case of plane strain in the transverse direction, i.e., $\varepsilon'_{zs} = 0$, the longitudinal strain at the interface of the beam and the web can be found from Eqs. 1 by substituting the respective values of σ.

The longitudinal strain resulting from temperature effects on the freely deforming segment is

$$\varepsilon'_{xs} = \frac{1 - \mu_s^2}{E_s} \left[\frac{P'_{ts}}{A_s} + \frac{M'_{ts} y_s}{I_s} \right] \qquad (7)$$

Because they are dissimilar materials, the separated slab and stringer have different temperature distribution patterns and curvatures. For composite action, these units must deform as a single body. To achieve compatible interface strains and curvature, forces F_1 and F_2 are applied to the slab and beam at the ends of the uniform segment as shown in Fig. 33.

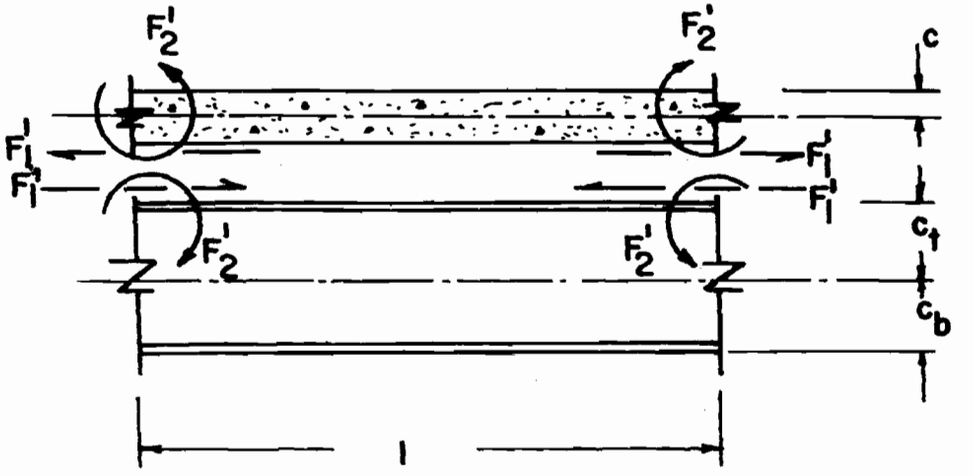

Fig. 33. Compatibility of Forces for a Prismatic Element

Summing forces along the length of the segment $\Sigma F_x = 0$ gives

$$\tau w \, dx = \int_{y}^{y_b} \frac{\partial \sigma}{\partial x} \, dx \, dA \tag{8}$$

If it is assumed that the temperature is a function of depth only, $T = f(y)$, i.e., constant in the longitudinal and transverse directions, the curvature about the transverse axis of the segment must be constant. The constant curvature produces a constant normal stress along the length of the segment resulting in a horizontal shear stress of zero when Eqs. 5 and 8 are solved. By neglecting the local stress concentrations resulting from the application of forces at the ends (St. Venant's principle), the forces occurring at the interface appear as shown in Fig. 33.

From simple mechanics, the longitudinal slab stress produced by the interface forces is

$$\sigma''_{xs} = \left[\frac{1}{A_s} + \frac{c y_s}{I_s} \right] F'_1 - \left\{ \frac{y_s}{I_s} \right\} F'_2 \tag{9}$$

From Eqs. 1 and the relation $\sigma''_{zs} = \mu \sigma''_{xs}$, the transverse slab strain for the case of plane strain, i.e., $\varepsilon''_{zs} = 0$, becomes

$$\varepsilon''_{xs} = \frac{1 - \mu_s^2}{E_s} \sigma''_{xs} \tag{10}$$

Composite action requires that the interface slab and beam strain be equal at any point along the length of the segment. The slab strains

and, similarly, the stresses can be determined by summing the strain resulting from unrestrained movement and the strain resulting from equilibrium and compatibility forces. Thus, after simplification, the slab longitudinal strain and stress become

$$^{c}\varepsilon_{xs} = \varepsilon'_{xs} + \varepsilon''_{xs} \tag{11}$$

and

$$^{c}\sigma_{xs} = \sigma'_{xs} + \sigma''_{xs} \tag{12}$$

From substitution into Eq. 12 and reduction,

$$^{c}\sigma_{xs} = -\frac{\alpha_s E_s T_s(y)}{1-\mu_s} + \frac{P'_{ts}}{A_s} + \frac{M'_{ts} y_s}{I_s} + \left[\frac{1}{A_s} + \frac{cy_s}{I_s}\right] F'_1 - \left\{\frac{y_s}{I_s}\right\} F_2 \tag{13}$$

In the vertical direction,

$$^{c}\sigma_{ys} = \sigma'_{ys} + \sigma''_{ys} = 0 \tag{14}$$

Along the z axis for plane strain,

$$^{c}\varepsilon_{zs} = \varepsilon'_{zs} + \varepsilon''_{zs} = 0 \tag{15}$$

and

$$^{c}\sigma_{zs} = \sigma'_{zs} + \sigma''_{zs} \tag{16}$$

The substitution of the equations for corresponding elements in Eq. 16 and simplification gives

$$c_{\sigma_{zs}} = - \frac{\alpha_s E_s T_s(y)}{1 - \mu_s} + \mu_s \left[\frac{P'_{ts}}{A_s} + \frac{M'_{ts} y_s}{I_s} \right]$$

$$+ \mu_s \left[\left\{ \frac{1}{A_s} + \frac{c y_s}{I_s} \right\} F'_1 - \left\{ \frac{y_s}{I_s} \right\} F_2 \right] \qquad (17)$$

2. Beam Stresses. The analysis for beam strains and stresses is carried out in the same manner as for the slab, namely that the beam and slab are initially separated and assumed simply supported; and temperature effects are then introduced. The temperature distribution through the beam depth is assumed to be constant in the longitudinal and transverse direction. Because the web and flanges are relatively thin, the beam is assumed to act in a state of plane stress.

First, totally restrain the beam in the longitudinal direction (only) and subject it to some temperature variation. From the assumptions and boundary conditions $\overset{*}{\varepsilon}'_{xb} = \overset{*}{\sigma}'_{yb} = \overset{*}{\sigma}'_{zb} = 0$ and using Eqs. 1

$$\overset{*}{\sigma}'_{xb} = - \alpha_b E_b T_b(y) \qquad (18)$$

Add the forces required to provide free movement in the longitudinal direction as shown in Fig. 33 to obtain

$$P'_{tb} = \alpha_b E_b \int_{-c_t}^{c_b} w(y)\, T_b(y)\, dy \qquad (19)$$

and

$$M'_{tb} = \alpha_b E_b \int_{-c_t}^{c_b} w(y)\, T_b(y)\, y\, dy \tag{20}$$

A combination of Eqs. 18, 19, and 20, provides the longitudinal beam stress;

$$\sigma'_{xb} = -\alpha_b E_b T_b(y) + \frac{P'_{tb}}{A_b} + \frac{M'_{tb} y_b}{I_b} \tag{21}$$

The longitudinal beam interface strain for the plane stress state ($\sigma'_{yb} = \sigma'_{zb} = 0$) resulting from temperature variations and free movement conditions becomes

$$\varepsilon'_{xb} = \frac{1}{E_b}\left[\frac{P'_{tb}}{A_b} + \frac{M'_{tb} y_b}{I_b}\right] \tag{22}$$

and the strains perpendicular to the longitudinal axis are

$$\varepsilon'_{yb} = \varepsilon'_{zb} - \frac{\mu_b}{E_b}\left[\frac{P'_{tb}}{A_b} + \frac{M'_{tb} y_b}{I_b}\right] + (1 + \mu_b)\alpha_b T_b(y) \tag{23}$$

To achieve compatibility of slab and beam strain and curvature at the interface, the forces of Fig. 33 applied to the slab must also be applied (in opposite directions) to the beam.

The longitudinal beam stress produced by these forces is

$$\sigma''_{xb} = \left[-\frac{1}{A_b} + \frac{c_t y_b}{I_b}\right] F'_1 + \left\{\frac{y_b}{I_b}\right\} F_2 \tag{24}$$

To satisfy Eqs. 1 for the beam in plane stress,

$$\sigma''_{zb} = \sigma''_{yb} = 0 \tag{25}$$

A combination of Eqs. 20 and 23 produces the longitudinal beam stress,

$$^{c}\sigma_{xb} = -\alpha_b E_b T_b(y) + \frac{P'_{tb}}{A_b} + \frac{M'_{tb} y_b}{I_b} + \left[-\frac{1}{A_b} + \frac{c_t y_b}{I_b} \right] F'_1 + \left\{ \frac{y_b}{I_b} \right\} F'_2 \tag{26}$$

and the vertical and transverse stresses are

$$^{c}\sigma_{yb} = {}^{c}\sigma_{zb} = 0 \tag{27}$$

3. Compatibility of the Composite Section. As previously noted, compatibility requires that the interface slab and beam strains and curvature be equal when the segment is free to deform longitudinally. Expressions can be formulated to determine longitudinal strains and stresses; however, the magnitude of strain and stress in the transverse direction cannot be expressed, because the slab is assumed to be in a state of plane strain and the beam to be in plane stress.

Setting the longitudinal strains equal and introducing the modular ratio ($n = E_b/E_s$) yields

$$\left[\frac{n(1 - \mu_s^2)}{A_s} + \frac{1}{A_b} + \frac{n(1 - \mu_s^2)c^2}{I_s} + \frac{c_t^2}{I_b} \right] F'_1 +$$

$$\left[\frac{c_t}{I_b} - \frac{n(1-\mu_s^2)c}{I_s}\right] F_2' = \left[\frac{P'_{tb}}{A_b} - \frac{M'_{tb}c_b}{I_b}\right] - n(1-\mu_s^2)\left[\frac{P'_{ts}}{A_s} + \frac{M'_{ts}c}{I_s}\right] \tag{28}$$

Expressing the radius of curvature at the interface in terms of the radius of curvature of the slab and of the beam based on radii to their respective centroids gives

$$\rho_{IF} = \rho_s + c = \rho_b - c_t \tag{29}$$

Because both c and c_t are quite small in comparison to the radius of curvature, ρ_{IF}, they can be ignored. The values for curvature can then be found by taking the difference in strain at the slab or beam centroid and at the interface and dividing by the distance between the respective points. Then, for the slab,

$$d\theta_s = \frac{1-\mu_s^2}{E_s}\left[\frac{M'_{ts}}{I_s} + \left\{\frac{c}{I_s}\right\} F_1' - \left\{\frac{1}{I_s}\right\} F_2'\right] dx \tag{30}$$

and for the beam,

$$d\theta_b = \frac{1}{E_b}\left[\frac{M'_{tb}}{I_b} + \left\{\frac{c_t}{I_b}\right\} F_1' + \left\{\frac{1}{I_b}\right\} F_2'\right] dx \tag{31}$$

By Equating Eqs. 30 and 31 and simplifying, one obtains

$$\left[\frac{c_t}{I_b} - \frac{n(1-\mu_s^2)c}{I_s}\right] F_1' + \left[\frac{1}{I_b} + \frac{n(1-\mu_s^2)}{I_s}\right] F_2' =$$

$$n(1 - \mu_s^2) \frac{M'_{ts}}{I_s} - \left\{\frac{1}{I_b}\right\} M'_{tb} \qquad (32)$$

The unknown forces introduced to achieve compatibility, F'_1 and F'_2, can be obtained by solving Eqs. 28 and 32 simultaneously.

B. PLANE STRESS

The derivation and procedure for the case of both the slab and the beam in plane stress are the same as those used for the case of the slab in plane strain and the beam in plane stress, except that the Poisson's ratio effect in the transverse direction is deleted. These two states represent extreme bounds; the actual behavior of the slab is some intermediate stage of partial transverse restraint.

C. PARTIAL TRANSVERSE SLAB RESTRAINT

The following procedure accounts for partial transverse slab restraint by introducing transverse slab curvature and is based on presentations of Emanuel and Hulsey[17] and Hulsey[22]. The procedure parallels the above derivation with the additional assumptions: 1) the temperature at any point in the beam flange varies only in the vertical direction, i.e., the temperature is constant in any horizontal plane along the x and z axes; 2) the longitudinal curvature compatibility ($d\theta_s/dx$), i.e., torsional forces between separated slab sections, is neglected; and 3) the slab segment between beam flanges rotates about the longitudinal axis but does not displace in the transverse direction when subjected to temperature variation.

Initially the slab and the beam are uncoupled as in the previous derivation, and the top beam flange is also uncoupled from the top of the web in order to account for compatibility in the transverse direction. The component members of the composite segment and the

subsequent compatibility forces that will be introduced are shown in Fig. 34. Expressions are developed for strains and stresses for each separate component and combined to obtain values for the composite segment.

1. Slab Stresses Over Slab Width b_f. Consider the slab immediately above the beam flange to be totally restrained in both the longitudinal and transverse directions. Then when subjected to some temperature variation, which is a function of depth only, $\overset{*}{\varepsilon}'_{xs} = \overset{*}{\varepsilon}'_{zs} = 0$ and Eqs. 1 yield

$$\overset{*}{\sigma}'_{xs} = \overset{*}{\sigma}'_{zx} = - \frac{\alpha_s E_s T_s(y)}{1 - \mu_s} \tag{33}$$

Being uncoupled, the slab acts as a simple beam in the longitudinal direction, i.e., along its length. To achieve this free movement and to satisfy equilibrium, force P'_{ts} and M'_{ts} are introduced. By superimposing these forces on the thermal forces induced in the restrained slab and summing, one obtains

$$P'_{ts} = \frac{\alpha_s E_s b_f}{1 - \mu_s} \int_{-c}^{c} T_s(y)\, dy \tag{34}$$

and

$$M'_{ts} = \frac{\alpha_s E_s b_f}{1 - \mu_s} \int_{-c}^{c} T_s(y)\, y\, dy \tag{35}$$

Note that for $b_f = b_{ef}$ these expressions are identical to the ones

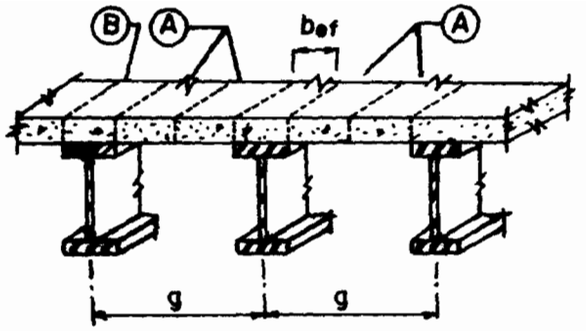

a) Composite - Girder Bridge Superstructure

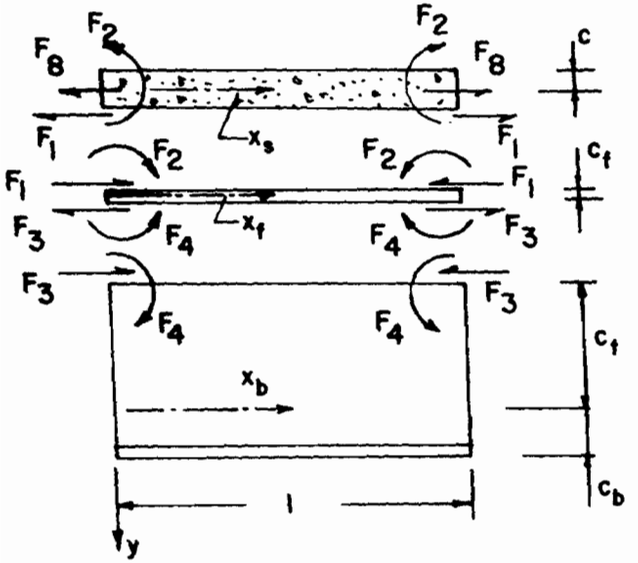

b) Longitudinal Compatibility Forces

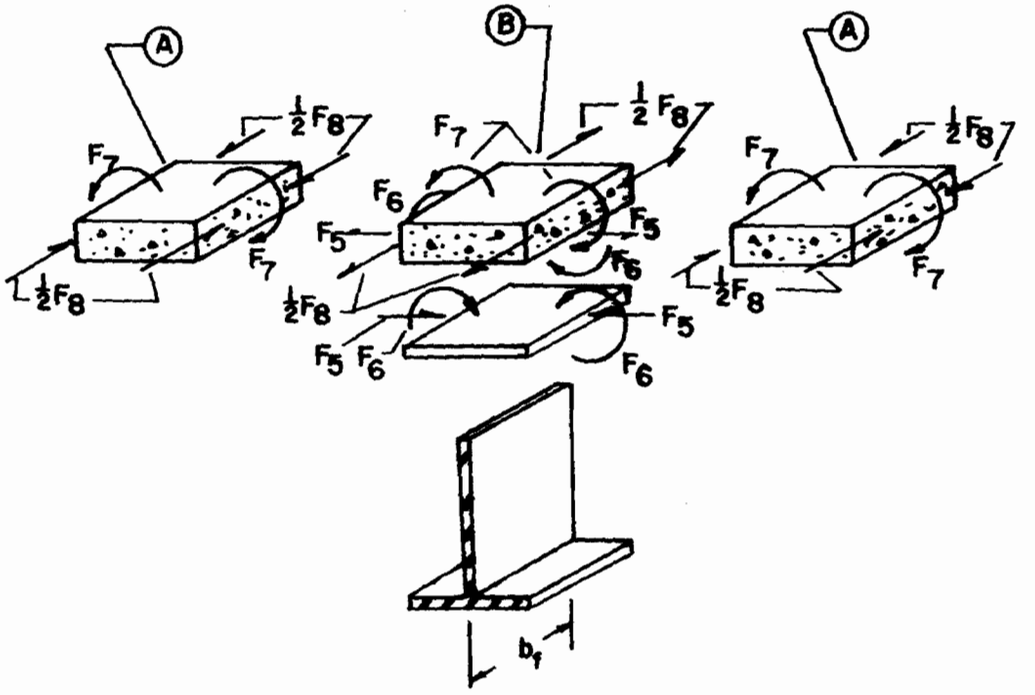

c) Transverse Compatibility Forces, Except for F_8 Longitudinal Forces Are Left Off for Clarity

Fig. 34. Element Compatibility Forces for Partial Transverse Slab Restraint

presented for the slab in a state of plane strain.

The substitution of Eqs. 34 and 35 into Eqs. 1 yields

$$\sigma'_{xs} = \sigma'_{zs} = - \frac{\alpha_s E_s T_s(y)}{1 - \mu_s} + \frac{P'_{ts}}{A_s} + \frac{M'_{ts} y_s}{I_s} \tag{36}$$

As the slab is not restrained in the vertical direction,

$$\sigma'_{ys} = 0 \tag{37}$$

To obtain interface strain and curvature compatibility in the composite segment, unknown forces are introduced and applied to the segment components as shown in Fig. 34. Within the bounds of the following additional assumptions: 1) temperature gradients occur only in the vertical direction, 2) curvature of a prismatic element is constant in the longitudinal and transverse directions, 3) normal stresses, σ_x and σ_z, are constant along the length of the segment, 4) the horizontal interface shear stress is zero, and 5) local stress concentrations produced by application of forces at the ends of the segement can be neglected by virtue of St. Venant's principle, the slab interface forces become

$$\sigma''_{xs} = \left[\frac{1}{A_s} + \frac{c y_s}{I_s} \right] F_1 - \left\{ \frac{y_s}{I_s} \right\} F_2 + \left\{ \frac{1}{A_s} \right\} F_8 \tag{38}$$

and

$$\sigma''_{zs} = \left[\frac{1}{A_s} + \frac{c y_s}{I_s} \right] F_5 - \left\{ \frac{y_s}{I_s} \right\} F_6 - \left\{ \frac{y_s}{I_s} \right\} F_7 \tag{39}$$

Through the summation of the contributory expressions, the stress at any vertical point in the slab above the beam flange becomes

$$\sigma_{xs} = - \frac{\alpha_s E_s T_s(y)}{1 - \mu_s} + \frac{P'_{ts}}{A_s} + \frac{M'_{ts} y_s}{I_s} + \left[\frac{1}{A_s} + \frac{c y_s}{I_s} \right] F_1$$

$$- \left\{ \frac{y_s}{I_s} \right\} F_2 + \left\{ \frac{1}{A_s} \right\} F_8 \qquad (40)$$

$$\sigma_{zs} = - \frac{\alpha_s E_s T_s(y)}{1 - \mu_s} + \frac{P'_{ts}}{A_s} + \frac{M'_{ts} y_s}{I_s} + \left[\frac{1}{A_s} + \frac{c y_s}{I_s} \right] F_5$$

$$- \left\{ \frac{y_s}{I_s} \right\} F_6 - \left\{ \frac{y_s}{I_s} \right\} F_7 \qquad (41)$$

and

$$\sigma_{ys} = 0 \qquad (42)$$

2. Beam Stresses--Top Flange. Based on the assumption of composite action, the biaxial stress state in the bridge slab above the beam flange forces the top flange also to be in a state of biaxial stress as shown in Fig. 34. These biaxial states are caused by dissimilar materials undergoing different temperature variations. Compatibility is achieved by introducing interface forces similar to those previously shown for the plane strain analysis. On the assumption that no transverse forces are created between the web and its flanges (as a result of the thinness of the web), there are no transverse interface forces between the top of the web and the top of

the flange. This assumption also allows the web and the bottom flange to be treated as a single component in a state of plane stress.

By restraining the top flange in the longitudinal and transverse directions and assuming a vertical temperature variation only (along the depth of flange), one can derive from $\overset{*}{\varepsilon}'_{xf} = \overset{*}{\varepsilon}'_{zf} = \overset{*}{\sigma}'_{yf} = 0$ and from Eqs. 1 the following:

$$\overset{*}{\sigma}'_{xf} = \overset{*}{\sigma}'_{zf} = - \frac{\alpha_f E_f T_f(y)}{1 - \mu_f} \tag{43}$$

The introduction of an axial force P'_{tf} and a moment M'_{tf} to allow free movement yields

$$P'_{tf} = \frac{\alpha_f E_f b_f}{1 - \mu_f} \int_{-c_f}^{c_f} T_f(y)\, d_y \tag{44}$$

and

$$M'_{tf} = \frac{\alpha_f E_f b_f}{1 - \mu_f} \int_{-c_f}^{c_f} T_f(y)\, y\, d_y \tag{45}$$

The superimposition of these forces on the thermal forces induced in the restrained flange yields

$$\sigma'_{xf} = \sigma'_{zf} = - \frac{\alpha_f E_f T_f(y)}{1 - \mu_f} + \frac{P'_{tf}}{A_f} + \frac{M'_{tf} y_f}{I_f} \tag{46}$$

For a biaxial stress state in the top flange, the stresses resulting from the unknown interface forces of Fig. 34 become

$$\sigma''_{xf} = \left[- \frac{1}{A_f} + \frac{c_f y_f}{I_f} \right] F_1 + \left\{ \frac{y_f}{I_f} \right\} F_2 + \left[\frac{1}{A_f} + \frac{c_f y_f}{I_f} \right] F_3 - \left\{ \frac{y_f}{I_f} \right\} F_4 \tag{47}$$

$$\sigma''_{zf} = \left[- \frac{1}{A_f} + \frac{c_f y_f}{I_f} \right] F_5 + \left\{ \frac{y_f}{I_f} \right\} F_6 \tag{48}$$

and

$$\sigma''_{yf} = 0 \tag{49}$$

From a summation of the stresses resulting from the interface forces and from thermal loading, the stresses at any vertical point in the flange can be given by

$$\sigma_{xf} = - \frac{\alpha_f E_f T_f(y)}{1 - \mu_f} + \frac{P'_{tf}}{A_f} + \frac{M'_{tf} y_f}{I_f} + \left[- \frac{1}{A_f} + \frac{c_f y_f}{I_f} \right] F_1 + \left\{ \frac{y_f}{I_f} \right\} F_2 + \left[\frac{1}{A_f} + \frac{c_f y_f}{I_f} \right] F_3 - \left\{ \frac{y_f}{I_f} \right\} F_4 \tag{50}$$

$$\sigma_{zf} = - \frac{\alpha_f E_f T_f(y)}{1 - \mu_f} + \frac{P'_{tf}}{A_f} + \frac{M'_{tf} y_f}{I_f} + \left\{ - \frac{1}{A_f} + \frac{c_f y_f}{I_f} \right\} F_5$$

$$+ \left\{\frac{y_f}{I_f}\right\} F_6 \tag{51}$$

and

$$\sigma_{yf} = 0 \tag{52}$$

3. Beam Stresses--Web and Lower Flange. The development for stresses in the web and lower flange is identical to that for the top flange except that only longitudinal compatibility forces are introduced (Fig. 34).

The stresses resulting from the interface forces are

$$\sigma''_{xb} = \left[- \frac{1}{A_b} + \frac{c_t y_b}{I_b} \right] F_3 + \left\{\frac{y_b}{I_b}\right\} F_4 \tag{53}$$

Upon summing Equations 21 and 53, the thermally induced stresses in the web and lower flange of an unrestrained segment become

$$\sigma_{xb} = - \alpha_b E_b T_b(y) + \frac{P'_{tb}}{A_b} + \frac{M'_{tb} y_b}{I_b} + \left[- \frac{1}{A_b} + \frac{c_t y_b}{I_b} \right] F_3$$

$$+ \left\{\frac{y_b}{I_b}\right\} F_4 \tag{54}$$

and

$$\sigma_{yb} = \sigma_{zb} = 0 \tag{55}$$

4. Stresses for Slab Section Between Beam Flanges. The development for stresses in the slab section between beam flanges is identical to that for the slab section immediately above the top flange of the beam except for subscripts. From Eqs. 1 the stresses induced by a thermal variation in a section between the beams and restrained in both the longitudinal and transverse directions ($\varepsilon^{*\prime}_{xsL} = \varepsilon^{*\prime}_{zsL} = \sigma^{*\prime}_{ysL} = 0$) are

$$\sigma^{*\prime}_{xsL} = \sigma^{*\prime}_{zsL} = - \frac{\alpha_s E_s T_{sL}(y)}{1 - \mu_s} \tag{56}$$

The force and moment to produce free movement are

$$P'_{tsL} = \frac{\alpha_s E_s b_f}{1 - \mu_s} \int_{-c}^{c} T_{sL}(y)\, d_y \tag{57}$$

$$M'_{tsL} = \frac{\alpha_s E_s b_f}{1 - \mu_s} \int_{-c}^{c} T_{sL}(y)\, y\, dy \tag{58}$$

The interface forces required for compatibility induce

$$\sigma'_{xsL} = \left\{ - \frac{1}{A_{sL}} \right\} F_8 \tag{59}$$

and

$$\sigma'_{zsL} = \left\{ - \frac{y_s}{I_{sL}} \right\} F_7 \tag{60}$$

The thermal stresses which result at any point within the unrestrained slab section between girders are obtained by summing the contributory terms;

$$\sigma_{xsL} = - \frac{\alpha_s E_s T_{sL}(y)}{1 - \mu_{sL}} + \frac{P'_{tsL}}{A_{sL}} + \frac{M'_{tsL} y_{sL}}{I_{sL}} - \left\{\frac{1}{A_{sL}}\right\} F_8 \qquad (61)$$

$$\sigma_{zsL} = - \frac{\alpha_s E_s T_{sL}(y)}{1 - \mu_s} + \frac{P'_{tsL}}{A_{sL}} + \frac{M'_{tsL} y_{sL}}{I_{sL}} - \left\{\frac{y_{sL}}{I_{sL}}\right\} F_7 \qquad (62)$$

and

$$\sigma_{ysL} = 0 \qquad (63)$$

5. Composite Section. On the assumption that the shear connectors bonding the slab and beam are adequately designed and installed, composite action of the determinate segment is assured, because the flange and web are also rigidly connected. Compatibility of strains and curvature at all interface surfaces is accomplished by action of the interface forces on the segment components as shown in Fig. 34. Interface strains are obtained by substituting Eqs. 40, 41, 42, 50, 51, 52, 54, 55, 61, 62, and 63 for corresponding elements in Eqs. 1. Curvatures can be obtained by dividing the difference in strain at two points at a section by the vertical distance between the points. At the top of a separated segment component,

$$\frac{1}{\rho} = \frac{d\theta}{d\xi} = (\varepsilon_t - \varepsilon_0)/(\xi_t - \xi_0) \qquad (64)$$

and at the bottom of a separated segment component,

$$\frac{1}{\rho} = \frac{d\theta}{d\xi} = (\varepsilon_b - \varepsilon_0)/(\xi_b - \xi_0) \tag{65}$$

With the introduction of the modular ratio $n = E_b/E_s = E_f/E_s$, seven of the eight required simultaneous equations can be obtained by equating strains and curvatures at the interface.

The eighth equation is generated by equating the transverse interface slopes, θ_z, of the segment slab components. The transverse slope at the face of the slab component immediately above the beam flange can be expressed as

$$\int_0^{b_f/2} \frac{1}{\rho}\, dz \tag{66}$$

and the transverse slope at the face of the slab component between the stringers, $g_s = g - b_f$, is given by

$$\int_0^{g_s/2} \frac{1}{\rho}\, dz \tag{67}$$

When expressed for simplicity in matrix form, the eight simultaneous equations become

$$[A]\{F\} = \{B\} \tag{68}$$

in which [A] =

$$\begin{bmatrix}
\lambda & \beta & \lambda_f & -\beta_f & \bar{\lambda} & -\bar{\beta} & \mu_s\beta_s & \tilde{A} \\
 & \psi & \beta_f & -\psi_f & -\bar{\beta} & \bar{\psi} & \beta_s\psi_s & 0 \\
 & & \tilde{\lambda} & \tilde{\beta} & -\mu_f\lambda_f & -\mu_f\beta_f & 0 & 0 \\
 & & & \tilde{\psi} & \mu_f\beta_f & \mu_f\psi_f & 0 & 0 \\
 & & & & \lambda & \beta & -\beta_s & -\mu_s\tilde{A} \\
 & & & & & \psi & \psi_s & 0 \\
 & & & & & & \approx & \\
 & & & & & & \psi & 0 \\
 & & & & & & & \approx \\
 & & & & & & & \tilde{A}
\end{bmatrix}$$

and

$$\lambda = n\left[\frac{1}{A_s} + \frac{c^2}{I_s}\right] + \left[\frac{1}{A_f} + \frac{c_f^2}{I_f}\right]$$

$$\lambda_f = \left[-\frac{1}{A_f} + \frac{c_f^2}{I_f}\right]$$

$$\tilde{\lambda} = \left[\frac{1}{A_f} + \frac{c_f^2}{I_f}\right] + \left[\frac{1}{A_b} + \frac{c_b^2}{I_b}\right]$$

$$\lambda = -n\mu_s\left[\frac{1}{A_s} + \frac{c^2}{I_s}\right] - \mu_f\left[\frac{1}{A_f} + \frac{c_f^2}{I_f}\right]$$

$$\beta_s = n[c/I_s]$$

$$\beta_f = c_f/I_f$$

$$\beta = -\beta_s + \beta_f$$

$$\bar{\beta} = -\mu_s\beta_s + \mu_f\beta_f$$

$$\tilde{\beta} = -\beta_f + c_b/I_b$$

$$\psi_f = 1/I_f$$

$$\psi_s = n[1/I_s]$$

$$\psi = \psi_s + \psi_f$$

$$\bar{\psi} = -\mu_s\psi_s - \mu_f\psi_f$$

$$\tilde{\psi} = \psi_f + 1/I_b$$

$$\tilde{\tilde{\psi}} = \psi_s + n[g_s/b_f I_s]$$

$$\tilde{A} = n[1/A_s]$$

$$\tilde{\tilde{A}} = \tilde{A} + n[1/A_{sL}]$$

and [B] =

$$
\begin{Bmatrix}
-n[1-\mu_s][P'_{ts}/A_s + M'_{ts}c/I_s] + [1-\mu_f][P'_{tf}/A_f - M'_{tf}c_f/I_f] \\
n[1-\mu_s]M'_{ts}/I_s - [1-\mu_f]M'_{tf}/I_f \\
-[1-\mu_f][P'_{tf}/A_f + M'_{tf}c_f/I_f] + [P'_{tb}/A_b - M'_{tb}c_b/I_b] \\
[1-\mu_f]M'_{tf}/I_f - M'_{tb}/I_b \\
-n[1-\mu_s][P'_{ts}/A_s + M'_{ts}c/I_s] + [1-\mu_f][P'_{tf}/A_f - M'_{tf}c_f/I_f] \\
n[1-\mu_s]M'_{ts}/I_s - [1-\mu_f]M'_{tf}/I_f \\
n[1-\mu_s]M'_{ts}/I_s + n[M'_{tsL}g_s/b_fI_s] \\
n[1-\mu_s][P'_{tsL}/A_{sL} - P'_{ts}/A_s]
\end{Bmatrix}
$$

The interface forces are obtained by rearranging Eq. 66 to the form

$$\{F\} = [A]^{-1}\{B\} \tag{69}$$

The thermal stresses described above are for any given element, e, in a structure. The stress values depicted by Eqs. 40, 41, 42, 50, 51, 52, 54, and 55 are referred to as compatibility stresses with the rigid boundaries at the modes of each element removed. (Rigid boundaries are taken into account later in the formulation of element stiffness matrices in the stiffness method of indeterminate analysis.) These stresses then represent the thermal stresses induced in a determinate (simply supported) prismatic element of length, ℓ, meeting the assumptions of the derivation.

D. FINAL STRESSES, FORCES, AND DEFORMATIONS

Stresses resulting from applied loads and the indeterminacy of the structure are obtained by using the stiffness method of indeterminate analysis. This method gives the forces (thrust, shear, and moment) that act at the nodal ends of each element. These forces are added directly to the fixed-end forces caused by thermal loading (shown in Fig. 35). These forces are typical for each element analyzed. Temperature variation introduces fixed-end forces that can be added directly to forces obtained from indeterminate analysis at each node to determine stresses in these elements.

Final stresses, strains, and deflections at any point in the structure can then be found by superimposing the values obtained from the stiffness method, the fixed-end force values, and the thermal values of compatibility curvature and differential expansion stresses, strains, and deflections as previously derived.

The thermal loading fixed-end forces for the plane strain case are

$$\{F_o\} = \begin{Bmatrix} P'_{ts} + P'_{tb} \\ 0 \\ -E_b I_c (d\theta_b/dx) \\ -(P'_{ts} + P'_{tb}) \\ 0 \\ E_b I_c (d\theta_b/dx) \end{Bmatrix} \qquad (70)$$

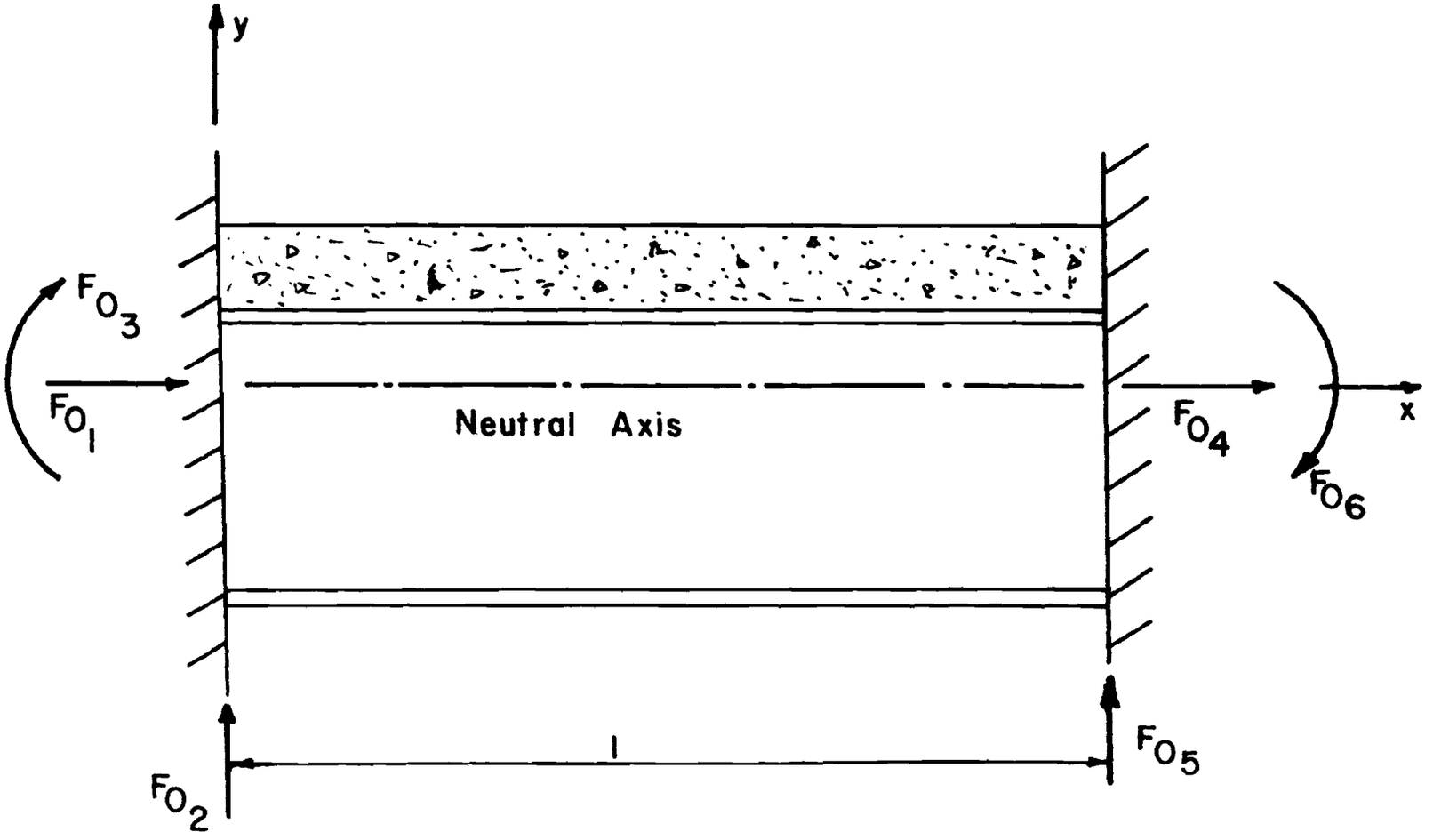

Fig. 35. Fixed - End Forces of a Prismatic Element

wherein

$$\frac{d\theta_b}{dx} = (1 - \mu)\frac{M'_{tb}}{E_b I_b} + F'_1\left\{\frac{c}{I_b E_b}\right\} + F'_2\left\{\frac{1}{I_b E_b}\right\} \tag{71}$$

For the partially restrained (elastic bending) case,

$$\{F_o\} = \begin{Bmatrix} P'_{ts} + P'_{tf} + P'_{tb} + \left\{\frac{b_{ef} - b_f}{b_f}\right\} P'_{tsL} \\ 0 \\ -E_b I_c\,(d\theta_{sx}/dx) \\ -\left[P'_{ts} + P'_{tf} + P'_{tb} + \left\{\frac{b_{ef} - b_f}{b_f}\right\} P'_{tsL}\right] \\ 0 \\ E_b I_c (d\theta_{sx}/dx) \end{Bmatrix} \tag{72}$$

in which

$$\frac{d\theta_{sx}}{dx} = (1 - \mu_s)\frac{M'_{ts}}{E_s I_s} + (F_1 - \mu_s F_s)\frac{c}{E_s I_s}$$

$$- (F_2 - \mu_s F_6)\frac{1}{E_s I_s} + (\mu_s F_7)\frac{1}{E_s I_s} \tag{73}$$

The stiffness procedure used for determining forces other than thermal forces is generally known and may be briefly outlined as follows: 1) the bridge structure is divided into prismatic elements; 2) rigid boundaries are introduced at each nodal point; 3) fixed-end

forces are obtained for unit deformations and combined to formulate individual element stiffness matrices; 4) the structural stiffness matrix is assembled from the element matrices; and 5) the resultant system of forces related to the structure stiffness and the nodal deformations is solved to obtain the unknown forces and moments acting on each node of each element. These forces and moments can be added to the thermally induced fixed-end forces, and the thrust, shear, and moment relations at intermediate points along the length of each element can be obtained by numerical procedures, such as one developed by Newmark[31]. Stress values at any point can then be obtained from any of the classical relationships involving force, moment, and section and material properties. These stresses are then superimposed onto the thermally induced stresses arising from compatibility to give the final stress level at any point in the structure.

The theoretical stresses and strains presented in this report were obtained by applying the above procedure to experimental temperature profiles obtained from the laboratory tests of this study. Calculated values were obtained by utilizing a computer program developed by Hulsey[22] and available through the Department of Civil Engineering of the University of Missouri-Rolla.

VI. HEAT TRANSFER

The analysis of temperature distribution through a bridge structure has attracted much attention in recent years. Both steady-state and transient conditions have been studied, the latter in an effort to predict structure temperatures caused by the environmental cycle. Solutions for temperature distribution center on numerical techniques, either finite element of finite difference, because the complexity of the governing differential equations makes a closed form solution quite tedious, if not nearly impossible. This complexity arises from the geometry of the structure, the boundary conditions, and the effects of the three classical forms of heat transfer--namely conduction, convection and radiation.

Only steady-state conditions were considered in this investigation. Excellent discussions of transient conditions are presented by Lanigan[26], Hulsey[22], and Hulsey and Emanuel[23]. Also, only the general formulation of the heat transfer equations are discussed herein, because solutions to both transient and steady state problems are well documented in the above references and also in work by Priestley[32], Emerson[19], and Hunt and Cooke[24].

In this discussion, terms such as solar radiation are used which are applicable to an actual prototype in the field, but not necessarily present in laboratory modelling. The magnitude of these terms are functions of time and geographic location, and they are included in the discussion to help give a better understanding of actual physical conditions. The solar radiation source for steady state laboratory testing was infrared heat lamps set at constant emittance values which

yielded eventual steady state conditions.

As noted, a study of temperature distribution in bridge structures involves the three classical types of heat transfer: 1) conduction of energy through the deck and the beams, 2) radiation gain from the sun, and also radiation loss from the structure itself based on absolute temperatures, and 3) heat loss or gain by convection from the structure to the surrounding air arising from temperature differentials.

For a bridge long enough that the temperature distribution can be assumed constant along the length (i.e., neglecting heat loss through the ends by a principle analogous to St. Venant's principle), the flow of heat through the structure is essentially a two dimensional problem. Fig. 36 shows the coordinate system used in the formulation.

The two dimensional problem (neglecting the z direction) can be shown as

$$\frac{\partial}{\partial x}\left\{k_x(x,y)\ \frac{\partial t}{\partial x}\ (x,y)\right\} + \frac{\partial}{\partial y}\left\{k_y(x,y)\ \frac{\partial t}{\partial y}\ (x,y)\right\} = 0 \qquad (74)$$

which is from the general class of field problems governing torsion, heat conduction, and fluid seepage. In Eq. 74, $t(x,y)$ is the temperature function, x and y are cartesian coordinates, $k_x(x,y)$ and $k_y(x,y)$ are anisotropic thermal conductivities, and $\frac{\partial t}{\partial x}(x,y)$ and $\frac{\partial t}{\partial y}(x,y)$ are temperature gradients in the x and y directions (transverse to the stringers and through the depth, respectively). Assuming the concrete deck to be homogeneous and isotropic and that the reinforcement in the deck may be considered negligible, Eq. 72 can be reduced to a two-dimensional problem similar to that shown by Hunt and Cooke[24]

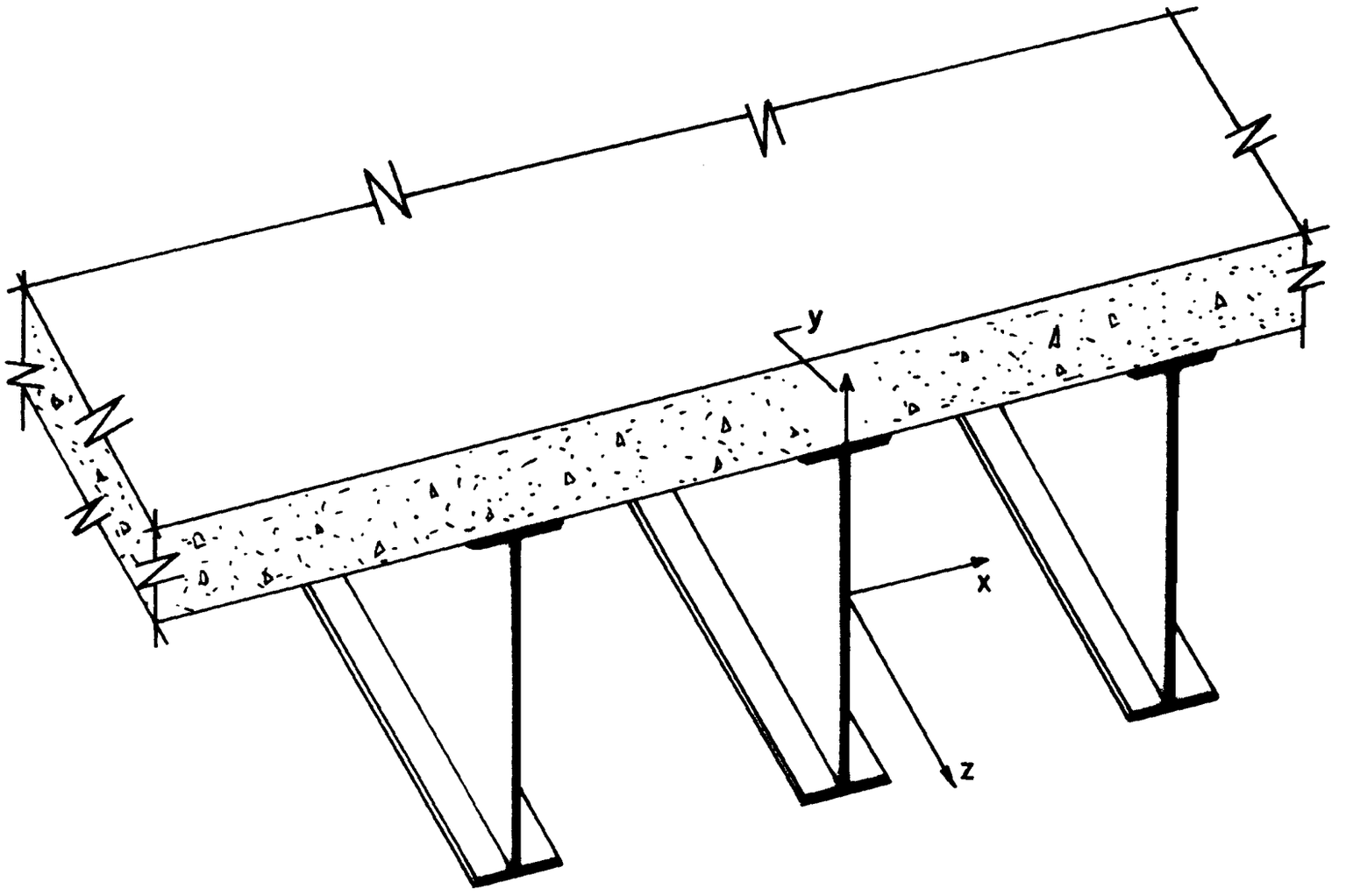

Fig. 36. Heat Transfer Coordinate System

and Hulsey and Emanuel[23] which expresses temperature at any point in the bridge as

$$k_i \left\{ \frac{\partial^2 t}{\partial x^2} + \frac{\partial^2 t}{\partial y^2} \right\} = 0 \qquad i = 1, 2 \ldots n \tag{75}$$

where i refers to the ith material, e.g., slab, web, flange, etc.

Equation 75 describes the heat flow through any given material. When more than one material is present, as in a composite bridge, the temperature and heat flux values must be constant and continuous across the material interface. Thus, for any given interface boundary, the thermal values along the edge of one material are transferred to the edge of the next material, forcing compatibility. This energy transfer is a continous function which follows the same logic as interface strain compatibility.

At the interface of the bridge structure and the surrounding air, energy can be transferred by three means; 1) solar flux absorbed by the bridge deck, noted as q_s; 2) convection, noted as $q_c(x,y)$; and 3) thermal radiation from the structure itself, noted as $q_r(x,y)$. The relationship at any boundary location can be expressed by

$$k_i \frac{\partial t}{\partial x} \ell_x + k_i \frac{\partial t}{\partial y} \ell_y + q_s + q_c(x,y) + q_r(x,y) = 0 \tag{76}$$

where ℓ_x and ℓ_y are direction cosines of the outward normal to the bridge deck. For boundaries not exposed to solar radiation, e.g., the interface of the bottom of the deck and the air, q_s becomes zero.

A closer look at the terms of Eq. 76 shows that the heat gain at the surface of the deck resulting from the sun's rays, i.e., solar or

short wave radiation, can be expressed as

$$q_s = \alpha_r I_n \tag{77}$$

where α_r is the absorption coefficient of the deck, a function of the surface texture of the deck, the deck material, and the angle of incidence of radiation. I_n is the sum of direct and diffuse radiation incident upon the bridge deck in Btu/hr-ft^2(w/m^2). As noted, q_s becomes zero for boundaries not exposed to the sun.

Convective heat transfer is governed by Newton's law of cooling

$$q_c(x,y) = h_c \{t(x,y) - T_a\} \tag{78}$$

in which T_a is the ambient air temperature around the structure and $t(x,y)$ is the temperature at any point on a boundary. The heat transfer film coefficient, h_c, is a function of air velocity across the surface, surface texture and geometric configuration, and orientation of the boundary. The values for the film coefficient can be either determined experimentally or calculated from empirical equations. Expressions for either laminar or turbulent flow can be found in most standard elementary heat transfer texts such as those by Holman[21] and McAdams[28]. The equations for laminar flow are based on either horizontal or vertical plates in a controlled environment. Discretion and judgment must be utilized in applying these equations to a bridge structure because continuous laminar flow is a questionable phenomenon as a result of irregular contours under the deck, and protruding elements such as curbs cause discontinuous flow patterns. Thus, empirical expressions can give only a rough estimate, and coefficient values would need to be calculated from wind tunnel tests since values for

bridges have not been published.

One empirical formula

$$h_c = 1.0 + 0.22\ v \tag{79}$$

has been developed[2] for forced convection in which the air currents are laminar across a flat horizontal plate. The air velocity, v in ft/sec (m/sec), must be below 16 ft/sec (4.9 m/sec). For bridges then, this formula would be exact only for the top surface of the deck. This equation has been used by Lanigan[26] and Hulsey[22], and gives the best general values available.

The heat transfer between the structure and the surrounding atmosphere caused by long wave or thermal radiation is highly nonlinear and can be modelled by

$$q_r(x,y) = \sigma_{sb}\varepsilon_r T_\alpha(x,y)^4 - q_{as} \tag{80}$$

where σ_{sb} is the Stephan-Boltzman constant, $T_\alpha(x,y)$ is the temperature at a point on the boundary in degrees absolute, and ε_r is the emissivity coefficient relating the radiation of the bridge surface (a gray body) to that of an ideal black body. The term q_{as} denotes atmospheric long wave radiation and is well known in two forms which give approximately equal values. The first, found in most texts and used by Lanigan[26] is expressed by

$$q_{as} = \sigma_{sb}\varepsilon_r T_\infty^4 \tag{81}$$

where T_∞ is the ambient air temperature in degrees absolute surrounding the bridge. The second expression has been developed more recently through work of Idso and Jackson[25] and Armaly and Leeper[3] to be

$$q_{as} = \sigma_{sb} \varepsilon_r \varepsilon_{as} T_\infty^4 \tag{82}$$

where ε_{as} is the atmospheric emittance expressed by

$$\varepsilon_{as} = 1 - 0.261 \exp\left[-7.776 \times 10^{-4} (T_c)^2\right] \tag{83}$$

with T_c being the ambient air temperature in degrees Celsius. Equation 82 will yield values slightly lower than those of Eq. 81.

From the above discussion, it may be easily seen that the solution of Eqs. 76 and 77 and thermal compatibility requirements at material interfaces lead to highly complex solutions. As noted earlier, this complexity has led to the development of several numerical solution procedures. Priestley[32] devised a one-dimensional linear solution. Emerson[19] developed a finite difference technique capable of handling one-dimensional heat flow with linear boundary conditions. Hunt and Cooke[20] extended Emerson's work to include non-linear boundary conditions. Two-dimensional solutions based on finite element techniques and capable of handling various boundary conditions have been developed by Lanigan[26], Zienkiewicz and Cheung[37], Zienkiewicz and Parekh[38], and Wilson and Nickell[36] with extensions of the latter by Hulsey[22].

Any of these methods can be used to give reasonable values of the temperature distribution through a cross section. All theoretical predictions in this report are based on the techniques of Wilson and Nickell[36] as extended by Hulsey[22].

VII. RESULTS OF EXPERIMENTAL INVESTIGATION

A. TEMPERATURE DISTRIBUTION

The major objective of the study was to obtain thermally induced strains in a laboratory test bridge structure that was to be subjected to thermal loading in a controlled environment and to then compare these strains with values obtained from theoretical procedures developed by Emanuel and Hulsey[17] and Hulsey[22]. In addition to observing strains, it was desired to obtain the experimental temperature profiles through a cross section and to compare these profiles with theoretical profiles obtained from a numerical approach developed by Wilson and Nickell[36] and most recently extended by Hulsey[22]. The temperature profiles are discussed below.

As described previously, a steady-state condition due to heating was achieved by exposing the bridge deck to infrared radiation from heat lamps for a period of seven to eight hours. In the test sequence, two levels of radiation were used, and the tests were repeated at each level to check reproducibility of results. Multiple runs at each level were selected over singular tests at many different input levels, because it was believed that trends could be better substantiated with consistent readings than with singular readings subject to some degree of doubt as to accuracy.

The higher level of input heat flow was governed by the transformer's capacity, which was 28 amps per circuit. Circuits down the center of the structure, circuits 4 and 5 of Fig. 28b, were set to this level, and then the outer circuits were adjusted with the aid of the heat receptor previously described to obtain uniform flux. For the second series of

tests, transformer settings were reduced by 15 percent and then adjusted to give uniformity of incident flux.

An approximate value of the flux incident upon the deck surface could be determined from the manufacturer's data and the known voltage applied to the lamps through the transformers. Assuming that the output of each lamp covered 144 sq in. (929 sq cm)--the lamps were spaced 12 inches [30 cm] on center in each direction, see Fig. 28a--the incident flux on any given square inch (sq cm) of exposed surface became the wattage emitted by the lamps divided by 144 (929). At the maximum level of output for the tests, the lamps emitted about 79 percent of their rated capacity, which produced an incident heat flux of 1.30 Btu/hr-in.^{2} (0.21 W/cm^2). When the transformer settings were reduced 15 percent, the incident heat flux became 1.13 Btu/hr-in.^{2} (0.18 W/cm^2), 12 percent lower than the higher value. Using an absorbtivity factor of 0.7[22, 26] for the concrete deck (30 percent of radiated energy reflected by the deck back to the atmosphere), the heat flux entering the deck became 0.91 Btu/hr-in.^{2} (0.15 W/cm^2) and 0.79 Btu/hr-in.^{2} (0.13 W/cm^2).

Tests at the higher input value, hereafter referred to as Series One, gave very uniform results. Fig. 37 shows the temperature profiles obtained at the three transducer groups located along the center stringer (locations 2, 3, and 4 of Fig. 15) for Test 1 of Series One. These profiles are typical of the tests run with the higher heat flux value. The maximum temperature difference taken from stable sensors in the three transducer groups was three percent which occurred at the surface of the deck and was common to all tests. All temperature profiles for the tests of Series One fall within a band of

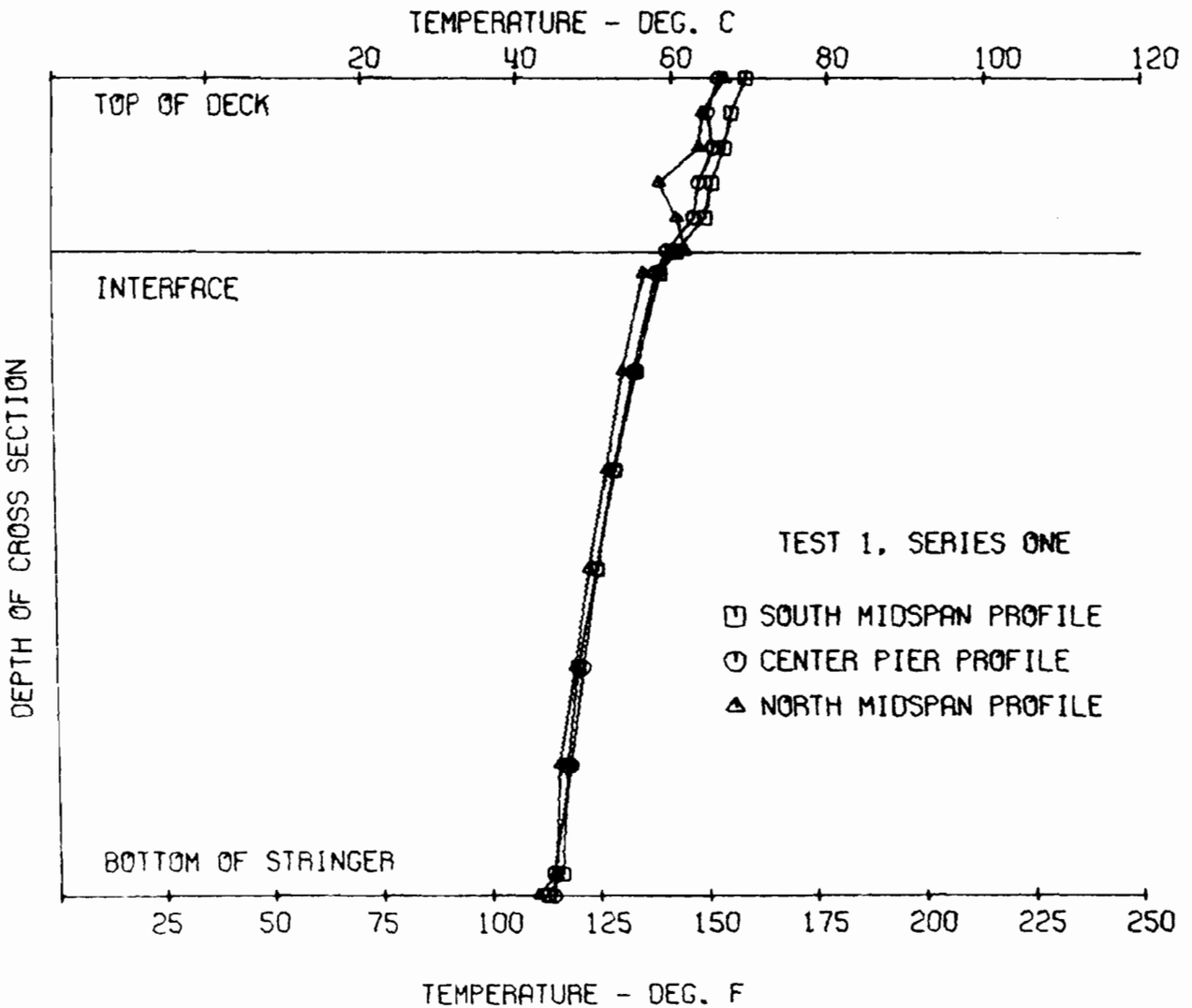

Fig. 37. Temperature Profiles, Test 1, Series One

± two percent of those shown for Test 1. Profiles for two other tests of Series One are shown in Figs. 38 and 39.

For both Series One and Two it should be noted that the temperature values for the north midspan at approximately two-thirds of the depth of the slab and at the deck-beam interface are not true values as the thermistors at these locations became unstable. The other temperature values for all profiles can be considered accurate within the instrumentation limits.

The lowest temperature on a profile, at the bottom of the stringer, is located at the outer edge of the flange, not directly beneath the web. The temperature beneath the web was always very close to that at the location on the web just above the flange. This web value is shown on the profiles immediately above the bottom flange temperature.

The temperatures obtained for tests in Series Two (power reduced 15 percent) parallel those of the Series One tests. Profiles for this series are shown in Figs. 40, 41, and 42.

In observing the profiles of Test 2 of Series Two, it can be seen that the temperatures tend to be about 6 F (3 C) cooler through the depth of the cross section than those of Tests 1 and 3 of Series Two under the same conditions. This resulted from drift of the recorded base value used to calculate the temperature values. Thermistor resistance readings for the three tests shown were very close. If the above temperature differenc (6 F [3 C]) was added to each value of Test 2, the profiles of all three tests would fall into a small band similar to that noted for the Series One tests.

The theoretical temperature profiles were obtained from a finite element analysis of the heat transfer problem. The general solution

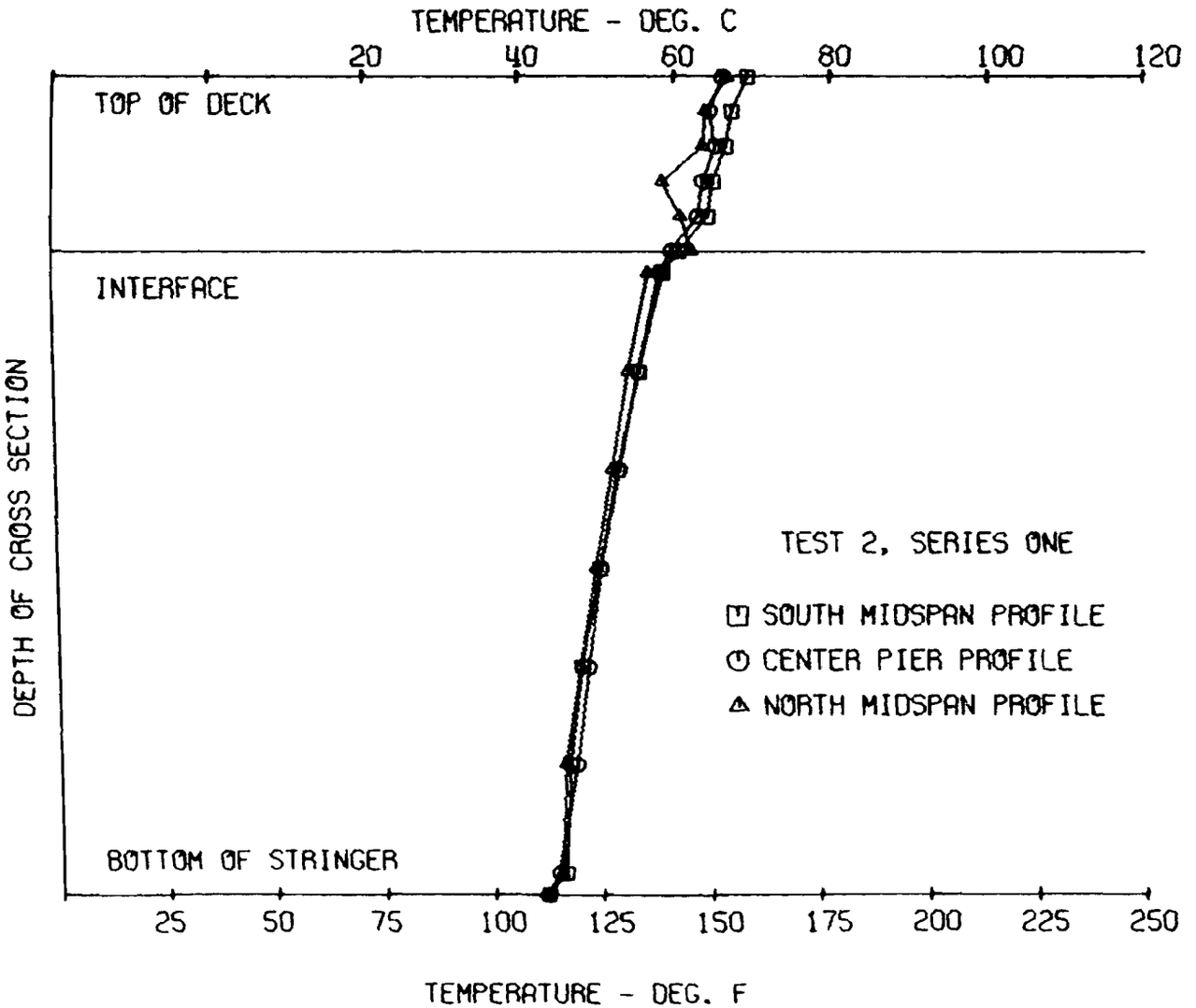

Fig. 38. Temperature Profiles, Test 2, Series One

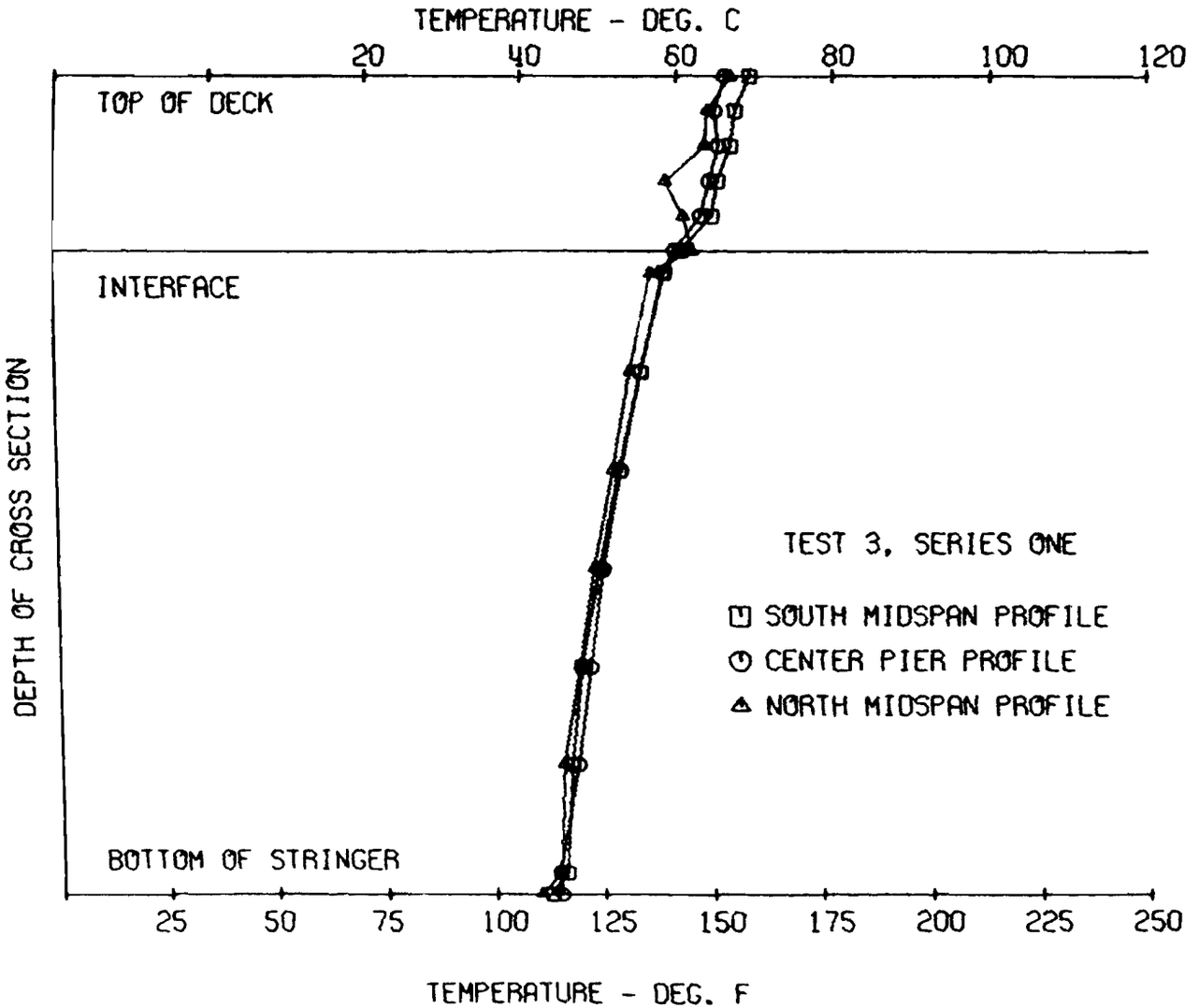

Fig. 39. Temperature Profiles, Test 3, Series One

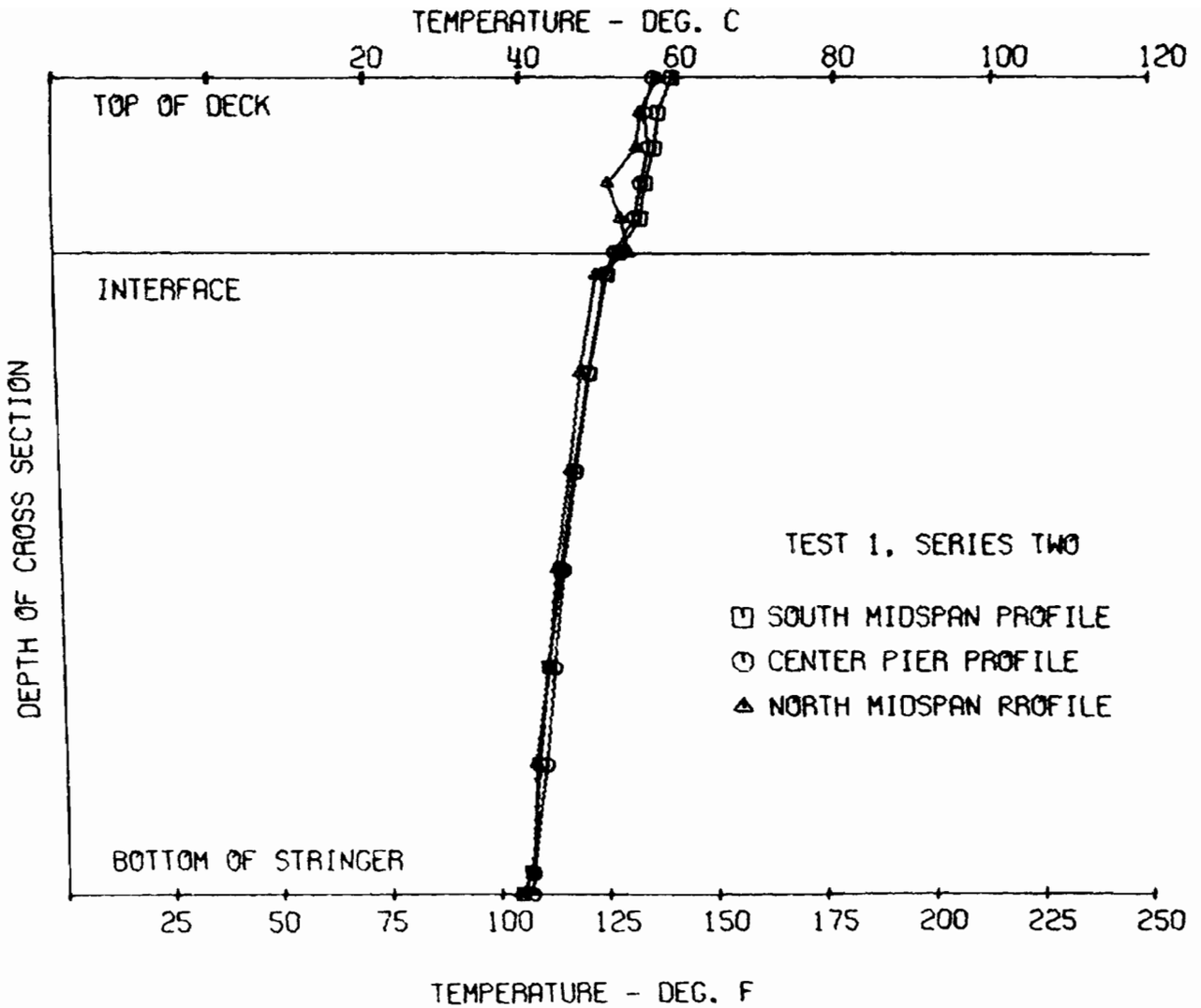

Fig. 40. Temperature Profiles, Test 1, Series Two

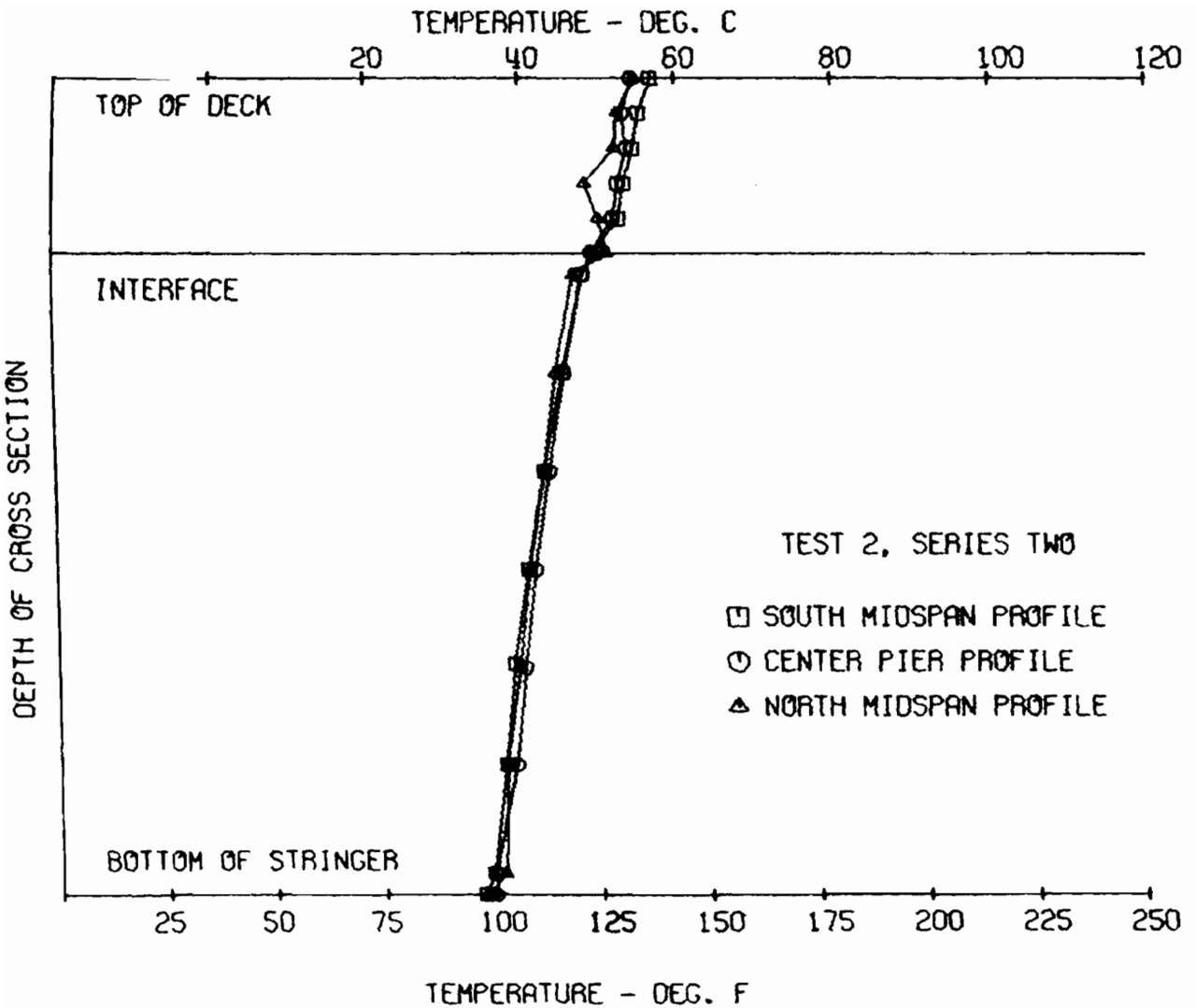

Fig. 41. Temperature Profiles, Test 2, Series Two

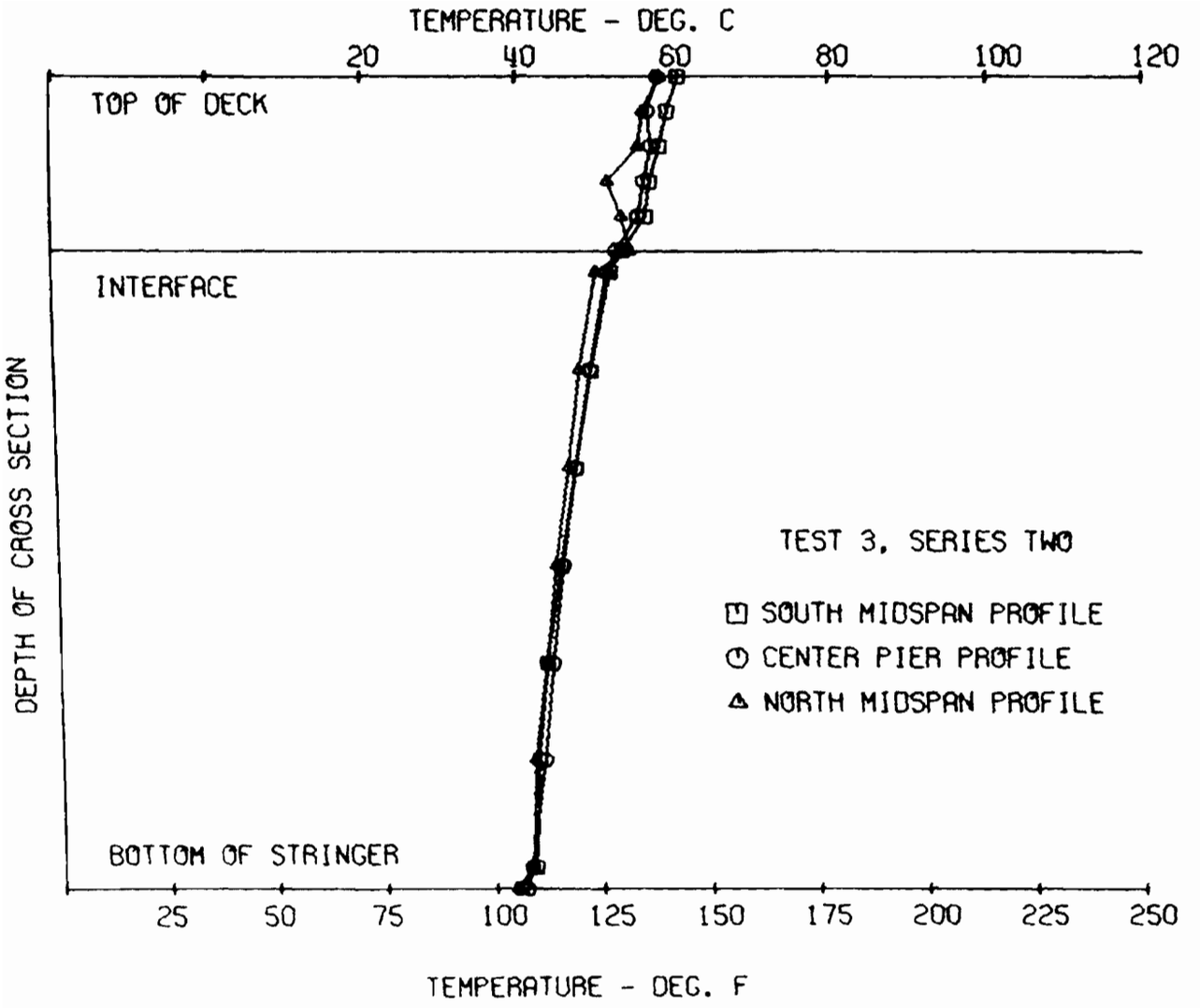

Fig. 42. Temperature Profiles, Test 3, Series Two

procedure, as outlined earlier, was capable of handling a radiant flux as a heat source and higher order nonlinear convection boundary conditions.

To utilize this analysis, an 88-element grid was designed which covered the partial bridge cross section as shown in Fig. 43. The vertical boundaries, as denoted by the centerlines, are considered perfectly insulated, allowing convection to occur only from the top and the bottom of the deck and from the left face of the stringer. No convective losses occur at the centerline, because the cross section in an actual structure is continuous.

The heat flux values put into the finite element program were the magnitudes of flux (assuming an absorbitivity factor of 0.7) absorbed by the deck in the test series, namely 0.91 Btu/hr-in.^{2} (0.15 W/cm^2) and 0.79 Btu/hr-in.^{2} (0.13 W/cm^2). The value used for thermal conductivity, k, of the concrete deck was 0.80 Btu/ft-hr-F (0.014 W/cm-C). This was consistent with values reported by Holman[21] and Lanigan[26]. The value of 31 Btu/hr-ft-F (0.54 W/cm-C) was used for the steel.

Ambient air temperatures were obtained from readings taken in the vicinity of the test structure during thermal testing. The values recorded were 120 F (49 C) above the slab and 95 F (35 C) below the slab for the Series One tests and 110 F (43 C) above and 90 F (32 C) below for the Series Two tests with reduced flux values.

Values for the convective film coefficient were the most difficult to select. The values chosen were based on Eq. 79 for an assumed wind velocity of 1 ft/sec (0.3 m/sec) in the laboratory that resulted from thermal currents discussed previously. This gave a coefficient of 1.22 Btu/hr-ft^2-F (6.93 W/m^2-C). Emerson[19] and Priestley[32]

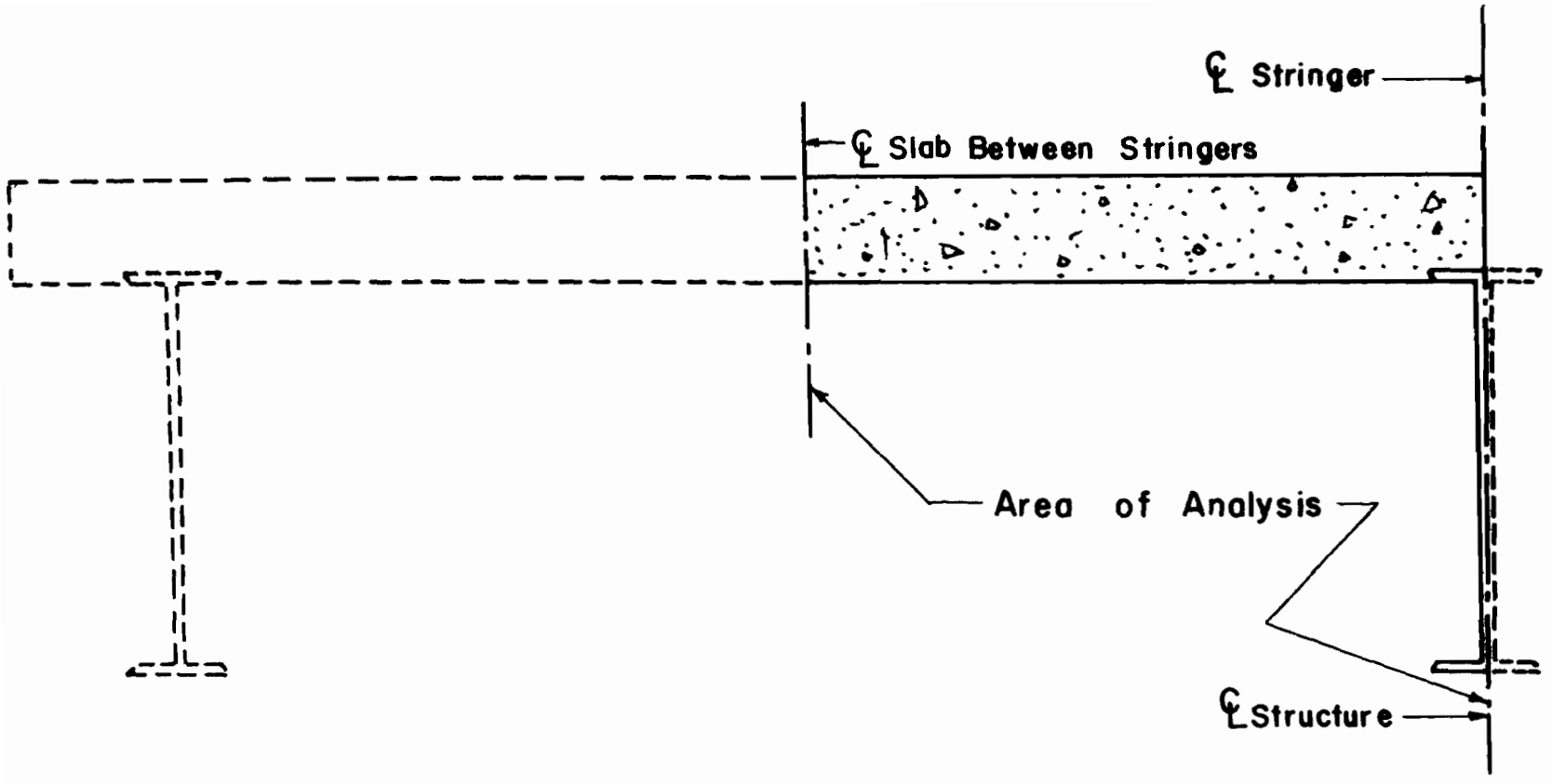

Fig. 43. Partial Bridge Section for Finite Element Analysis

suggested that a coefficient of one-half of that used for the upper surface of the deck be used for the underside of the deck.

The coefficient selected for the exposed portion of the stringer and underside of the deck was determined by an iterative procedure using the higher flux level input and starting with the suggested one-half value for the lower areas and then increasing the ratio in steps (0.50, 0.55, 0.60). The theoretical profile for a ratio of 1 to 0.6 most closely matched the experimental profile. This 1:0.6 relationship (1.22 Btu/hr-ft^2-F [6.93 W/m^2-C] to 0.74 Btu/hr-ft^2-F [4.16 W/m^2-C]) was then used with the reduced flux level, and a very close match of the theoretical and experimental profiles was again obtained.

The one-half reduced rate suggested by Emerson[19] and Priestley[32] in their studies of concrete box girder bridges was for horizontal surfaces of the structure facing downward that were continuous across the width of the structure. The difference encountered in composite design bridges stems from the fact that the area of primary concern with regard to heat loss is not a continuous horizontal plane. The web of the stringer constitutes a vertical plane of high heat loss having a horizontal cover that gives a partially enclosed area. This vertical plane loses heat faster than a horizontal plane facing downward and leads to a slightly higher value than that suggested. However for natural convection, a reduced coefficient is justified for the region below the deck, because the deck tends to alter the heat flow pattern from the stringer, e.g., hot air rises while cool air falls.

The numerical values used to obtain the theoretical temperature profiles are tabulated in Table 1.

TABLE I

NUMERICAL VALUES USED FOR CALCULATION OF THEORETICAL TEMPERATURE PROFILES

	Trial 1		Trial 2	
Property	English	Standard	English	Standard
Heat Flux	1.30 $\frac{Btu}{hr\text{-}in.^2}$	0.212 $\frac{W}{cm^2}$	1.13 $\frac{Btu}{hr\text{-}in.^2}$	0.185 $\frac{W}{cm^2}$
Deck Absorbtivity	0.7	0.7	0.7	0.7
$k_{concrete}$	0.8 $\frac{Btu}{hr\text{-}ft\text{-}F}$	0.014 $\frac{W}{cm\text{-}C}$	0.8 $\frac{Btu}{hr\text{-}ft\text{-}F}$	0.014 $\frac{W}{cm\text{-}C}$
k_{steel}	31.0 $\frac{Btu}{hr\text{-}ft\text{-}F}$	0.536 $\frac{W}{cm\text{-}C}$	31.0 $\frac{Btu}{hr\text{-}ft\text{-}F}$	0.536 $\frac{W}{cm\text{-}C}$
$h_{above\ deck}$	1.22 $\frac{Btu}{hr\text{-}ft^2\text{-}F}$	0.215 $\frac{W}{m^2\text{-}C}$	1.22 $\frac{Btu}{hr\text{-}ft^2\text{-}F}$	0.215 $\frac{W}{m^2\text{-}C}$
$h_{below\ deck}$	0.73 $\frac{Btu}{hr\text{-}ft^2\text{-}F}$	0.129 $\frac{W}{m^2\text{-}C}$	0.73 $\frac{Btu}{hr\text{-}ft^2\text{-}F}$	0.129 $\frac{W}{m^2\text{-}C}$
$Air_{above\ deck}$	120.0 F	49.0 C	110.0 F	43.0 C
$Air_{below\ deck}$	95.0 F	35.0 C	90.0 F	32.0 C

The resultant theoretical temperature profiles for Trial 1 (full input) and Trial 2 (reduced input) are shown in Fig. 44. These curves closely match the experimental curves as illustrated in Fig. 45 (typical Series One test) and Fig. 46 (typical Series Two test).

After the numerical values of Table 1 were established and the experimental and theoretical profiles compared, the influence of the various parameters on Trial 1 temperature profiles was studied.

The conductivity of the concrete has the least effect on the profile. Increasing this parameter to 1.0 Btu/hr-ft-F (0.017 W/cm-C) yielded values in Fig. 47. Increasing the conductivity caused more heat to transfer through the cross section, and the temperatures in the lower portion of the section were raised. The conductivity of steel was not altered as it is well documented and changes minimally with such factors as age and weather. The conductivity of concrete, however, is a function of many parameters including moisture content, mix proportions, and aggregate types[4, 7, 10, 22, 27].

Ambient air temperature and convection film coefficients have the greatest effect on temperature profiles. For testing in a controlled environment, values for these two parameters can be selected with a good degree of confidence. For actual field structures, these values are difficult to establish, as they vary greatly as a function of air velocity (wind) across exposed surfaces.

On a still day, the ambient air temperature lies somewhere between the surface temperature of the deck and the temperature at some distance (say, 20 ft [6.1 m]) away from the structure. In laboratory tests with the deck surface 60 to 80 F (33 to 44 C) warmer than the air at some distance away from the structure, the ambient air

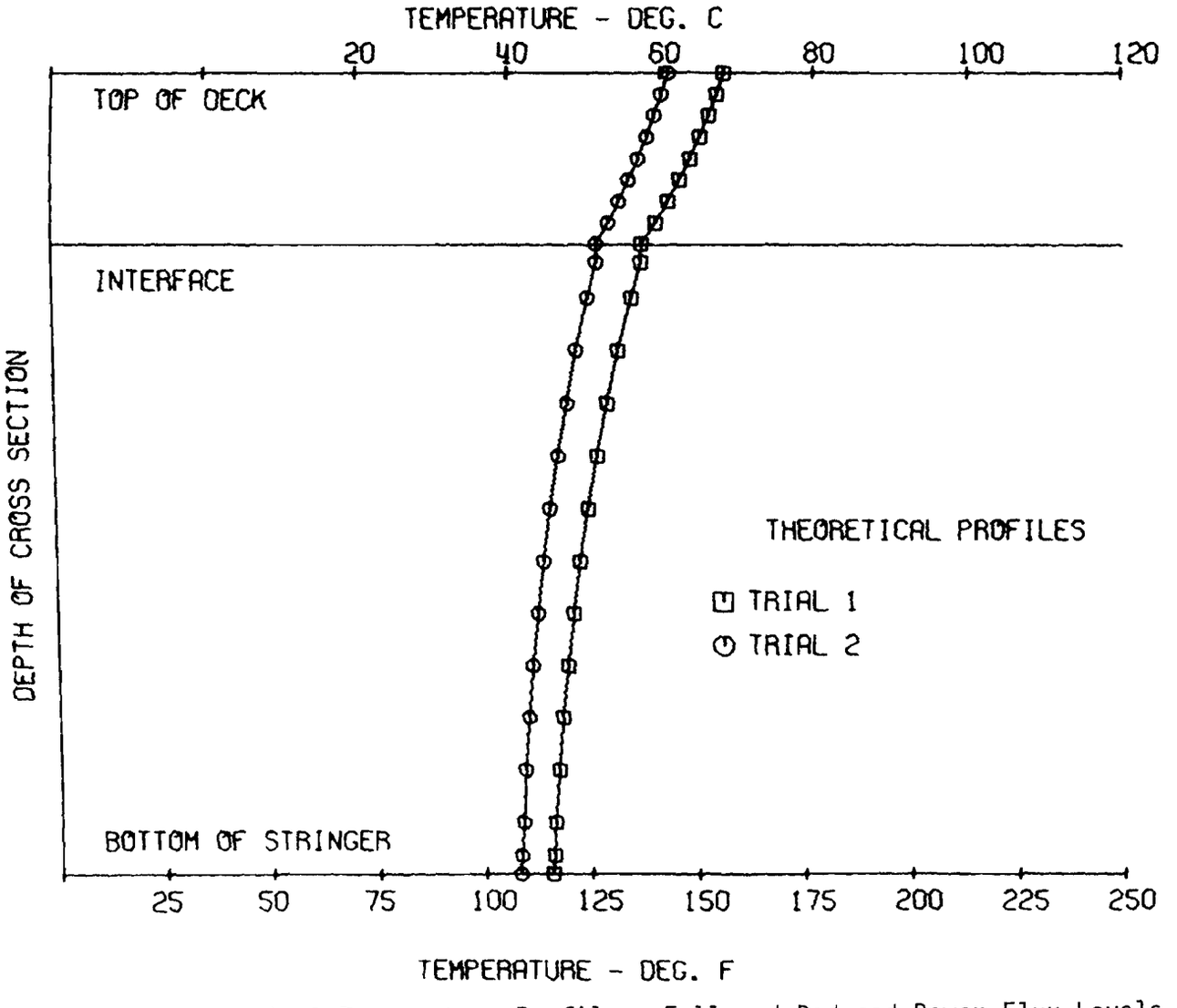

Fig. 44. Theoretical Temperature Profiles, Full and Reduced Power Flux Levels

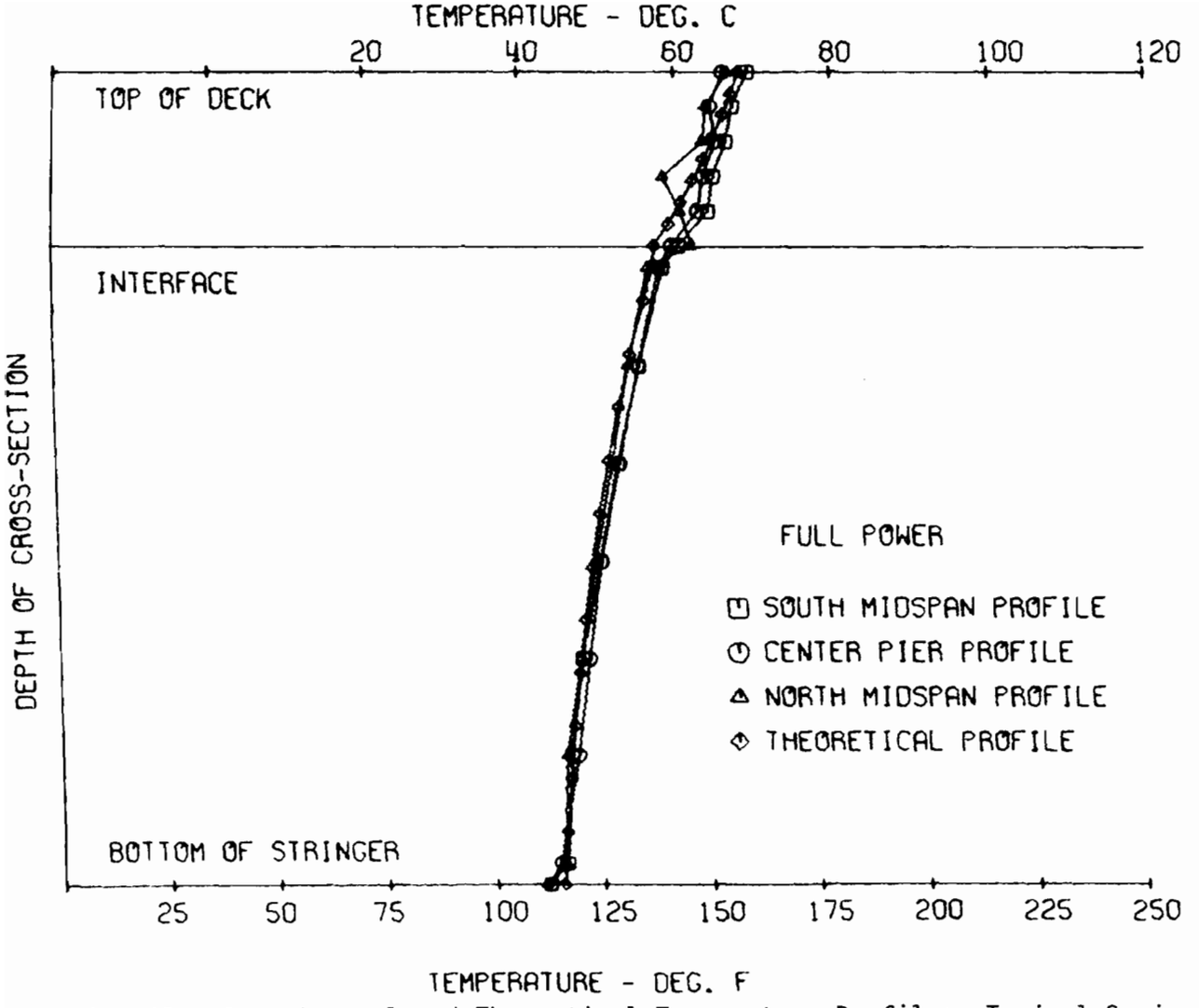

Fig. 45. Experimental and Theoretical Temperature Profiles, Typical Series One Test

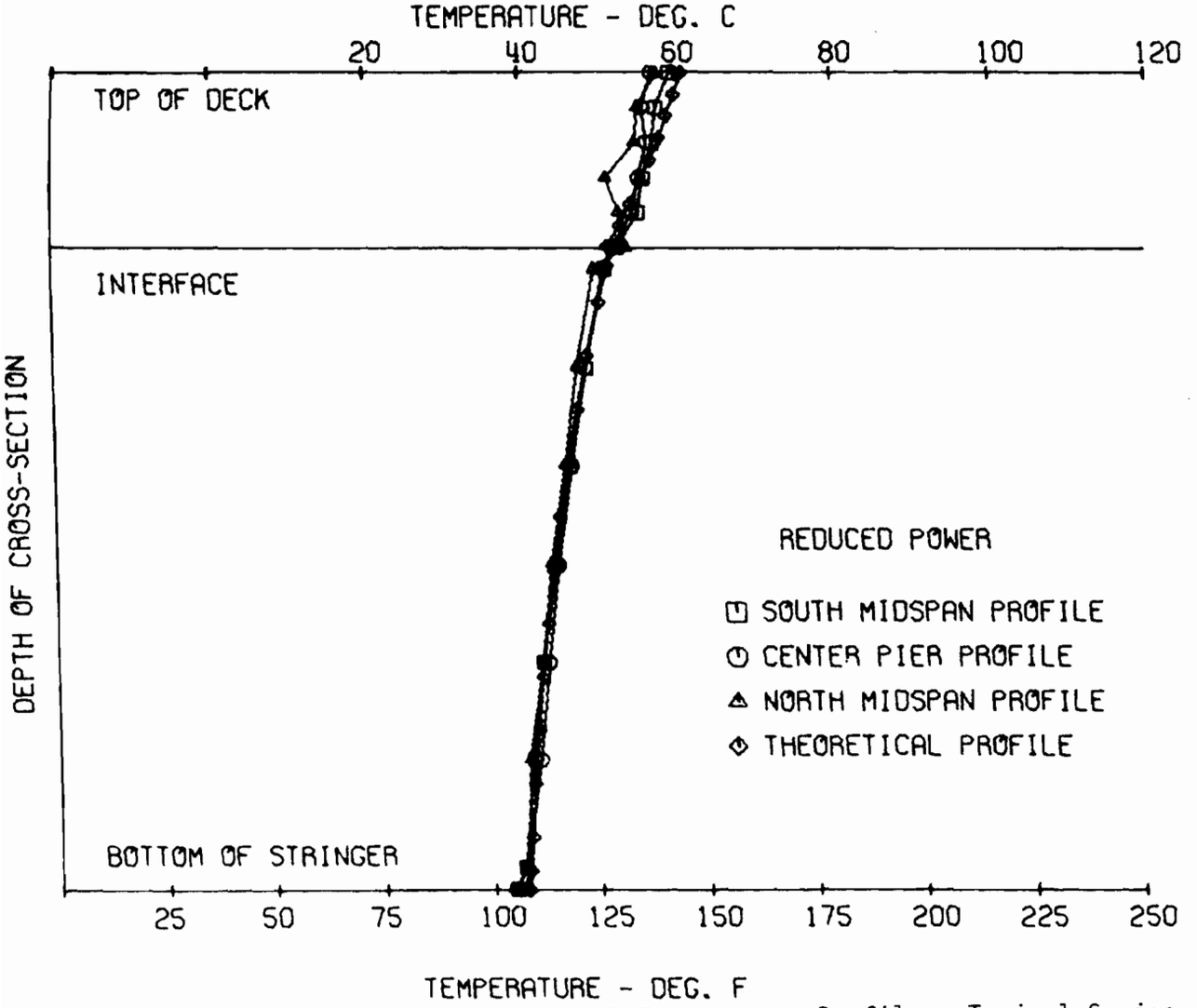

Fig. 46. Experimental and Theoretical Temperature Profiles, Typical Series Two Test

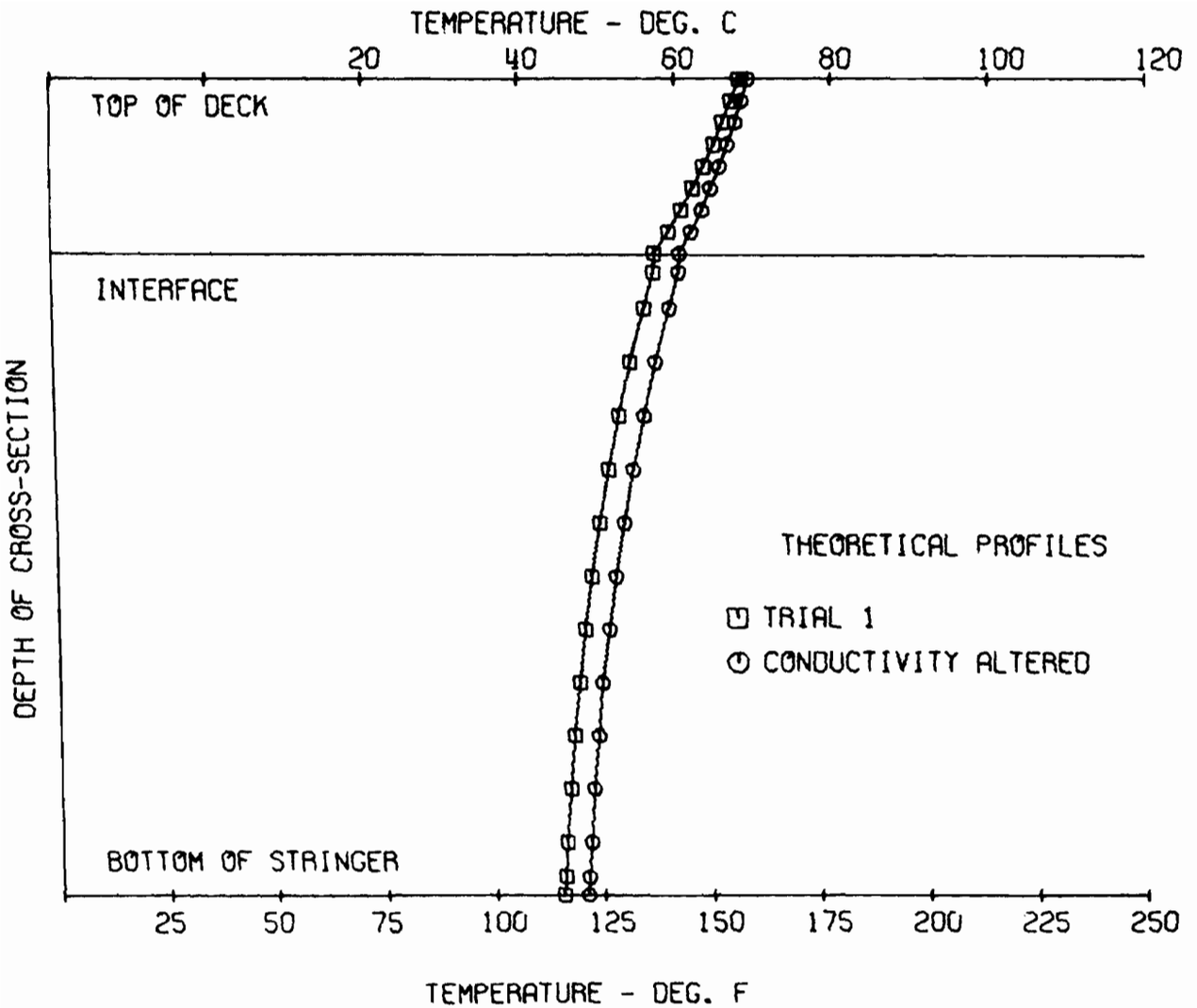

Fig. 47. Effect of Conductivity on Temperature Profile

temperature above the deck was found to be approximately the average of the surface temperature and that of the surrounding air, and the ambient temperature beneath the deck was 15 to 20 F (8 to 11 C) above that of the surrounding air. Ambient air temperatures decrease and approach the surrounding air temperature as the wind velocity across the surface increases. This induces forced convection and turbulent flow for a composite design structure.

As previously stated, the convection film coefficient also is a function of air velocity. As the velocity increases, the coefficient also increases allowing for a more rapid heat flow from the structure. This is illustrated by Eq. 79.

The effect of ambient air temperature on Trial 1 is shown in Fig. 48. The modified air temperatures are 110 F (43 C) above the slab and 90 F (32 C) below the deck. Fig. 49 shows the effect of varying the convection film coefficient. Trial 1 is compared with an altered profile for h above the slab of 5.0 Btu/hr-ft^2-F (28.4 W/m^2-C) and 3.0 Btu/hr-ft^2-F (17 W/m^2-C) below the deck. The value of h used above the deck represents an upper bound for the coefficient resulting from natural convection. From these profiles, it can be seen that the temperature through a section decreases markedly as the wind speed increases.

As described previously, exact values for film coefficients can be obtained only by elaborate wind tunnel studies for a particular design. In adapting this finite element approach, or any numerical analysis to actual field structures, fairly reliable values for convection coefficients can be obtained from rigorous studies of the relation between wind velocity and the physical characteristics of

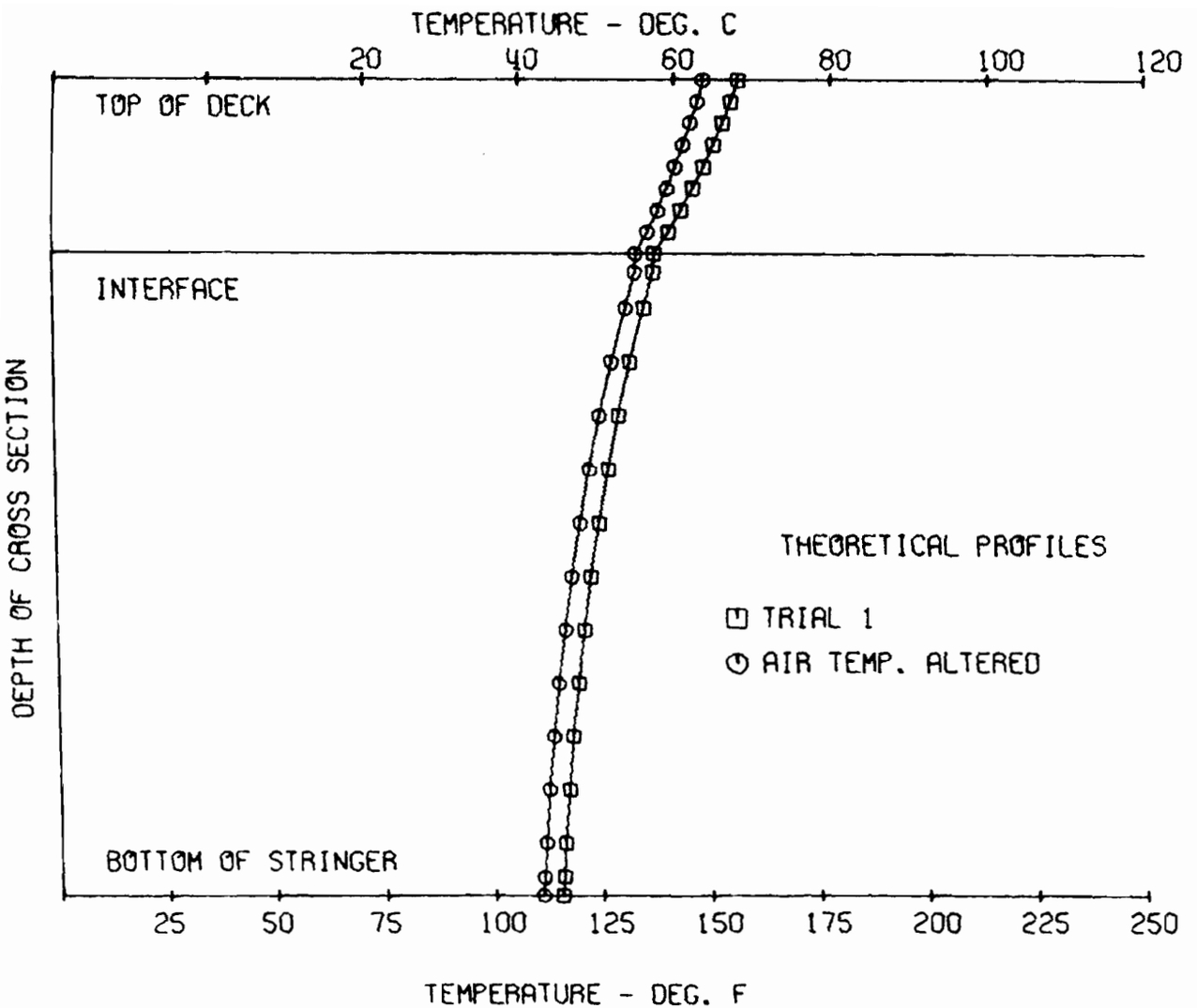

Fig. 48. Effect of Ambient Air Temperature on Temperature Profile

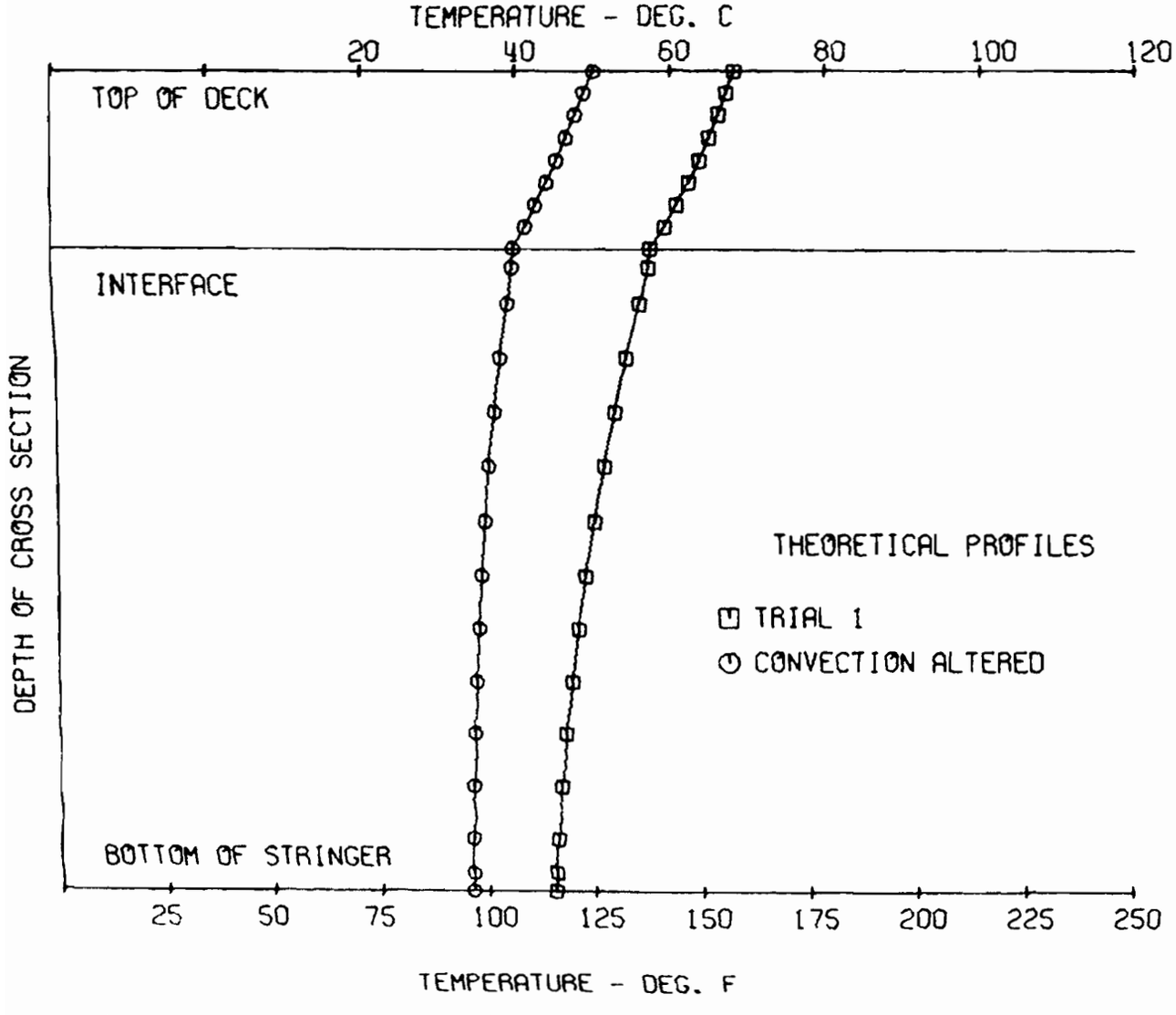

Fig. 49. Effect of Convection Film Coefficient on Temperature Profile

the structure. Values for the ambient air temperature must be estimated until studies are conducted relating the ambient air temperature and wind velocity.

B. STRAIN DISTRIBUTION

As discussed previously, temperature compensated electric resistance strain gauges were mounted on the abutment piling (Fig. 13), the pier (Fig. 14), the transducers of groups 1 through 5 (Fig. 15), and the center stringer at groups 2 through 4 (Fig. 15). These gauges, self-temperature-compensated for mild steel, indicate zero strain when applied to an unrestrained steel member subjected to a temperature change. However, when applied to materials having a coefficient of thermal expansion different from that of steel, the gauges indicate an apparent strain equal to the difference in thermal coefficients times the temperature change. When applied to a partially or totally restrained steel member subjected to a temperature change, the gauges likewise indicate an apparent strain. The true strain on any surface, i.e., the actual movement per unit length, can be calculated by adding the product of the change in temperature times the gauge temperature compensating factor to the recorded apparent strain.

For this study, the electrical resistance properties of the gauge were independent of temperature below 100 F (38 C). Above this temperature, an apparent strain was introduced into the recorded values. The electrical resistance-apparent strain relationship is shown on graphs furnished by the strain gauge manufacturer for use in data reduction. For the temperature range and the gauges of this study, the curve is nearly linear, ranging from zero apparent strain at 100 F (38 C) to an apparent strain of -100 micro strain at 200 F

(93 C).

The recorded strains included apparent strain resulting from the effects of change in electrical resistance, restraints (abutments and pier), and dissimilar materials. An apparent strain resulting from a difference in thermal coefficients of expansion was also induced in the glass slide transducers. A computer program was developed for data reduction and apparent strain correction.

Recorded and temperature compensated strain profiles are shown in Figs. 50 through 61. Strains for repeated tests fall within a narrow bandwidth similar to that observed for the temperature profiles. The strain profiles for transducer group 2, south midspan, for Series One tests (full heat flux) and for Series Two tests (reduced heat flux) are shown in Figs. 50 and 51 respectively. It should be noted that the compensated Test 2 values of Fig. 51 are misleading. As explained previously, the temperature profile for this test ran a constant 6 F (3.3 C) lower than Tests 1 and 3 under the same conditions. The compensated strains are a function of temperature and, thus, the Test 2 values are lower by a corresponding amount. The recorded strains of Fig. 51 are in close agreement. If the 6 F (3.3 C) difference was included in the Test 2 strain compensation, this profile would closely agree with those of Tests 1 and 3. Recorded and compensated strains for Series One and Series Two tests, respectively, at the center pier are shown in Figs. 52 and 53 and at the North midspan in Figs. 54 and 55.

Individual recorded and compensated strain test profiles are shown in Figs. 56 through 61. These figures show the relation of the strains along the length of the bridge, i.e., at instrument groups 2,

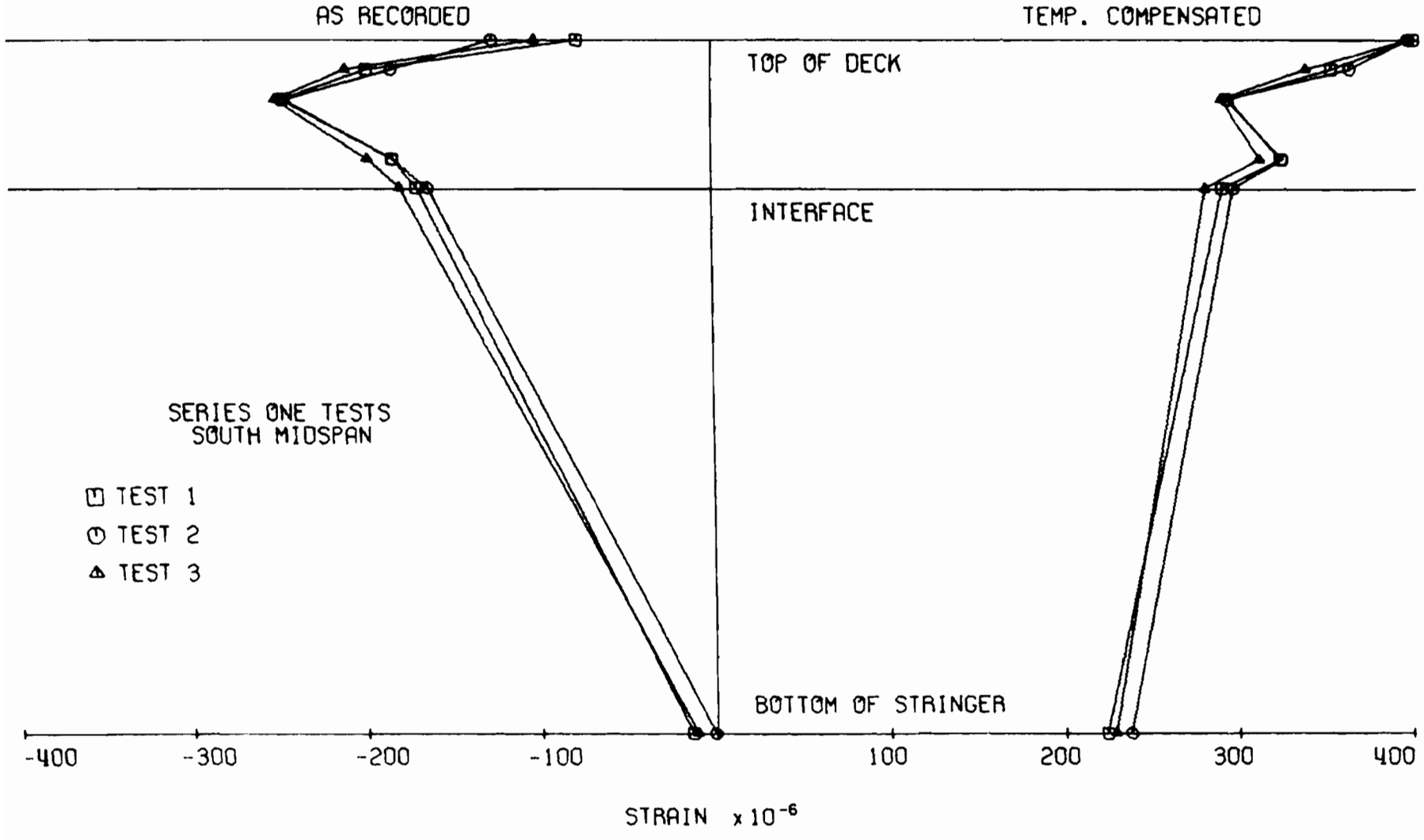

Fig. 50. Strain Profiles, South Midspan, Series One

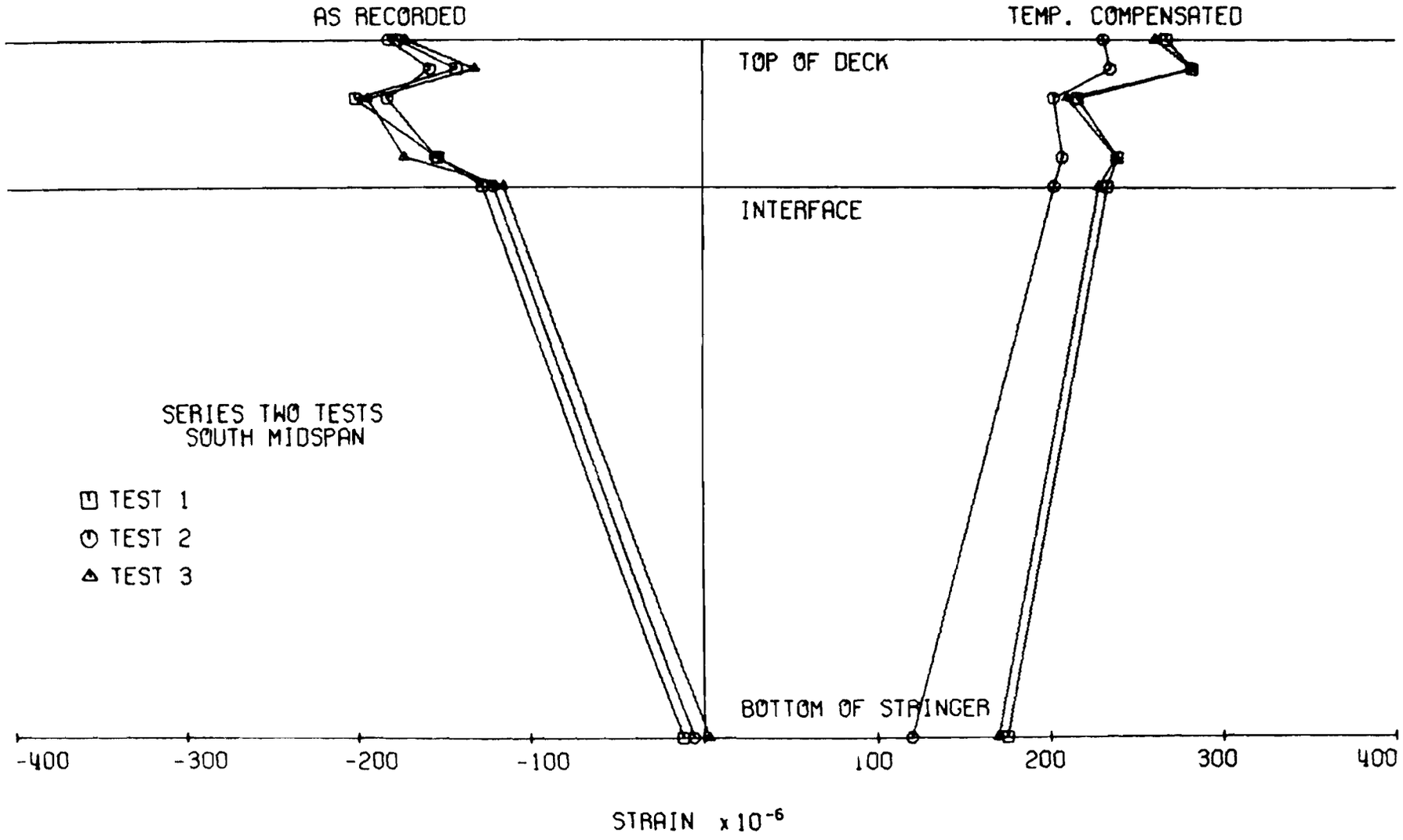

Fig. 51. Strain Profiles, South Midspan, Series Two

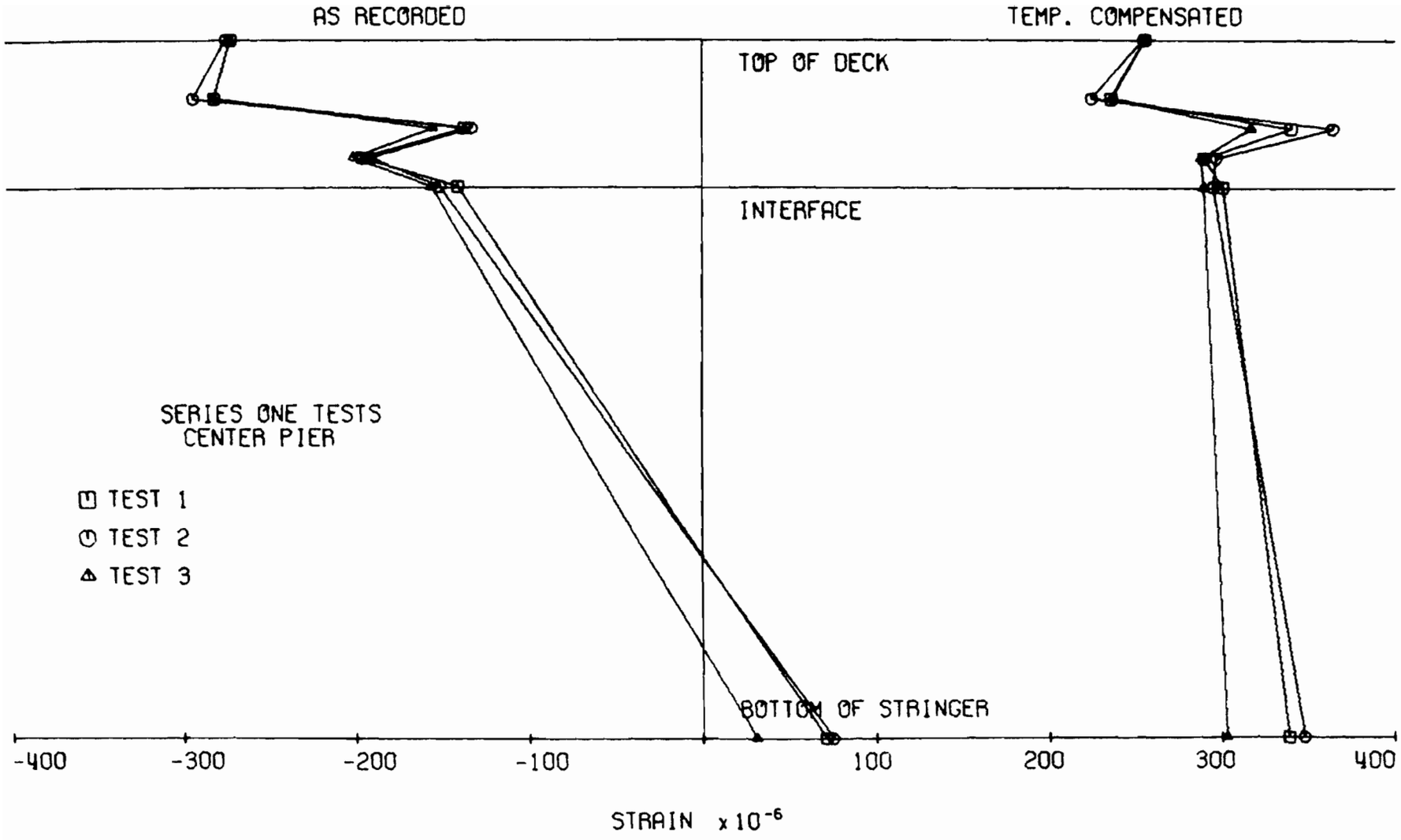

Fig. 52. Strain Profiles, Center Pier, Series One

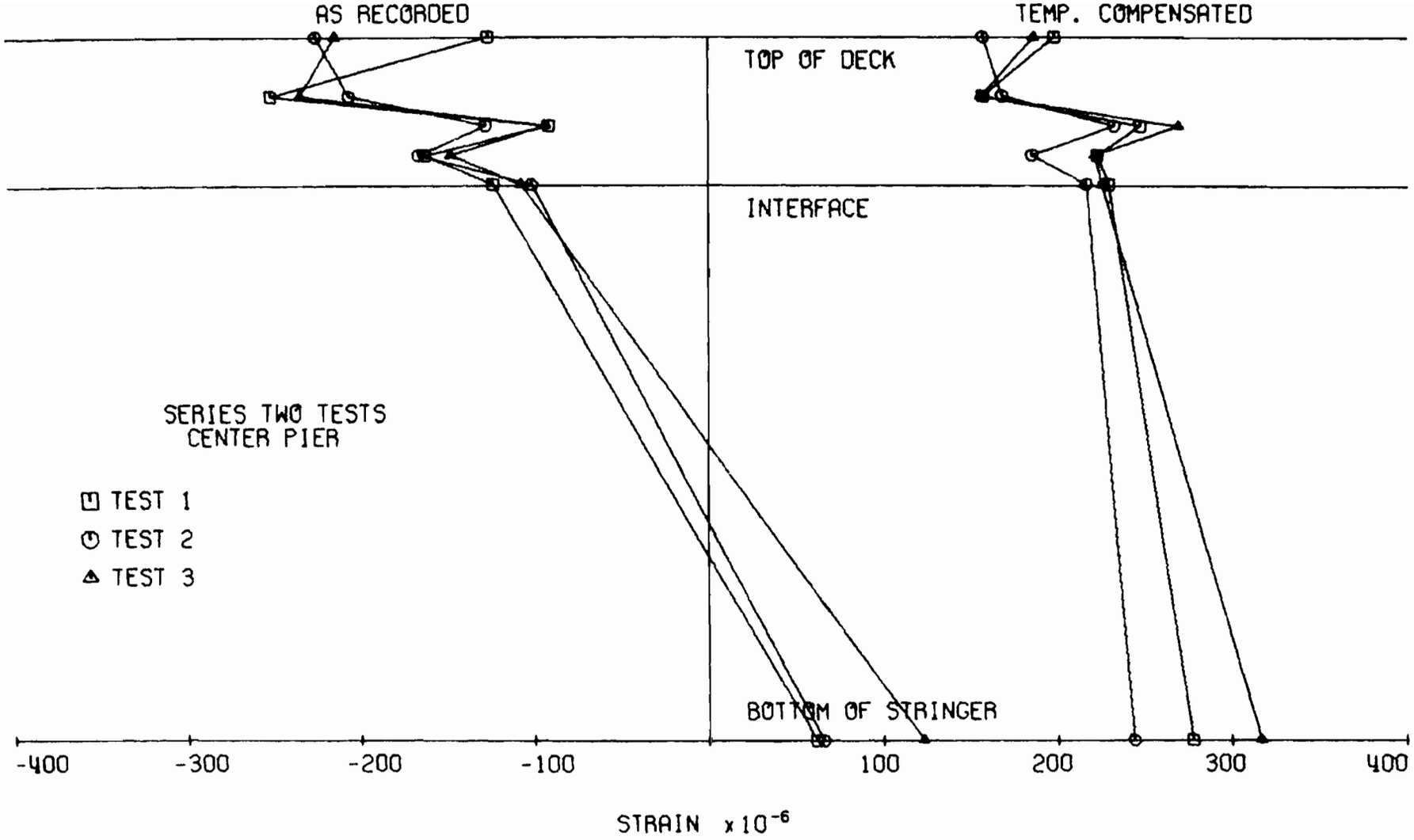

Fig. 53. Strain Profiles, Center Pier, Series Two

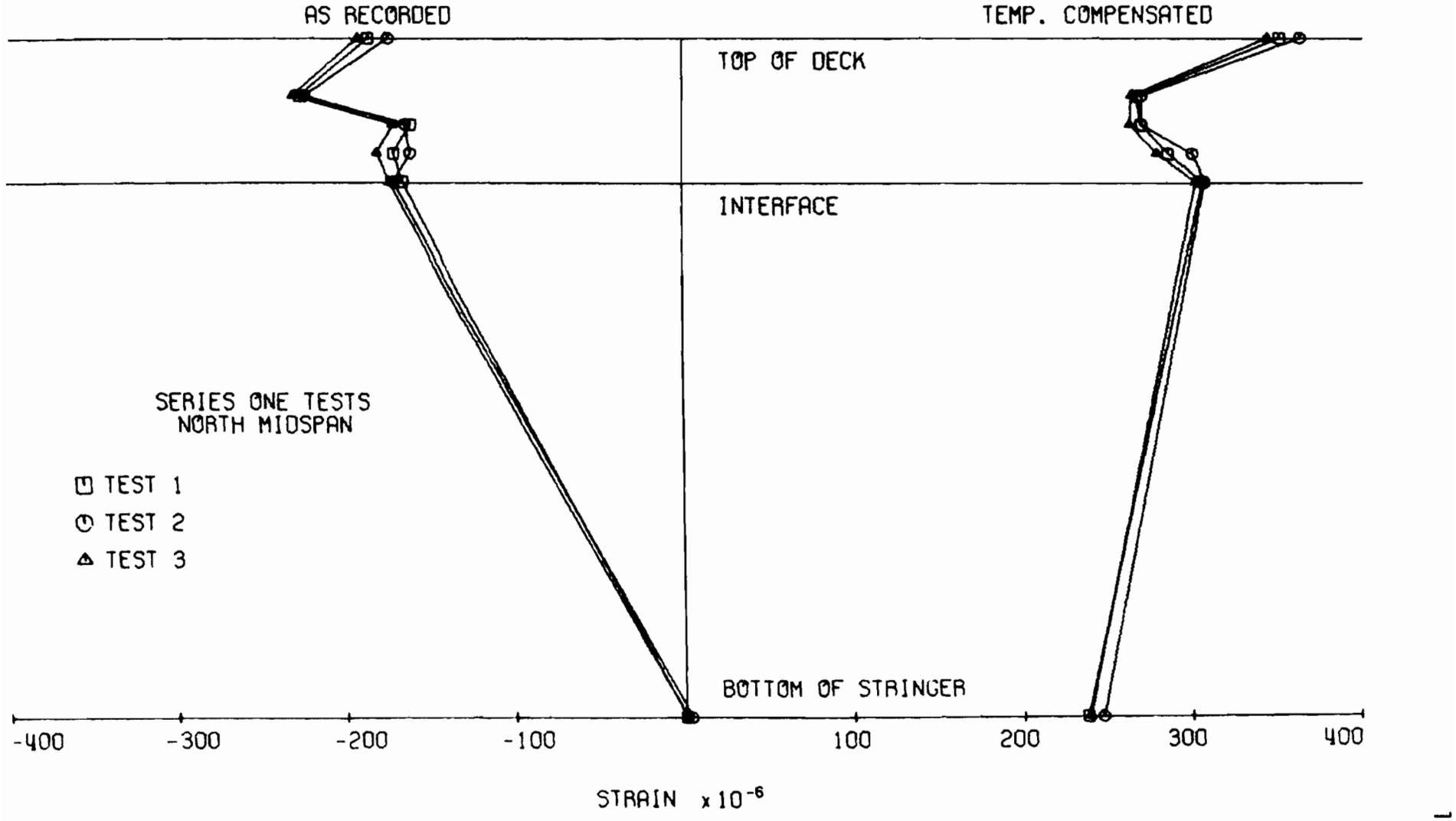

Fig. 54. Strain Profiles, North Midspan, Series One

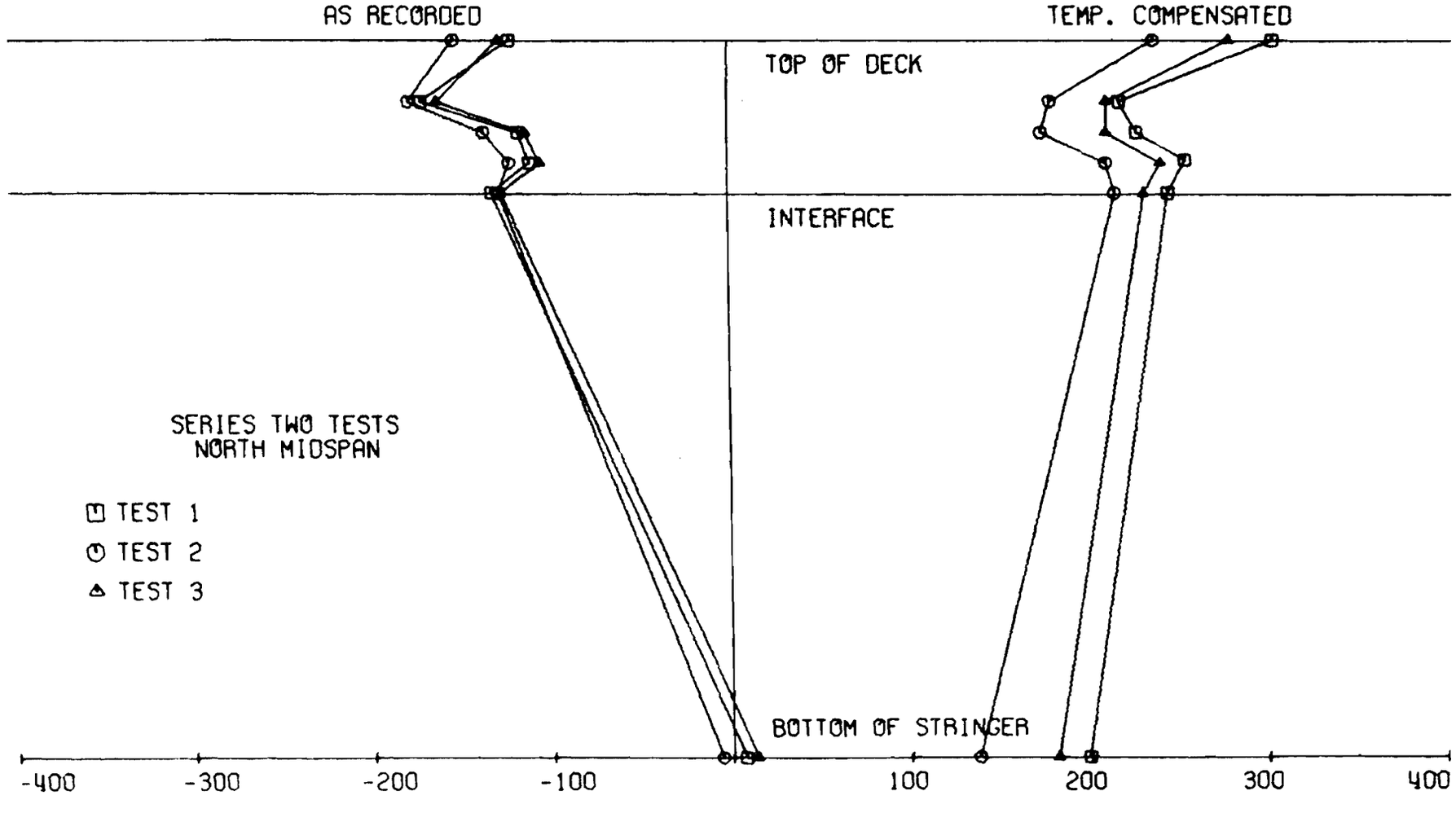

Fig. 55. Strain Profiles, North Midspan, Series Two

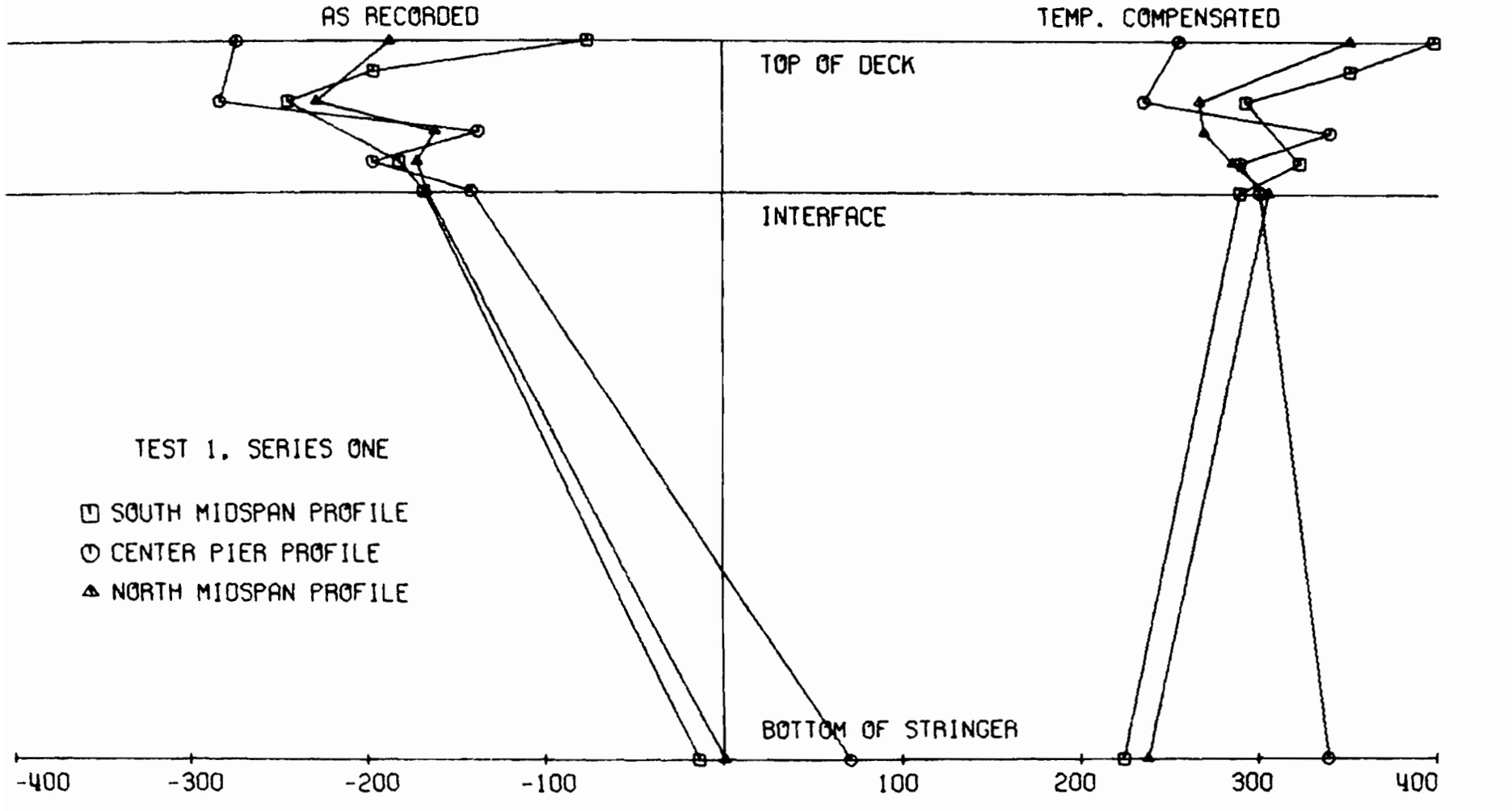

Fig. 56. Strain Profiles, Test 1, Series One

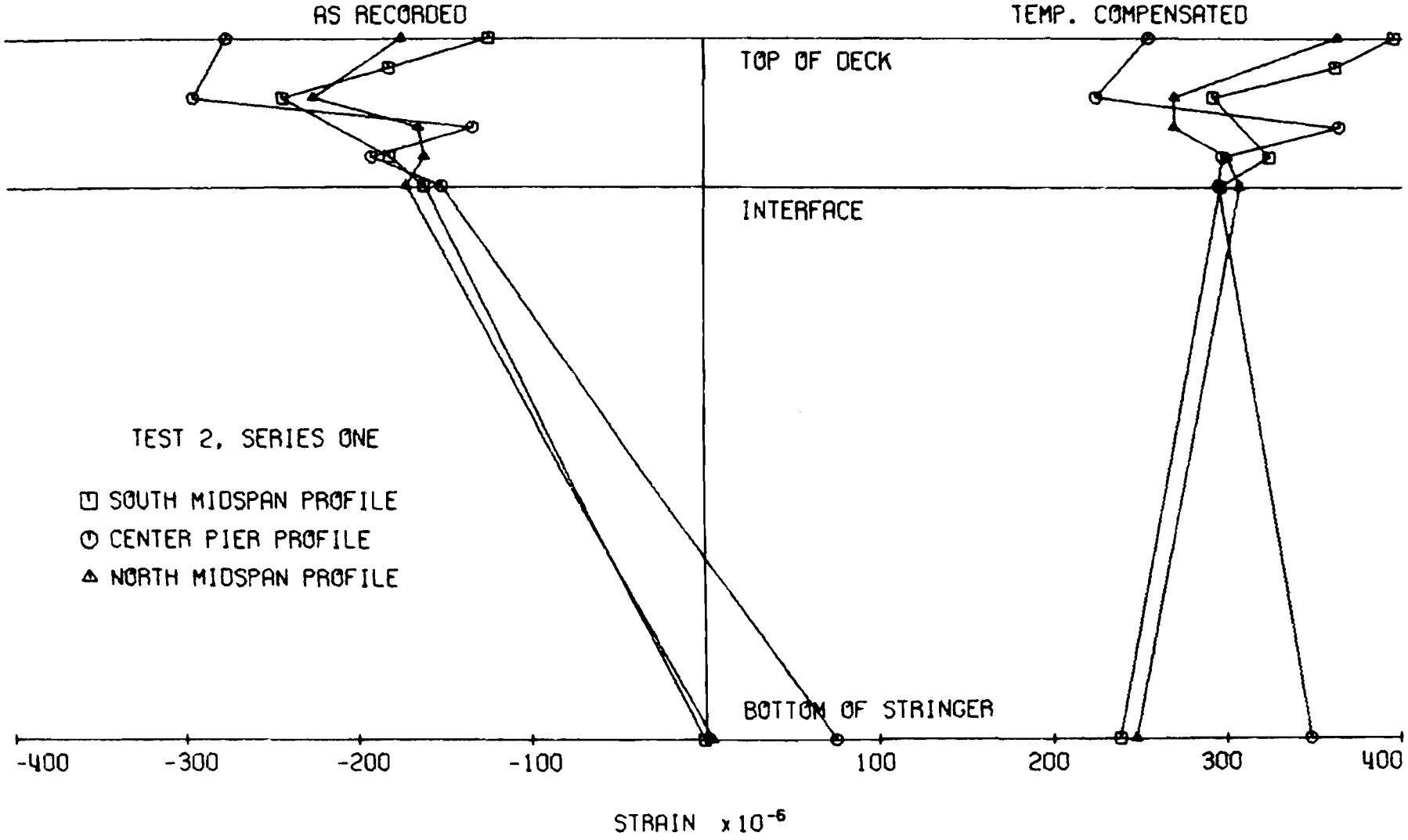

Fig. 57. Strain Profiles, Test 2, Series One

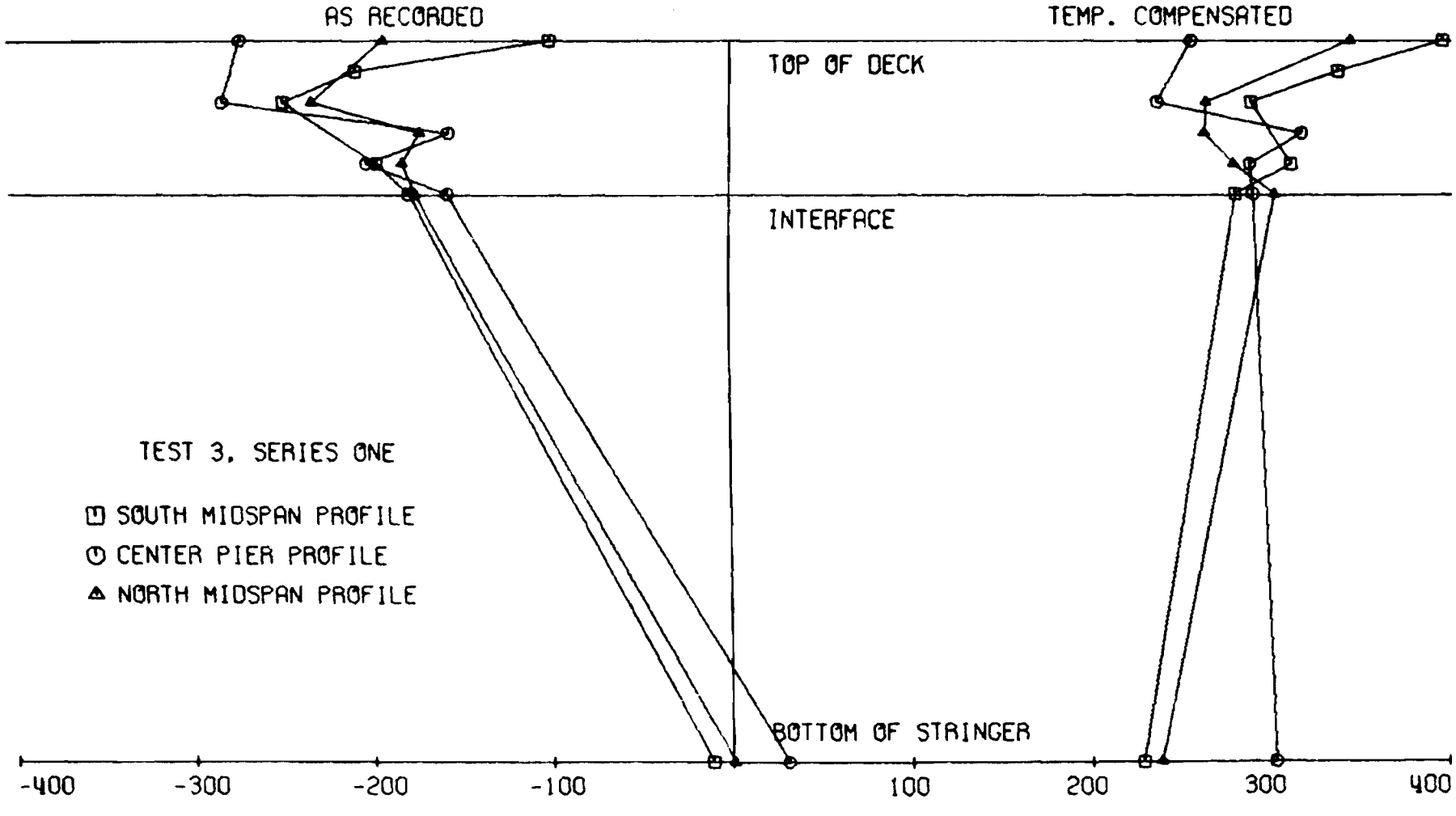

Fig. 58. Strain Profiles, Test 3, Series One

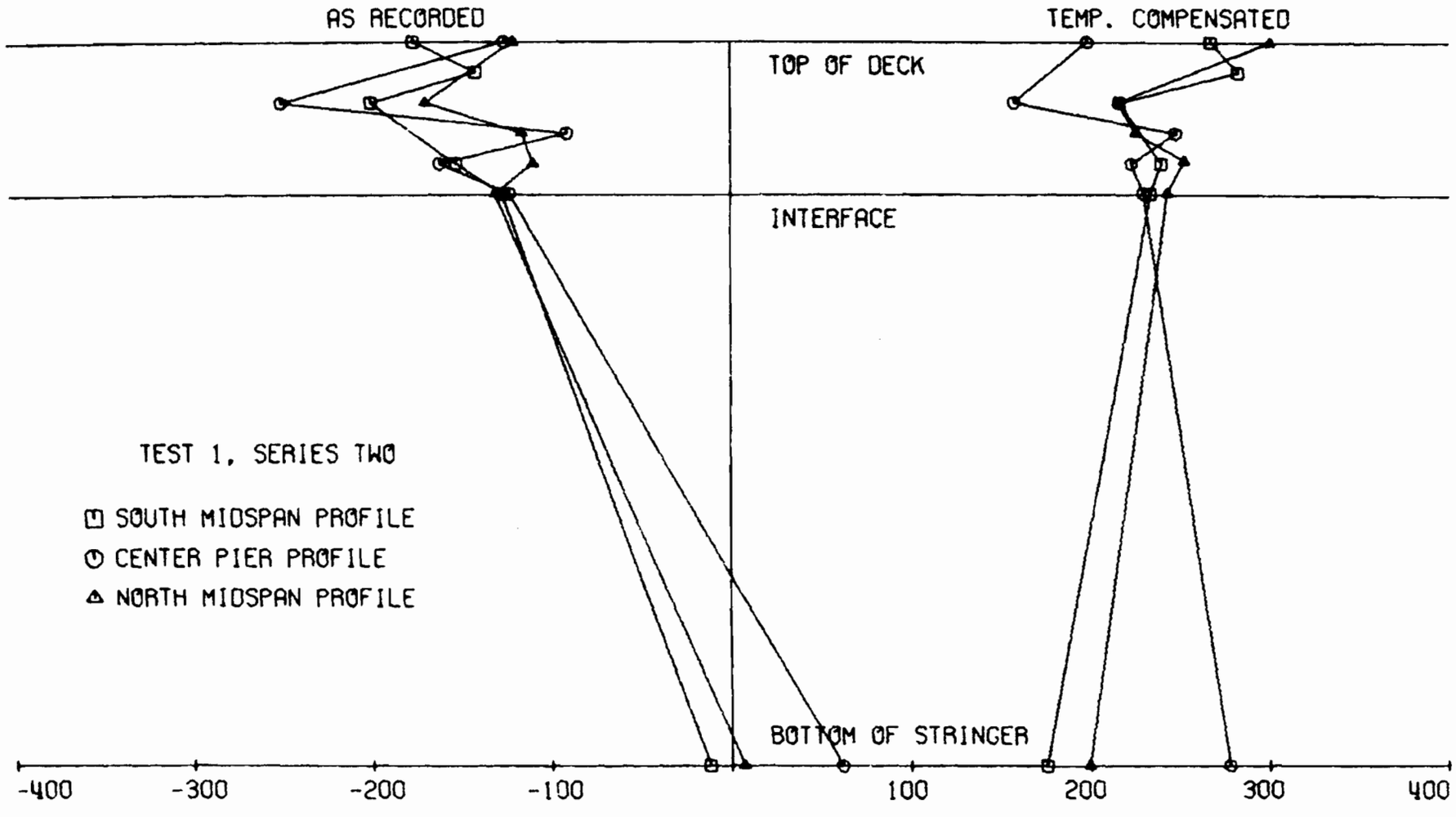

Fig. 59. Strain Profiles, Test 1, Series Two

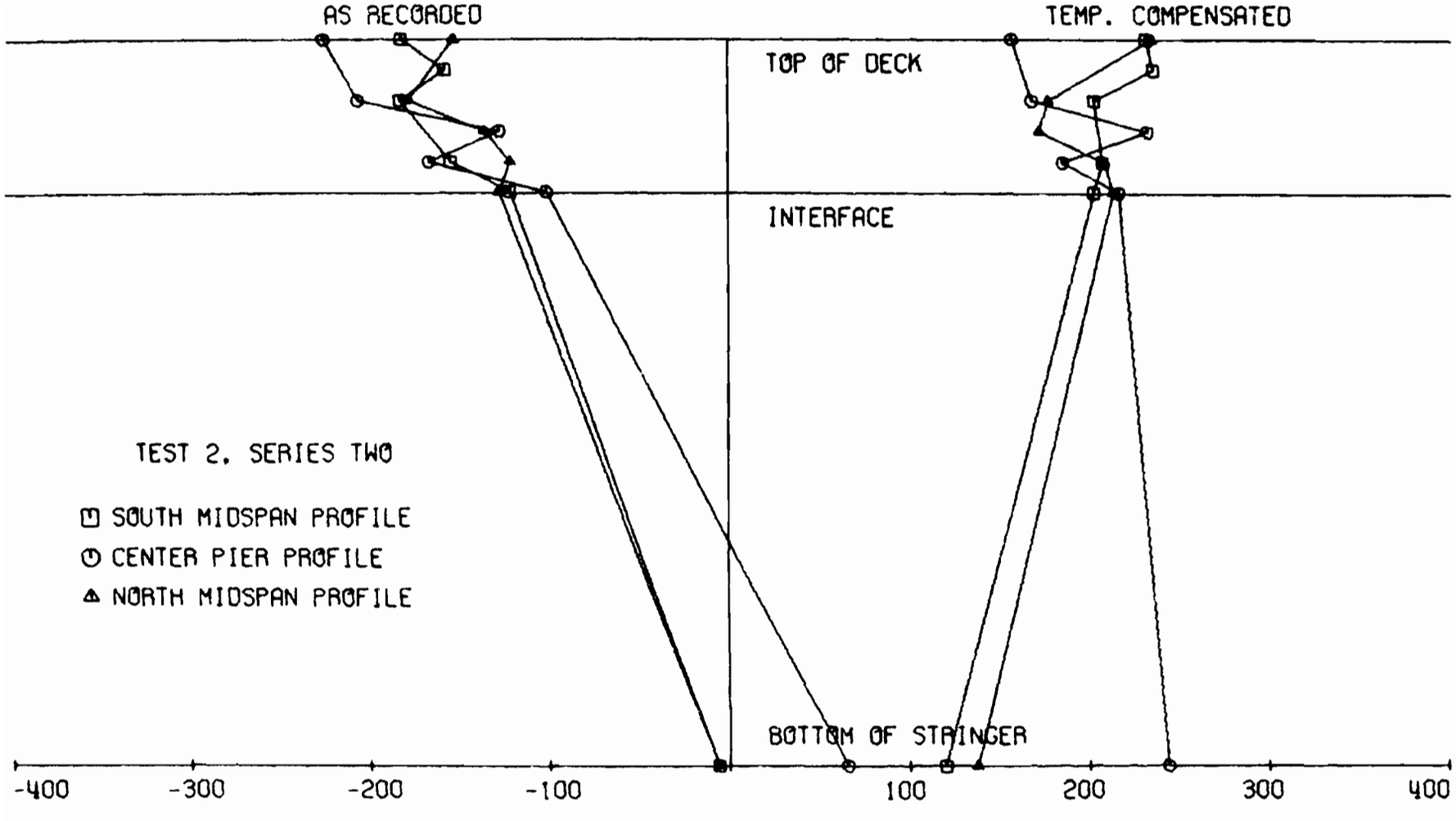

Fig. 60. Strain Profiles, Test 2, Series Two

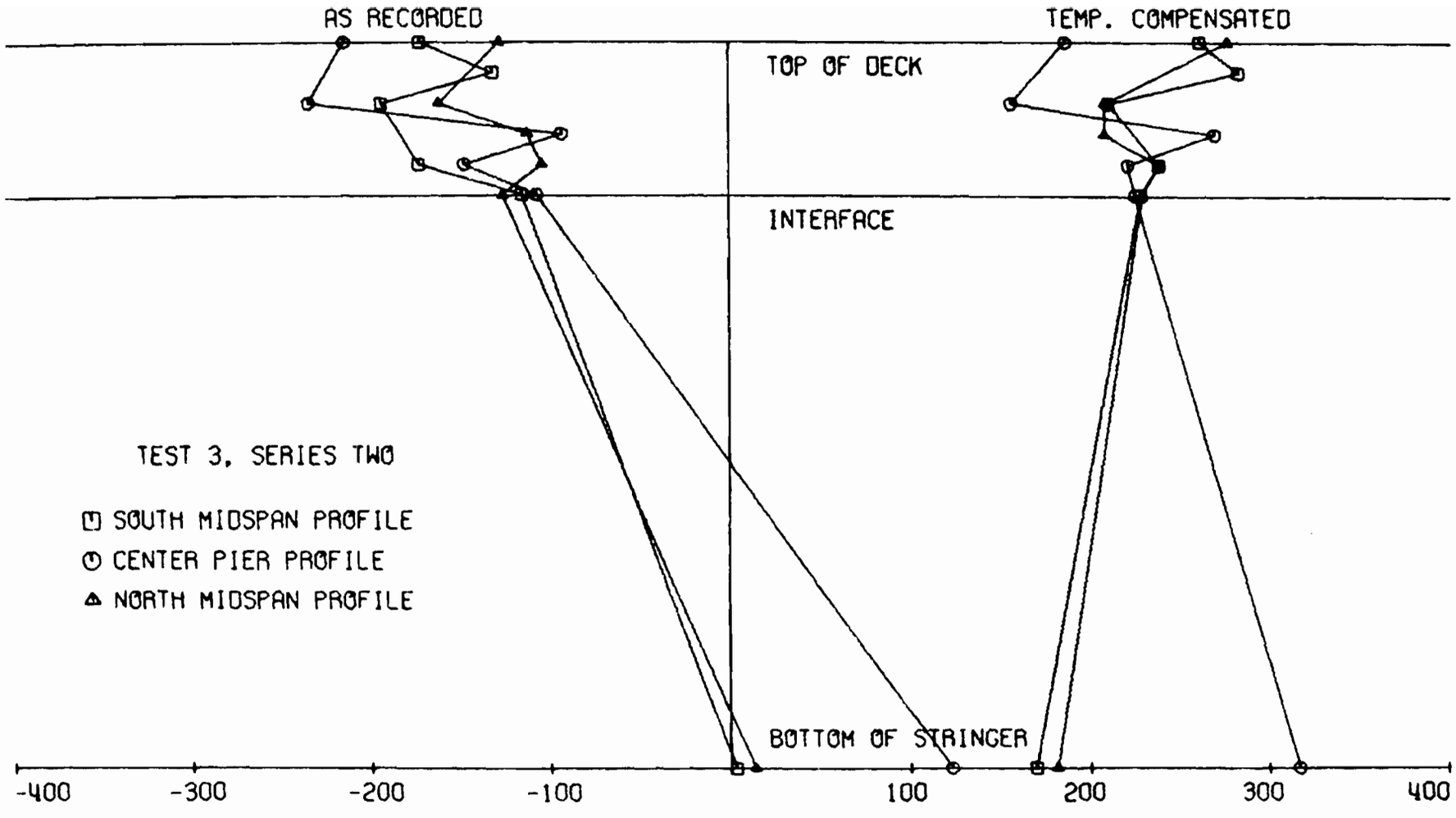

Fig. 61. Strain Profiles, Test 3, Series Two

3, and 4.

After the test structure was constructed, several gauges were found to be unstable or inoperative. These failures could have been caused during placement of the slab or by possible malfunction of the instruments. Readings that would have been recorded at these points are missing from the profiles.

In contrast to the temperature profiles, an erratic pattern of strains is apparent in the slab. These patterns could be the result of a number of things: imperfect bonding or slippage between the transducers and the deck or honeycombs or air voids in the concrete around the instrument groups. The latter could result from inadequate emplacement of the concrete around the congestions of transducers in the slab. All patterns, however, are consistent for a given series of tests.

From the data obtained from the cantilever sections of instrument groups 1 and 5, the coefficient of thermal expansion for the limestone aggregate concrete was determined to be $3.5 \times 10^{-6}/F$ ($6.3 \times 10^{-6}/C$). This compares closely with calculated design values obtained from the method of Emanuel and Hulsey[18]. The experimental value is used later in calculations of theoretical strains.

The strain profiles indicate negative curvature at the midspan locations and positive curvature above the center pier. These relationships are compatible with the temperature profiles, i.e., the top of the section is warmer than the bottom, and with the pier support, which arrests dead load deflection at the support.

There was no differential strain at the base of the center pier, which indicates that no longitudinal displacement occurred at the

bearing elevation of the pier thus resulting in symmetrical longitudinal displacements about the center of the structure. This symmetrical action was substantiated by the dial indicator readings at the abutments that were virtually identical for each of the tests in a given series.

Strains recorded from the piling gauges were very erratic and no plausible explanation, conclusions, or trends could be deduced.

The previously described procedure of Emanuel and Hulsey[17] and the computer program developed by Hulsey[22] were used to obtain the theoretical strains. Experimental rather than the theoretical temperature profiles were used to calculate the theoretical strains that were correlated with the experimental strains. The following material properties were used to calculate the theoretical values:

Young's Modulus-Steel.....30.0 x 10^6 psi (2.1 x 10^8 kN/m^2)

Young's Modulus-Concrete.....3.0 x 10^6 psi (2.1 x 10^7 kN/m^2)

Poisson's Ratio-Steel.....0.3

Poisson's Ratio-Concrete.....0.2

Coef. of Thermal Exp.-Steel.....6.5 x 10^{-6}/F (11.7 x 10^{-6}/C)

Coef. of Thermal Exp.-Concrete..3.5 x 10^{-6}/F (6.3 x 10^{-6}/C)

Three cases (previously described) were analyzed: a) both the slab and the beam in plane stress, b) the slab in plane strain and the beam in plane stress, and c) the slab in some state between plane stress and plane strain (partially restrained) and the beam in plane stress. The theoretical strain profiles for the three cases are shown for full and reduced power flux levels in Figs. 62 and 63, respectively. The uncommon coincidence of the midspan and the pier profiles for case a, slab in plane stress, and case c, slab partially restrained, results from the particular combination of material and

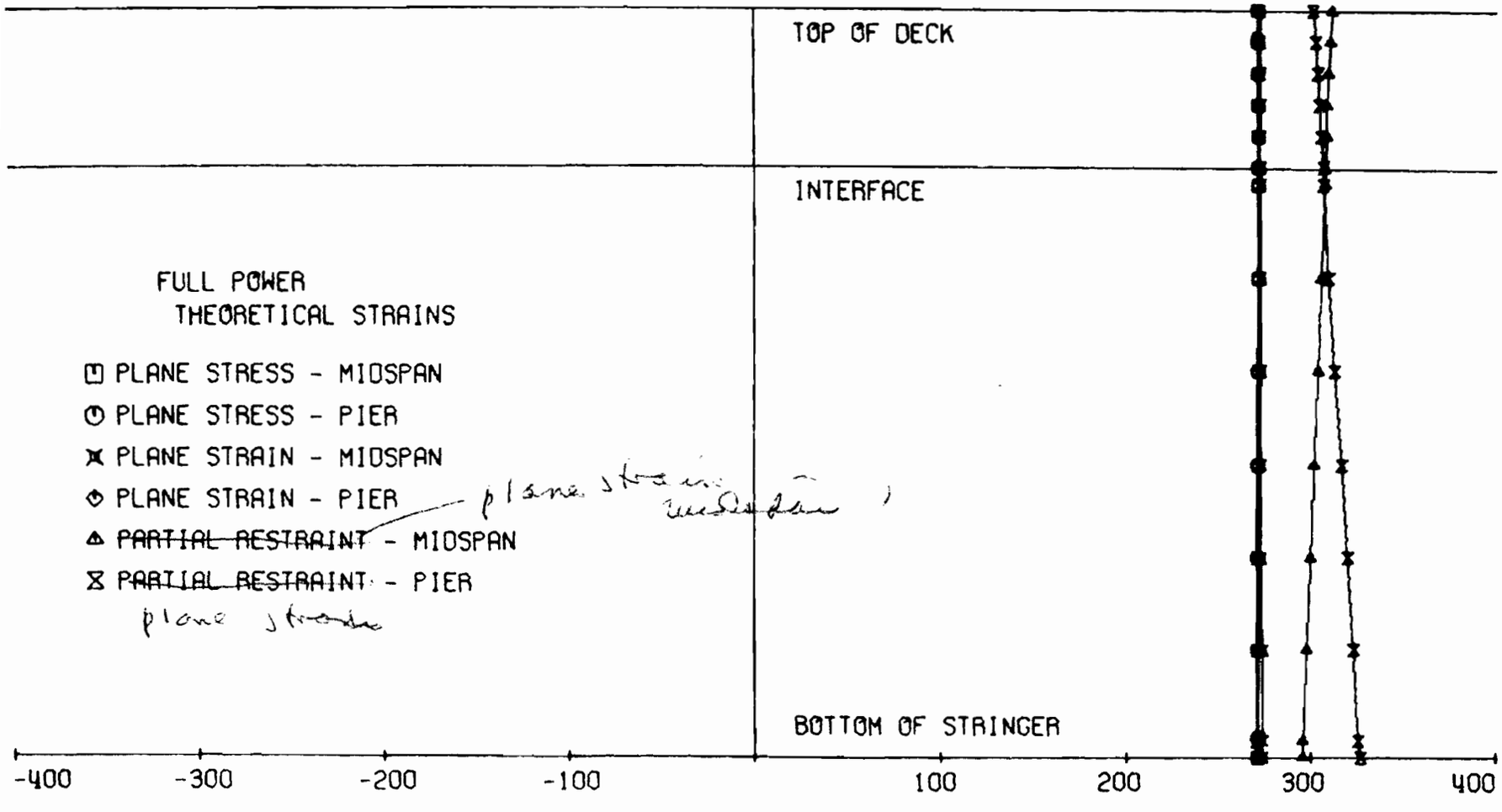

Fig. 62. Theoretical Strain Profiles, Full Power Flux Level

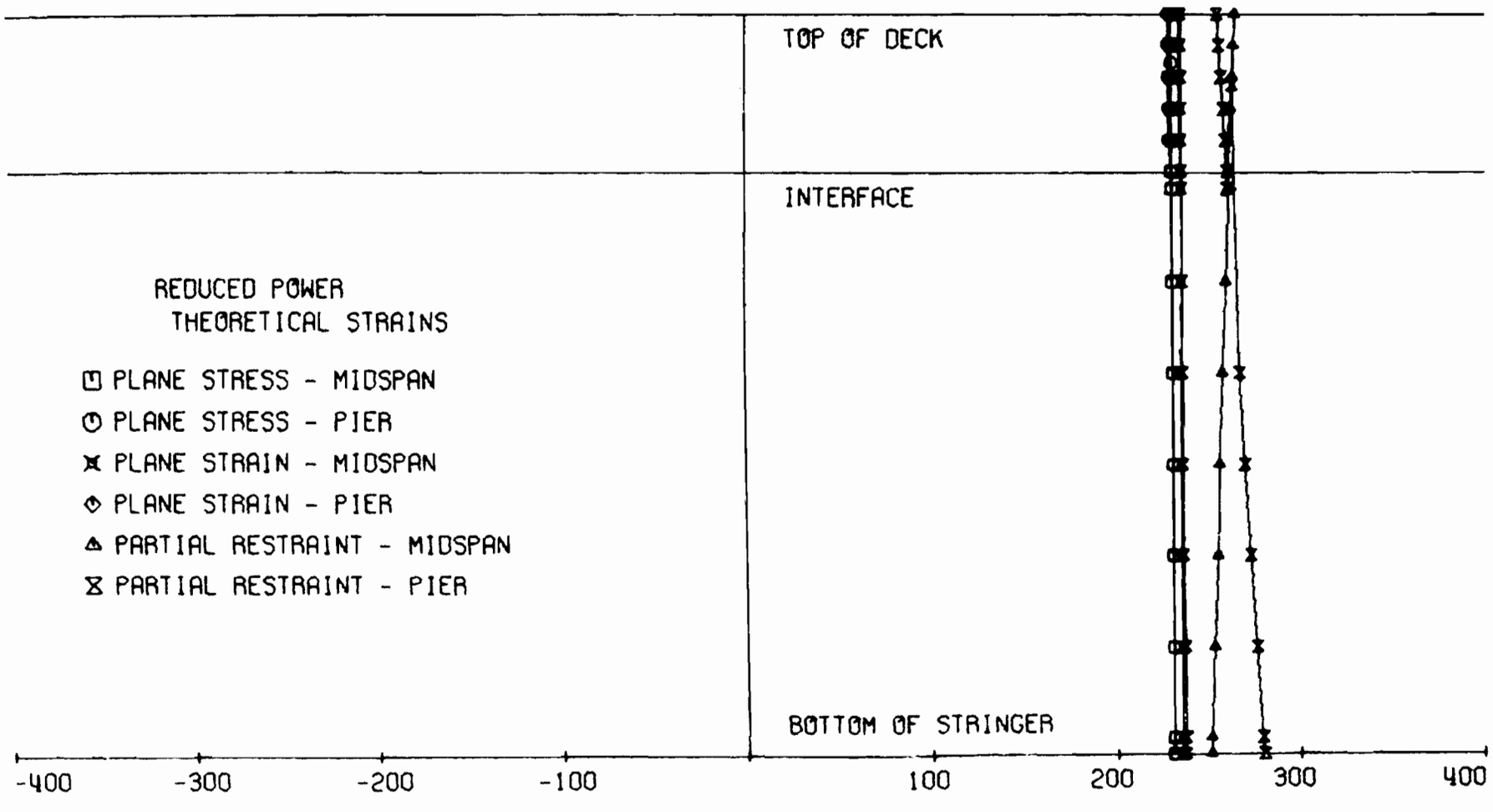

Fig. 63. Theoretical Strain Profiles, Reduced Power Flux Level

cross section geometric properties and the temperature profiles of the test structure. The vertical orientation of the profiles indicates very little longitudinal curvature of the cross section at the midspan and pier, thus resulting in very small calculated vertical deflections at the midspan.

Superposition of the experimental (Figs. 56 through 61) and the theoretical strains (Figs. 62 and 63) shows close general agreement. Also, the observed and theoretical longitudinal deck displacements at the bearing elevation of the abutments differ by only 10 to 15 percent of the measured and theoretical values.

The only experimental and theoretical values not in reasonable agreement, excluding strain scatter in the slab, are the vertical deflections at the midspans and the curvatures at both the midspan and pier. These deflections and curvatures are both functions of differential strain values and the vertical distance between the points of strain measurement. The closest agreement between experimental and theoretical curvature is for case b, the slab in plane strain. This case also yielded the largest theoretical calculated vertical deflection, about 25 percent of the observed deflection and a rather poor correlation. However, the experimental strains yield a curvature that would produce deflections quite close to those observed.

Differences in correlation may arise, of course, with either the experimental or theoretical values, or both. Potential sources of experimental error are either faulty gauges or instruments that give inaccurate readings, error in conversion from recorded to compensated strains, and error in determination of the thermal

coefficient of expansion of the concrete deck. If the coefficient of expansion was actually larger than calculated, the theoretical curvatures would have been larger and would have approached those obtained from the tests. However, this would also result in theoretical longitudinal deck displacements and longitudinal strains greater than the observed determined values.

The most plausible explanation for differences in correlation originates at the center pier. The programmed theoretical procedure assumes that no vertical displacement occurs at any support. In the test structure, some vertical deflection was possible at the center pier. As a result of the curved steel rocker plate and pintle, the superstructure was free to deflect vertically upward at the pier, the only restrictions being its own dead weight and the stiffness of the structure. Also, the steel pier was subjected to some temperature increase as the bridge deck was heated. The thermal expansion of the pier would tend to raise the stringers in the same direction that the superstructure would tend to deflect as a result of the thermal loading. The effect of this vertical deflection would be to increase the curvature above the theoretical values and subsequently increase the midspan deflections. An increase in curvature produces an increase in the strain differential for any two points in a vertical cross sectional plane. Adjustment in the theoretical procedure for this differential would produce values in closer agreement with experimental results. Vertical deflections measured at the pier during the tests were slightly less than one-third the recorded deflection of the midspans.

Potential discrepancies between theoretical and experimental strains near the pier could result from the fact that the shear connectors were discontinued near this location, and composite action was not assured at this section. However, the theoretical and experimental strains are in close agreement, and the magnitude of such discrepancy, if any, is not known.

Determination of stress in the theoretical procedure utilizes the interaction of longitudinal, transverse, and vertical strains and Poisson's ratio, with longitudinal strains being the major parameter. In this study, it was feasible to instrument only for longitudinal strain. Thus, a prediction of stress based strictly on experimental observation is not possible. However, because the experimental and theoretical longitudinal strain correlate closely, theoretical stresses calculated from the observed temperature profile are believed to be valid and are presented in Table 2 for Series One tests and discussed in the following. The pattern of stresses for Series Two tests parallel those for Series One tests.

Case c, i.e., the slab in some state between plane stress and plane strain, produces the highest compressive stress in the upper flange of the stringer at both the midspan and the pier. Values for case a, the slab in plane stress, are not quite 10 percent lower and for case b, the slab in plane strain, are 40 percent lower.

Tensile stresses are produced in the lower stringer flange. The highest values at both the midspan and pier are found with method b and slightly lower values result from methods a and c in order of magnitude, respectively.

TABLE II

THEORETICAL SUPERSTRUCTURE STRESSES

Top of Slab--Midspan	9 psi (62 $\frac{kN}{m^2}$)	-31 psi (-214 $\frac{kN}{m^2}$)	-47 psi (-324 $\frac{kN}{m^2}$)
Top of Slab--Pier	11 psi (76 $\frac{kN}{m^2}$)	-42 psi (-290 $\frac{kN}{m^2}$)	-44 psi (-304 $\frac{kN}{m^2}$)
Bottom of Slab--Midspan	140 psi (966 $\frac{kN}{m^2}$)	119 psi (821 $\frac{kN}{m^2}$)	264 psi (1822 $\frac{kN}{m^2}$)
Bottom of Slab--Pier	140 psi (966 $\frac{kN}{m^2}$)	114 psi (787 $\frac{kN}{m^2}$)	264 psi (1822 $\frac{kN}{m^2}$)
Top of Stringer--Midspan	-4380 psi (-30222 $\frac{kN}{m^2}$)	-3290 psi (-22700 $\frac{kN}{m^2}$)	-4890 psi (-33740 $\frac{kN}{m^2}$)
Top of Stringer--Pier	-4380 psi (-30222 $\frac{kN}{m^2}$)	-3340 psi (-23046 $\frac{kN}{m^2}$)	-4880 psi (-33672 $\frac{kN}{m^2}$)
Bottom of Stringer--Midspan	1190 psi (8211 $\frac{kN}{m^2}$)	1910 psi (13179 $\frac{kN}{m^2}$)	1250 psi (8625 $\frac{kN}{m^2}$)
Bottom of Stringer--Pier	1150 psi (7935 $\frac{kN}{m^2}$)	2940 psi (20286 $\frac{kN}{m^2}$)	1150 psi (7435 $\frac{kN}{m^2}$)

For flange stresses, the method producing the largest compressive stresses produced the smallest tensile stresses, and vice versa.

The maximum compressive stress (4890 psi, 33740 [kN/m^2]) in the upper flange occurred at midspan for case c and was approximately 25 percent of the allowable design stress. The maximum tensile stress (2940 psi [20290 kN/m^2]) in the bottom flange occurred at the pier for case b and was nearly 15 percent of the design stress.

Maximum tensile and compressive slab stresses at both the midspan and the pier were produced by case c, the slab in some state between plane stress and plane strain. This is caused primarily by transverse bending in the slab between the stringers. The maximum slab tensile stress (264 psi [1820] kN/m^2]) and the maximum compressive stress (44 psi [304] kN/m^2]) were approximately 10 and 3 percent of the compressive strength of commonly used 3000 psi (20,700 kN/m^2) concrete.

As stated previously, the theoretical procedure is based on the assumption that the pier does not deflect vertically. Upward pier support movement as indicated in the tests reduces the tensile stress in the lower stringer flange; however this movement has only minimal effect on the stress in the upper flange, because this flange is very near the neutral axis of the composite section.

Integral abutments, as contrasted with roller supports, introduce the following effects. As the substucture stiffness increases, changes in the stress patterns result primarily from the interaction of axial, P/A and flexural, My/I stresses produced by the resistance to movement at the abutments. At midspan, the primary influence is an My/I superposition from a moment which induces positive curvature. This results from the resistance of the stiffer abutment (piling) to

rotation of the superstructure. This rotational resistance also reduces the curvature and deflections along the span adjacent to the abutment.

If there is no vertical deflection at the pier, the My/I effect at the pier is produced by a moment which induces negative curvature. This results from decreasing deflection at midspan. The reduced negative curvature at midspan helps produce reduced positive curvature at the pier.

The P/A effect is present at both the pier and at midspan but has less effect on the stresses at any given cross section than does an increase in abutment rotational stiffness. However, if an approach slab abuts the superstructure or abutment cap and resists longitudinal movement, the P/A effect can become very significant.

It should be noted that the theoretical trends discussed are based on the assumption that the center pier does not deflect vertically. If vertical movement occurs, the theoretical values should be modified by the resultant My/I effect for more accurate results.

VIII. CONCLUSIONS

The present investigation was initiated as a result of an increased interest among bridge design engineers in bridge behavior under thermal loading and in the potential magnitudes of thermally induced stresses. It is also recognized that there is a need for intermediate experimental studies toward utilization of theoretical studies in the development of rational design criteria.

Because of the increased usage of bridge superstructures supported by flexible substructures and the apparent lack of information concerning bridge behavior and induced stresses associated with bridges of this type, a prior study was initiated to explore the feasibility of developing rational design criteria for bridges with Semi-Integral end bents. The study, which was titled "An Investigation of Design Criteria for Stresses Induced by Semi-Integral End Bents: Phase I--Feasibility Study"[16], was conducted under the Missouri Cooperative Highway Research Program by the Department of Civil Engineering at the University of Missouri-Rolla. It was concluded that development of rational design criteria for bridges with Semi-Integral end bents is feasible, but the anticipated cost precluded continuation of subsequent phase to fruition as desired.

In a subsequent theoretical study of environmental effects on composite-girder bridge structures at the University of Missouri-Rolla, Emanuel and Hulsey[17] and Hulsey[22] developed a method for analyzing composite-girder bridge structures that are supported by flexible substructures and subjected to environmental loadings.

Recognizing that acceptance of theoretical results and their utilization toward rational design criteria is subject to substantiation by experimental results from model and prototype structures, the present investigation was initiated as an intermediate study to verify the theoretical approach. The objectives of the study were to construct and instrument a small composite design laboratory structure in the Structural Laboratory of the Engineering Research Laboratory at the University of Missouri-Rolla, to subject the structure to thermal loading, and to correlate the experimental results with calculated values obtained from the theoretical study [17, 22]. In addition, the heat transfer phenomenon was investigated, and the experimental results were correlated with values obtained from a theoretical numerical approach[36, 22].

Based on the correlation of consistent readings from multiple runs at two levels of steady-state infrared radiation heat loading and calculated theoretical values the following conclusions were reached:

1. Steady-state temperature profiles can be predicted with reasonable accuracy from the modeling procedures used for the study. These procedures provide an upper bound for both temperatures and subsequent calculated stresses. Actual temperature profiles are generally lower than the modeled steady-state profiles because of the variation in and short duration of given values of the incident heat flux that strikes the surface, whereas the steady-state analysis requires several hours of constant flux application. Wind also tends to reduce temperatures.

2. The correlation confirms that the theoretical procedures are adequate for a reasonable prediction of the behavior of composite-girder bridge structures subjected to thermal loading.
3. The theoretical longitudinal curvature is somewhat smaller than that observed. This is believed to be a result of the assumption that there is no vertical deflection of the supports, whereas the test data indicate a probable upward deflection of the pier.
4. The theoretical and observed longitudinal strains are in reasonable agreement. Resultant stresses in the test structure, being functions of longitudinal, transverse, and vertical strains, can be expected to parallel the theoretical values.
5. Based on the strain profiles, the theoretical procedures give reasonable stress values for the slab and upper flange areas of the cross section. The theoretical stresses in the lower flange tend to be larger than actual. This is believed to arise from the My/I effect resulting from vertical deflection at the pier and is more pronounced in the lower flange because it is farthest from the neutral axis of the section.
6. A comparison of the experimental temperature profiles of the slab directly above the stringer and midway between the stringers indicates that case c is the most realistic of the three theoretical cases, i.e., a) both the slab and the beam in plane stress, b) the slab in plane strain

and the beam in plane stress, and c) the slab in some state between plane stress and plane strain (partially restrained) and the beam in plane stress. The profile midway between stringers is more vertical (less temperature differential) than the profile directly above the stringer. This indicates transverse bending in the slab.

7. All three cases of the theoretical procedure will generally predict upper bound stresses for a composite-girder bridge structure subjected to a steady-state radiant heat flux and having a coefficient of thermal expansion for the concrete lower than that of the steel.

Subject to the limitations of correlation with a single experimental test structure, it is concluded that the theoretical procedure provides a rational method for predicting the thermal behavior of composite-girder bridge structures and can be applied with reasonable confidence when used with realistic temperature profiles, material properties, and substructure stiffness characteristics.

Further substantiation and modification from field testing of prototype structures toward development of rational design criteria for thermal behavior is desirable and feasible.

IX. RECOMMENDATIONS

During the course of any investigation, additional questions arise as an outgrowth of the research. It is customary that most of these questions are beyond the scope of the study and remain unanswered.

From a practical standpoint, the following studies of immediate value for the development of a simplified design procedure to account for the thermal behavior of bridge structures need to be conducted:

1) A study of the thermal behavior of the concrete deck in the transverse and vertical directions.

2) A study of the effect of diaphragms and supports on transverse action.

3) A determination of the effect of noncomposite areas or inadequately spaced shear connectors on deck-stringer interface forces and stress variations.

4) Field studies of temperature distributions to obtain actual temperature profiles and an eventual equivalent profile.

5) A parametric study of the interaction of substructure stiffness, cross-sectional geometric properties, span lengths, material properties, and support deflections to establish the limiting length for composite-girder bridges supported by flexible substructures.

Other studies, which should provide information of value to bridge engineers and those in related fields, were suggested in the prior theoretical study[17, 22]. Some suggestions of interest to this study are:

6) Further information concerning the thermal properties, such as thermal conductivity, specific heat, and thermal diffusivity of concrete, is needed. Although limited data are available in the literature, this study should include the variation of each of these variables with temperature, humidity, proportion of mix, and types of aggregate.

7) The effect of slab reinforcing on the transfer of heat through a concrete bridge deck, i.e., temperature distribution, should be studied.

8) The effect of slab reinforcing and slab cracking when subjected to both environmental exposures and shrinkage stresses needs to be investigated. Some work reported in the literature takes into account the effect of reinforcing; however, this effect on slab bending and biaxial stresses and the resulting distribution of stress in both the concrete deck and the girder have yet to be considered.

9) An improved method, such as a three-dimensional finite element analysis or closed form solutions, to account for slab bending, diaphragm action, and shear connector spacing would provide a tool for more accurately predicting true behavior. This would serve as bounds for development of simple rational design procedures.

10) During this (theoretical) study it was found that the film coefficient greatly affected the distribution of temperature through the cross section but had little effect upon stress magnitudes. However, where turbulent flow exists, the stresses may change. Thus, it is recommended that the effect of the film coefficient be investigated by means of a series of wind tunnel tests.

11) The coefficient of thermal expansion of concrete varies widely with aggregate type, moisture content, and age. It appears that combining concrete with a coefficient of thermal expansion that is lower than that of steel could produce maximum stresses during the winter months, whereas combining concrete with a coefficient higher than that of the steel members would produce higher stresses during the summer months. This should be explored.

12) A study of the probabilistic combinations of loading, including environmental loadings, would be helpful to engineers evaluating the overall effect of this study.

13) A study should be made to evaluate the effect of the assumed initial temperature on temperature distributions obtained by the finite element method.

X. REFERENCES

1. Aleck, B.J., "Thermal Stresses in a Rectangular Plate Clamped Along an Edge," Transactions, American Society of Mechanical Engineers, Vol. 71, 1949.

2. American Society of Heating and Ventilating Engineers, Heating Ventilating Air Conditioning Guide 1950, 28th ed., New York, N.Y., author, 1950.

3. Armaly, B.F., and Leeper, S.P., "Diurnal Stratification of Deep Water Impoundments," paper No. 75-HT-35, presented at the AIChE-ASME Heat Transfer Conference, San Francisco, Calif., Aug. 11-13, 1975, American Society of Mechanical Engineers.

4. Benseman, R.F., "Thermal Properties of Concrete for Roxburgh Dam," Dominion Physical Laboratory, Department of Scientific and Industrial Research, New Zealand, Report No. R. 207, 1953.

5. Berwanger, C., "Thermal Stresses in Composite Bridges," Proceedings, American Society of Civil Engineers, Specialty Conference on Steel Structures, Engineering Extension Series, No. 15, University of Missouri-Columbia, Columbia, Mo., June, 1970.

6. Berwanger, C. and Symko, Y., "Thermal Stresses in Steel-Concrete Composite Bridges," Canadian Journal of Civil Engineering, Vol. 2, No. 1, 1975.

7. Billington, N.S., Thermal Properties of Buildings, Cleaver-Hume Press Ltd., London, England, 1952.

8. Bonnel, D.G.R. and Harper, F.C., "Thermal Expansion of Concrete," Journal of the Institution of Civil Engineers; London, No. 4, Feb., 1950.

9. Brown, R.D., "Properties of Concrete in Reactor Vessels," Conference on Prestressed Pressure Vessels, Proceedings, Institute of Civil Engineers, London, 1968.

10. Campbell-Allen, D., and Thorne, C.F., "The Thermal Conductivity of Concrete," Magazine of Concrete Research, Vol. 15, No. 43, March 1968.

11. Chow, D.Y.F., "Thermal Contraction and Moisture Creep in Concrete," Unpublished Master of Science Thesis, McGill University Library, Montreal, Quebec, 1953.

12. Davis, R.E., "A Summary of the Results of Investigations Having to do with Volumetric Changes in Cements, Mortars and Concretes Produced by Causes Other Than Stress," Proceedings, American Concrete Institute, Vol. 26, 1930.

13. Davisson, M.T., and Salley, J.R., "Model Study of Laterally Loaded Piles," Proceedings, American Society of Civil Engineers, Vol. 96, No. SM5, September, 1970.

14. Dettling, H., "The Thermal Expansion of Hardened Cement Paste, Aggregates, and Concrete (Die Wärmedehnung des Zementsteines, der Gesteine und der Betone)," Bulletin No. 164, Beutscher Ausschuss für Stahlbeton, Berlin, 1964, (Translation No. 458, PCA Technical Information Department, available from SLA Translation Center, John Crerar Library, Chicago).

15. Ekberg, C.E., Jr., and Emanuel, J.H., "Current Design Practice for Bridge Bearings and Expansion Devices," Final Report, Project 547-S, Iowa State University, Engineering Research Institute, 1967.

16. Emanuel, J.H., et al., "An Investigation of Design Criteria for Stresses Induced by Semi-Integral End Bents: Phase I--Feasibility Study," Missouri Cooperative Highway Research Program Final Report 72-9, University of Missouri-Rolla, Rolla, Mo., 1973.

17. Emanuel, J.H., and Hulsey, J.L., "Thermal Stresses and Deformations in Nonprismatic Indeterminate Composite Bridges," paper presented to TRB Committee A2C01--General Structures, Transportation Research Board 55th Annual Meeting, Washington, D.C., January, 1976.

18. Emanuel, J.H., and Hulsey, J.L., "Prediction of the Thermal Coefficient of Expansion of Concrete," Journal of the American Concrete Institute, Vol. 74, No. 4, April, 1977.

19. Emerson, M., "The Calculation of the Distribution of Temperature in Bridges," Transport and Road Research Laboratory Report LR 561, Crowthorne, Berkshire, England, 1973.

20. Hillhouse, J.L., "Dynamic Testing of Anchors Buried in Dry Sand," Unpublished M.S. Thesis, Library, University of Missouri-Rolla, Rolla, Mo., 1975.

21. Homan, J.P., Heat Transfer, McGraw-Hill Book Company, New York, N.Y., 1972.

22. Hulsey, J.L., "Environmental Effects on Composite-Girder Bridge Structures," Unpublished Ph.D. Thesis, Library, University of Missouri-Rolla, Rolla, Mo., 1976.

23. Hulsey, J.L., and Emanuel, J.H., "Finite Element Modelling of Climatically Induced Heat Flow," Paper Presented at International Association for Mathmatics and Computers in Simulation (IMACS) International Symposium on Simulation Software and Numerical Methods for Differential Equations, Virginia Polytechnic Institute and State University, Blacksburg, Va., March, 1977.

24. Hunt, B., and Cooke, N., "Thermal Calculations for Bridge Design," Journal of the Structural Division, American Society of Civil Engineers, Vol. 101, No. ST 9, Proc. paper 11545, Sept., 1975.

25. Idso, S.B., and Jackson, R.D., "Thermal Radiation From the Atmosphere," Journal of Geophysical Research, Vol. 74, 1969, No. 23.

26. Lanigan, A.G., "The Temperature Response of Concrete Box Girder Bridges," Ph.D. Thesis, Report No. 94, School of Engineering, University of Auckland, Auckland, New Zealand, 1973.

27. Lentz, A.E., and Monfore, G.E., "Thermal Conductivities of Portland Cement Paste, Aggregate, and Concrete Down to Very Low Temperatures," Journal of the PCA Research and Development Laboratories, Vol. 8, No. 3, Sept., 1966.

28. McAdams, W.H., Heat Transmission, 3rd ed., McGraw-Hill Book Company, New York, N.Y., 1954.

29. Meyers, S.L., "Thermal Expansion Characteristics of Hardened Cement Paste and of Concrete," Proceedings, Highway Research Board, Vol. 30, 1950.

30. Mitchell, L.J., "Thermal Expansion Tests on Aggregates, Neat Cement, and Concretes," Proceedings, American Society for Testing Materials, Vol. 53, 1953.

31. Newmark, N.M., "Numerical Procedure for Computing Deflections, Moments, and Buckling Loads," Proceedings, American Society of Civil Engineers, Vol. 68, 1942.

32. Priestley, M.J.N., "Linear Heat-Flow Analysis of Concrete Bridge Decks," Research Report 76-3, Department of Civil Engineering, University of Canterbury, Christchurch, New Zealand, Feb., 1976.

33. Reynolds, J.C., and Emanuel, J.H., "Thermal Stresses and Movements in Bridges," Journal of the Structural Division, American Society of Civil Engineers, Vol. 100, No. ST1, Proc. Paper 10275, Jan., 1974.

34. United States Department of the Interior Bureau of Reclamation, "Thermal Properties of Concrete," Boulder Canyon Project Final Reports, Part VII--Cement and Concrete Investigations Bulletin 1, Denver, Colo., 1940.

35. Vesic, A.S., "A Study of Bearing Capacity of Deep Foundations," Final Report, Project B-189, Engineering Experiment Station, Georgia Institute of Technology, 1967.

36. Wilson, E.L., and Nickell, R.E., "Application of the Finite Element Method to Heat Conduction Analysis," Nuclear Engineering and Design, 4, 1966.

37. Zienkiewicz, O.C., and Cheung, Y.K., The Finite Element Method in Structural and Continuum Mechanics, McGraw-Hill Book Co., New York, N.Y., 1967.

38. Zienkiewicz, O.C., and Parekh, C.J., "Transient Field Problems: Two-Dimensional and Three-Dimensional Analysis by Isoparametric Finite Elements," International Journal for Numerical Methods in Engineering, Vol. 2, No. 1, 1970.

39. Zuk, W., "Thermal and Shrinkage Stresses in Composite Beams," Journal of the American Concrete Institute, Vol. 58, No. 3, Sept., 1961.

40. Zuk, W., "Thermal Behavior of Composite Bridges--Insulated and Uninsulated," Highway Research Board No. 76, Highway Research Board, 1965.

VITA

David John Wisch was born in Jefferson City, Missouri, on December 6, 1953. He received his primary and secondary education in Jefferson City, Missouri. In August, 1971, he entered the University of Missouri-Rolla in pursuit of a degree in Civil Engineering which he received in May, 1975.

Since June, 1975, he has been enrolled in the Graduate School of the University of Missouri-Rolla and has held a research assistantship, a graduate teaching assistantship, and a Chancellor's Fellowship.